

Ground State of the Quantum Spin Ice $\text{Yb}_2\text{Ti}_2\text{O}_7$

GROUND STATE OF THE QUANTUM SPIN ICE $\text{YB}_2\text{Ti}_2\text{O}_7$

By
ROBERT MICHAEL D'ORTENZIO, B.Sc. (HONS.)

A Thesis
Submitted to the School of Graduate Studies
in Partial Fulfilment of the Requirements
for the Degree
Master of Science

McMaster University
© Copyright by R.M. D'Ortenzio, June 2013

MASTER OF SCIENCE (2013)
(Department of Physics and Astronomy)

McMaster University
Hamilton, Ontario

TITLE: Ground State of the Quantum Spin Ice $\text{Yb}_2\text{Ti}_2\text{O}_7$

AUTHOR: Robert D'Ortenzio, B.Sc. (Hons.)

SUPERVISOR: Graeme M. Luke

NUMBER OF PAGES: xii, 105

Abstract

The frustrated pyrochlore magnet $\text{Yb}_2\text{Ti}_2\text{O}_7$ provides the exciting possibility of the realization of a "quantum spin ice", where unlike classical counterparts such as $\text{Dy}_2\text{Ti}_2\text{O}_7$ and $\text{Ho}_2\text{Ti}_2\text{O}_7$, magnetic moments do not freeze out at low temperature [Gardner 2004]. A physical example of a quantum spin ice could lead to observation of exotic magnetic phases and fractional quantum excitations.

In this study, we demonstrate through zero field (ZF) and transverse field (TF) μSR measurements in combination with specific heat measurements that the ground state of $\text{Yb}_2\text{Ti}_2\text{O}_7$ contains neither static magnetism nor long range magnetic order. The results presented here have been submitted to Physical Review Letters [R.M. D'Ortenzio 2013]. Our observations are in contrast to the ferromagnetic ground state observed in several neutron scattering experiments [L.-J. Chang 2012, Y. Yasui 2003]. The magnetic Yb^{3+} ions remain in the fast fluctuating dynamic regime down to 16 mK. Our experiments do not observe a first order-like drop in Yb^{3+} fluctuation rate seen by previous μSR and Mössbauer measurements [J.A. Hodges 2002, J.A. Hodges 2004]. Our ZF μSR measurements demonstrate that the magnetic state does not change significantly across the phase transition as viewed in the specific heat for both single and polycrystalline $\text{Yb}_2\text{Ti}_2\text{O}_7$. We propose that this transition is described by some other nonmagnetic order parameter that is unknown, and therefore enters a "hidden order" phase at low temperature.

These experiments were performed on single crystal samples grown via the optical floating zone method. Our single crystal exhibits a broad thermodynamic phase transition or cross over viewed in the specific heat at $T \sim 185$ mK,

and polycrystalline ceramic has a sharp first order like transition peaking at $T \sim 265$ mK. Surprisingly, μ SR results show that the low temperature magnetism is very similar for both of these samples despite the extreme differences in the specific heat. This suggests that sample dependence that effects the thermodynamic transition as viewed in specific heat measurements may not affect the low temperature magnetic state.

Our TF μ SR measurements show that the thermodynamic transition approximately corresponds with a distinct deviation from paramagnetic behavior in the Yb^{3+} spin susceptibility.

Although the microscopic Hamiltonian for $\text{Yb}_2\text{Ti}_2\text{O}_7$ is generally well understood due to a combination of neutron scattering measurements and theoretical work to reproduce thermodynamic properties [Applegate 2012, Hayre 2013, K.A. Ross 2011] our measurements do not support the prediction of ordered magnetism at low temperature. In addition, our specific heat measurements of the Schottky anomaly in an applied magnetic field qualitatively agree with calculations made in [Applegate 2012].

Acknowledgments

"I'm trying to learn something new, trying to surround myself with people that inspire me" - Kendrick Lamar

First and foremost, I would like to thank my supervisor, Graeme Luke. When I began my M. Sc., I quickly realized I had made the correct choice for a supervisor. In addition, the studies presented in this project would have been impossible without the support of the Luke research group, T.J.S. Munsie, T.J. Williams and T. Medino. I would particularly like to thank M.J.P. Gingras, Ray Ng and B.D. Gaulin for theoretical discussions.

Other notable contributions, mainly support for experiments performed in this work by H.A. Dabkowska, A. Dabkowski, K.A. Ross, A. Deschner and C. Marjerrison. In addition, the Uemura group at Columbia University including L. Liu and T. Goko made significant contributions to μ SR measurements. Also, insightful work by S.R. Dunsiger during μ SR measurements proved invaluable.

Also, specific heat measurements by D. Pomaranski and J. Kycia provided an essential component to this work.

Co-authorship

All experiments performed in this study were collaborative efforts.

The single crystals of $\text{Yb}_2\text{Ti}_2\text{O}_7$ were grown with assistance T.J.S Munsie and H.A. Dabkowska at McMaster University. μSR measurements were performed at TRIUMF at the University of British Columbia with the following scientists: T.J. Williams, T.J.S. Munsie, T. Medina and G. Luke from McMaster University, S.R. Dunsiger from Technische Universitat Munchen, T. Goko, L. Liu and Y.J. Uemura from Columbia University. Low temperature specific heat measurements were performed by J.B. Kycia and D. Pomaranski from University of Waterloo. Also, theoretical support was given by B.D. Gaulin from McMaster University, M.J.P. Gingras from University of Waterloo and K.A. Ross who is at Johns Hopkins University.

Finally, the data analysis and the writing contained herein this thesis is a result of my own work, under the supervision of G.M. Luke.

Contents

1	Introduction - Overview of $\text{Yb}_2\text{Ti}_2\text{O}_7$	1
1.1	Magnetic Frustration	2
1.2	Rare Earth Pyrochlores	4
1.3	Ytterbium Titanate - $\text{Yb}_2\text{Ti}_2\text{O}_7$	7
1.4	Previous work on $\text{Yb}_2\text{Ti}_2\text{O}_7$	9
2	Muon Spin Rotation, Resonance and Relaxation (μSR)	19
2.1	Zero Field (ZF) μSR	22
2.2	Transverse Field (TF) μSR	29
2.3	Longitudinal Field (LF) μSR	30
2.4	μSR in Magnetic Systems with Dynamic Fields	32
3	Sample Preparation and Characterization Techniques	35
3.1	Optical Floating Zone Crystal Growth of $\text{Yb}_2\text{Ti}_2\text{O}_7$	35
3.1.1	Polycrystalline Rod Preparation	36
3.1.2	Crystal Growth	38
3.2	Specific Heat Measurements	39
3.2.1	Specific heat above 2 K	41
3.2.2	Specific heat below 2 K	42
3.3	Superconducting Quantum Interference Device (SQUID)	43
3.4	X-Ray Diffraction	47
4	Characterization Results	51
4.1	Verification of Phase through Powder XRD	51
4.2	dc-magnetization Results	53

4.2.1	Determining the Curie-Weiss Temperature	54
4.3	Specific Heat Results	56
4.3.1	Zero Field Specific Heat $30 \text{ mK} < T < 400 \text{ mK}$	57
4.3.2	In Field Specific Heat $2 \text{ K} < T < 20 \text{ K}$	58
5	μSR Results	67
5.1	Zero Field μ SR	68
5.2	Transverse Field μ SR	71
5.3	Comparison to $\text{Tb}_2\text{Sn}_2\text{O}_7$	78
6	Conclusions	81
6.1	Prospective Future Work	85
	Bibliography	87
A	TF relaxation Temperature Dependence and LF measure- ments	97
A.1	TF = 500 G μ SR relaxation	97
A.2	LF μ SR measurements	97
B	"Unconventional Magnetic Ground State in $\text{Yb}_2\text{Ti}_2\text{O}_7$" - Sub- mitted to Physical Review Letters	99

List of Figures

1.1	Three types of crystal lattice that can show geometric magnetic frustration. The triangular lattice (a), the Kagome lattice (b) and the pyrochlore lattice (c) all have triangular geometry [Kittel 2005, Thompson 1999].	3
1.2	Entropy of a classical frustrated spin ice.	6
1.3	The corner sharing tetrahedra of $\text{Yb}_2\text{Ti}_2\text{O}_7$, with the nonmagnetic Ti^{4+} ions removed for clarity. There are two distinct oxygen sites (assuming no symmetry breaking external field is applied), six equivalent O^{2-} (represented in blue) ions surrounding the central Yb^{3+} ion (represented in red), and one in the center of each tetrahedra.	9
1.4	Original specific heat and ac-susceptibility measurements of polycrystalline $\text{Yb}_2\text{Ti}_2\text{O}_7$ by [H.W.J. Blote 1969]. The dash-dotted line in (a) represents a prediction based on entropy $S = R \ln(2)$. The solid line in (b) represents a fit to the inverse magnetic susceptibility above 2 K giving $\Theta_{CW} = 0.4 \pm 0.1$ K.	10
1.5	Left side figure: The first ZF μSR measurements performed on $\text{Yb}_2\text{Ti}_2\text{O}_7$ by Bonville <i>et al.</i> [P. Bonville 2004], showing the muon polarization time spectra. Below the thermodynamic transition at $T \sim 240$ mK, a fast relaxing component develops. The right side figure shows the fluctuation frequency viewed by both Mössbauer and μSR which drops by approximately 4 orders of magnitude at $T \sim 240$ mK.	12
1.6	Magnetic phase diagram of $\text{Yb}_2\text{Ti}_2\text{O}_7$ deduced by Ross <i>et al.</i> [K.A. Ross 2009], showing 2D and 3D magnetic correlations, and the field induced long range magnetic order (LRO) regime.	13
1.7	A single crystal of $\text{Yb}_2\text{Ti}_2\text{O}_7$ we grew in an optical floating zone furnace at McMaster University. This sample was grown in 6 Atm of O_2 . This crystal shows a color gradient possibly indicating O^{2-} defects.	17

-
- 2.1 Left image: Parity violation of weak decay of a surface pion into a muon and a muonic neutrino, illustrating conservation of linear momentum. Right image: positron decay angular direction probability with a given muon polarization at the time of decay. There is a higher probability the positron to have it's momentum vector parallel to the muon' polarization. Taken from [J.E. Sonier 2001]. 22
- 2.2 Schematic for a zero field (ZF) μ SR experiment. A single muon enters the sample area with its polarization antiparallel to the beam direction (or muon momentum vector), and passes through a muon counter that begins a timer. The muon then enters the sample and precesses at a frequency dependent on the local internal field, until it decays into a positron and a neutrino. Due to the weak interaction, the positron's momentum vector has a higher probability to point parallel to the original muon's polarization at the time of decay (Eq. 2.1). The emitted positron is then detected at either the forward (F) or backward (B) position detector. The positron detector turns the timer off, and a time spectra histogram is built for each detector, from which the time dependence of the muon polarization can be extracted. 23
- 2.3 A qualitative representation of the muon's polarization function, investigating a magnetically ordered sample. The solid black line represents the muon's decay $\propto e^{-t/\lambda}$ with lifetime $\lambda \approx 2.197 \mu\text{s}$ [S.L. Lee 1988]. Superimposed on the exponential muon decay are the positron counts for the forward **F** and backward **B** detectors (explained further in Fig. 2.2), giving a sinusoidally oscillating signal which are out of phase by 180° . This oscillating signal can be used to extract information about the properties of the system at the muon's site. To remove the contribution from the exponential muon decay, the asymmetry defined as $(F - B)/(F + B)$ in Eq. 2.4 is plotted in the graph's inset. [S.L. Lee 1988] 24
- 2.4 The left figure shows the muon polarization time evolution for the ferromagnetic material UCoGe below the Curie temperature ($T_{CW} \approx 3$ K). A precession of the muon polarization is observed. The figure on the right shows UCoGe in the paramagnetic regime. There is no net internal magnetic field at the muon's site, therefore no muon precession is observed, just a relaxation of the muon polarization. [A. de Visser 2009] 24

2.5	Schematic showing θ as defined in Eq 2.8 (different than Eq. 2.1), showing the vector relationship of the muon's spin direction, shown to point in the \mathbf{z} direction, and the local magnetic field H_{loc} . [Luke 2013].	25
2.6	Schematic geometry for a transverse field (TF) μ SR experiment. As in other μ SR geometries, a single muon enters the sample area, and an electronic clock is started by its detection. The muon's polarization may be electrostatically tilted perpendicular to its momentum vector, referred to as "spin rotated mode", or may have its polarization antiparallel to its momentum vector, such as shown in this schematic (as in ZF). For both cases, the magnetic field is applied perpendicular to the muon polarization, giving muon precession. The muon hits a positron detector which stops a clock, and a time spectra histogram is built [J.E. Sonier 2001].	31
3.1	Phase diagram of the $\text{Yb}_2\text{O}_3 - \text{TiO}_2$ system. There are two congruently melting phases, $\text{Yb}_2\text{Ti}_2\text{O}_7$ and Yb_2TiO_5 at 2050 °C and 2080 °C, respectively [Queyroux 1965].	37
3.2	(a) shows $\text{Yb}_2\text{Ti}_2\text{O}_7$ in the process of being grown using the optical floating zone furnace at McMaster University. This sample was grown in a 6 Atm O_2 environment, at a rate of ≈ 5 mm/hour. (b) shows a schematic of an optical floating zone furnace. The elliptical mirrors focus light from the halogen bulbs, creating the molten zone. As the polycrystalline feed rod passes through the molten zone, a single crystal is formed.	38
3.3	Visualization of Laue diffraction works using the Ewald Construction. The black points represent the reciprocal lattice in \mathbf{k} space. In figure a) a monochromatic source is used, so $\mathbf{k}_f - \mathbf{k}_i$ is satisfied only if a reciprocal lattice point lies directly on the surface of the gray Ewald sphere. In figure b) the incident wave vector ranges from \mathbf{k}_0 to \mathbf{k}_1 so that all reciprocal lattice points that lie in the volume contained by these two spheres will meet the Bragg condition. These points are represented by all of the points lying within the gray section.	48
4.1	XRD spectra of polycrystalline $\text{Yb}_2\text{Ti}_2\text{O}_7$ (before crystal growth), confirming the phase to be $\text{Yb}_2\text{Ti}_2\text{O}_7$. Rietveld refinement of the data gives a lattice constant of 10.029 ± 0.001 Å.	52

-
- 4.2 Magnetic susceptibility of single crystal $\text{Yb}_2\text{Ti}_2\text{O}_7$ along [100] and [110] directions in applied field up to $H=5$ T. As expected due to the cubic nature of the pyrochlore lattice, there is very small anisotropy between the crystallographic directions, which may be an artifact of the data. Inset: a zoom in of the magnetic susceptibility at $H = 0.2$ T to emphasize the small magnetic anisotropy. 54
- 4.3 Temperature dependence of the inverse magnetic susceptibility of single crystal $\text{Yb}_2\text{Ti}_2\text{O}_7$ aligned such that the applied field $H=500$ G is parallel to a [111] crystallographic direction, as measured in the SQUID at McMaster University. This is the same sample that was used for all μSR experiments. Linear fits are done on different temperature ranges to show that the Curie–Weiss temperature is not constant. The inset displays the magnetic moment temperature dependence. 56
- 4.4 The low temperature specific heat measurements of polycrystalline (red) and single crystal (blue) $\text{Yb}_2\text{Ti}_2\text{O}_7$, performed at the University of Waterloo using a combination of the relaxation method (described above) and the sweep method. For comparison, digitized versions of specific heat results of samples used in studies by Chang *et al.* [L.-J. Chang 2012] (black triangles) and Dalmas de Réotier *et al.* (green diamonds) are included. Taken from [R.M. D’Ortenzio 2013]. 57
- 4.5 (a) shows the specific heat measurements of single crystal $\text{Yb}_2\text{Ti}_2\text{O}_7$ up to $H=9$ T, with the field parallel to a [110] crystallographic direction. (b) shows a comparison of specific heat data taken with the field $H = 9$ T applied parallel to the [110] and [100] directions. 59
- 4.6 Specific heat measurements conducted at least up to 30 K, to give an approximation of where data becomes field independent. 60
- 4.7 A contour plot of specific heat in an applied field. 60
- 4.8 Plots of $C(T)/T$ vs T^2 of single crystal $\text{Yb}_2\text{Ti}_2\text{O}_7$ in a field of $H = 0.5$ T, 1 T, 3 T and 5 T applied parallel to a [110] crystallographic direction. This plot is included to show the linear fit as to subtract the phonon contribution of the specific heat. The extracted parameters γ and β from Eq. 4.2 for each fit are included. Notice for the two images on the right side where $H = 0.5$ T and $H = 3$ T, there is a temperature range where the specific heat dips below the red linear fits. 63

-
- 4.9 Field dependence of parameters β (a) and γ (b) from Eq. 4.2 extracted from specific heat data. The magnetic field is applied along a [110] direction. The $H = 1$ T measurement shows significantly different parameters, as it was fit using a different temperature range. 63
- 4.10 Comparison of theoretical data taken from Applegate *et al.* [Applegate 2012] and experimental data taken at McMaster University, with the T^3 phonon contribution subtracted. 64
- 4.11 Comparison of theoretical data (represented by solid lines) from [Applegate 2012] with our measurements with the $H = 0$ T data numerically subtracted. 65
- 5.1 Left image: the temperature dependence of the relaxation of the muon polarization in ZF. Both polycrystalline and single crystal $\text{Yb}_2\text{Ti}_2\text{O}_7$ show little change. The right images show the asymmetry spectra at 16 mK and 1 K, below and above the magnetic transition at ~ 265 mK for both polycrystalline and single crystal, to emphasize the similarities. Taken from [R.M. D’Ortenzio 2013]. 69
- 5.2 The image on the left: TF=50 mT μ SR measurements of (a) polycrystalline and (b) single crystal $\text{Yb}_2\text{Ti}_2\text{O}_7$. The single crystal is aligned such that a $\langle 111 \rangle$ direction is parallel to the muon momentum (beam direction), but perpendicular to the incident muon’s polarization. The temperature independent signal represented by grey points comes from the Ag sample holder. The black lines added are Curie–Weiss fits with a common $\Theta_{\text{cw}}^\mu = -1.3 \pm 0.5$ K. The inset of both (a) and (b) show the asymmetry time spectra in black, with the fit functions in red. The image on the right: The Fourier transform of the TF asymmetry spectra at $T = 50$ mK for both samples. There are three distinct lines (frequencies) for the polycrystal sample, and four distinct lines for the single crystal sample, justifying the fit presented in Eq. 5.1. Taken from [R.M. D’Ortenzio 2013]. 72
- 5.3 Temperature dependence of the difference between parameterized Curie-Weiss fits on the muon Knight shifts (shown in Fig. 5.2) for both single crystal and polycrystalline $\text{Yb}_2\text{Ti}_2\text{O}_7$ samples. There is a distinct deviation from Curie–Weiss behavior, more pronounced in the polycrystalline sample, at the approximate temperature of the phase transitions that are observed in the specific heat ($T_C \approx 265$ mK for the polycrystal, and $T_C \approx 185$ mK for the single crystal). Error bars are included, but smaller than the data points. Error is on the order of 1%. 77

A.1 The temperature dependence of the Gaussian envelope σ described in Eq. A.1 for single crystal (a) and polycrystalline samples (b).	98
---	----

Introduction - Overview of $\text{Yb}_2\text{Ti}_2\text{O}_7$

Contents

1.1	Magnetic Frustration	2
1.2	Rare Earth Pyrochlores	4
1.3	Ytterbium Titanate - $\text{Yb}_2\text{Ti}_2\text{O}_7$	7
1.4	Previous work on $\text{Yb}_2\text{Ti}_2\text{O}_7$	9

Magnetism plays an essential role in our modern industrialized society, with applications ranging from digital data storage to Magnetic Resonance Imaging. An understanding of magnetic systems can not only impact our society directly through technology, but also better our understanding of the physical laws that govern nature. Possibly the simplest magnetic system to visualize is a ferromagnetic material, where it is energetically preferable for electronic magnetic moments to align parallel to each other, adding up to a net magnetic moment. An active area of research in condensed matter physics is the study of magnetically frustrated systems. In a geometrically frustrated magnetic system, the geometry of the crystal lattice prevents the magnetic interactions between neighboring spins from being satisfied and reaching the

global energy minimum, which can result in a wide range of exotic magnetic phases, such as the "spin ice" phase discussed below.

1.1 Magnetic Frustration

Frustration generally arises in systems with competing interactions that cannot all be simultaneously energetically minimized [Thompson 1999]. Magnetic frustration can arise through at least two scenarios, the first of which occurs when the geometry of a crystal lattice in combination with the nature of the magnetic interactions prevents neighboring spins from reaching their energetically preferable orientations. The second involves competing magnetic interactions, such as multiple orientation-dependent J values results in competition between interactions such that each magnetic moment cannot reach its preferred energy minimum. For example, a two dimensional square lattice with magnetic ions on each corner could have ferromagnetic interactions $J < 0$ along the perimeter for adjacent ions, and antiferromagnet interactions $J > 0$ between diagonal ions. These two exchange parameters, denoted J_1 and J_2 , determine how "frustrated" the interactions are on the $2D$ square lattice. A square lattice with maximum frustration will have $|J_1| = |J_2|$, and has the possibility of remaining disordered down to absolute zero $T = 0$ K [Ross 2012].

A simple example of how geometric frustration can arise with idealized Ising-like antiferromagnet interactions on a two dimensional triangular lattice is illustrated in Fig. 1.1 (a). This simple system can be described by the Hamiltonian in Eq. 1.1, where J is the interaction strength, j, k are the lattice sites in two dimensions ($2D$), and S_j, S_k are the Ising spin orientations, pointing up or down (± 1). Magnetic frustration is more common on lattices

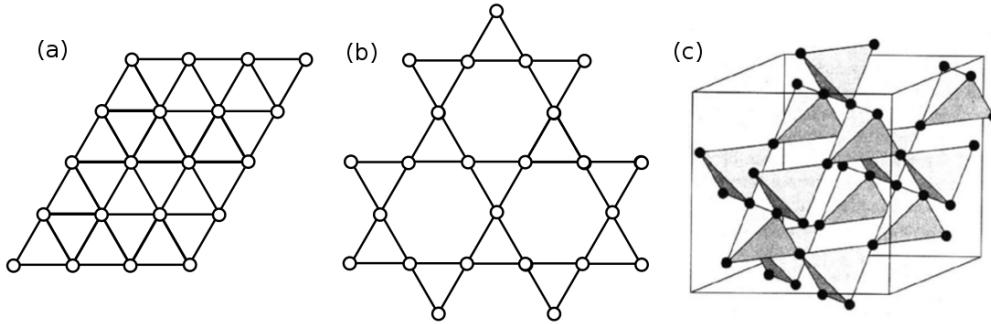


Figure 1.1: Three types of crystal lattice that can show geometric magnetic frustration. The triangular lattice (a), the Kagome lattice (b) and the pyrochlore lattice (c) all have triangular geometry [Kittel 2005, Thompson 1999].

with triangular motifs, such as those illustrated in Fig. 1.1.

$$H = J \sum_{\langle j,k \rangle} S_j \cdot S_k \quad (1.1)$$

Experimentally, an indication of novel magnetic behavior or magnetic frustration is seen as a large Ramirez frustration ratio [C. Lacroix 2011], such that $\Theta_{\text{CW}}/T_C \gg 1$, where Θ_{CW} is the Curie-Weiss temperature extracted from the inverse magnetic susceptibility in the paramagnetic regime, and T_C is a critical temperature of a phase transition, if one exists. For example, the frustrated pyrochlore $\text{Y}_2\text{Mo}_2\text{O}_7$, there is a phase transition at $T_C \approx 22$ K, and a Curie-Weiss temperature of $|\Theta_{\text{CW}}| \approx 200$ K (from dc-magnetization measurements) giving a Ramirez ratio of $\Theta_{\text{CW}}/T_C \approx 9$ [C. Lacroix 2011].

An example of how geometric magnetic frustration can lead to interesting quantum mechanical phenomena is in $\text{ZnCu}_3(\text{OH})_6\text{Cl}_2$, also known as Herbertsmithite. This material possesses a 2D kagome lattice, as shown in Fig. 1.1 (b) made up of magnetic Cu^{2+} ions. A neutron study by Han *et al.* [T-H Han 2012] on single crystals of Herbertsmithite was able to observe

fractional quantum magnetic excitations, which are observed in momentum space as continuous excitations. Classically, spin waves are seen as distinct surfaces in momentum space when viewed by neutron scattering. The authors were able to apply a quantum spin liquid model to accurately reproduce their experimental data. This is just one instance of how magnetic frustration can lead to exotic magnetic phases and excitations.

1.2 Rare Earth Pyrochlores

Rare earth titanates, of the form $R_2Ti_2O_7$, where R is a trivalent magnetic rare earth ion (Ho, Er, Dy, Tb, Yb etc) and the Ti is nonmagnetic, provide an excellent environment in which to study magnetic frustration. In the cubic pyrochlore structure with space group $Fd\bar{3}m$, the magnetic rare earth ions form a corner sharing tetrahedral lattice (Fig. 1.3) leading to frustrated magnetic interactions. The titanates have been a subject of interest of late, as the geometric frustration can lead to a wide range of interesting magnetic phases and phenomenologies [J.S. Gardner 2010].

For example, the rare earth titanate $Ho_2Ti_2O_7$ is well established as a classical "spin ice" material. $Ho_2Ti_2O_7$ has Ising-like magnetic interactions that point towards or away from the corner-sharing tetrahedra center (local [111] direction). This forms a degenerate low temperature ground state, where two spins of each tetrahedra point towards the center, and two away. The magnetic structure of $Ho_2Ti_2O_7$ was measured by first determining the crystal-field parameters of Ho^{3+} using neutron time-of-flight measurements. The splitting of the ground state J multiplet imposes the restriction on the orientation of the Ho^{3+} spins such that it almost an ideal Ising system, separated from the

first excited state with a large energy barrier (20.4 meV) [S. Rosenkranz 2000]. This “two in, two out” ground state is analogous to that formed by hydrogen bonds in the tetrahedral water ice structure, hence the name “spin ice”. This degenerate ground state is experimentally observed through a deviation of the entropy from the expected value of $R \ln(2)$, derived from integrating $C(T)/T$, shown in Fig. 1.2 [A.P. Ramirez 2011]. It has been proposed that $\text{Dy}_2\text{Ti}_2\text{O}_7$ may exhibit magnetic monopole–like quasiparticle excitations, when an energy barrier is overcome to flip one spin of the two in, two out ground state, creating net “monopole charges” in neighboring tetrahedra. These magnetic charges can then travel independently through the lattice at finite energy cost [C. Castelnovo 2008].

More recent careful studies on the specific heat of the spin ice $\text{Dy}_2\text{Ti}_2\text{O}_7$ by Pomaranski *et al.* [D. Pomaranski 2013] ensured their sample was in good thermal equilibrium, and observed an upturn in the specific heat at low temperature. This previously unobserved contribution results in a deviation from the expected value of the missing Pauling entropy $\frac{1}{3}\ln(2)$ [A.P. Ramirez 2011] when $C(T)/T$ is integrated. This measurement has caused doubt that $\text{Dy}_2\text{Ti}_2\text{O}_7$ exemplifies the spin ice model. It is possible that this upturn is a phase transition into an ordered magnetic state, theoretically proposed as the Melko-den Hertog-Gingras (MDG) phase obtained using a loop algorithm [Melko 2001].

The pyrochlore lattice is a non-Bravais lattice, and can be constructed with a face centered cubic (FCC) lattice with a four atom basis, forming the tetrahedra triangular motifs. The pyrochlore lattice \mathbf{R}_i^{P} is the sum of the FCC lattice vectors $\mathbf{R}_i^{\text{fcc}}$ and the four atom basis forming the tetrahedra

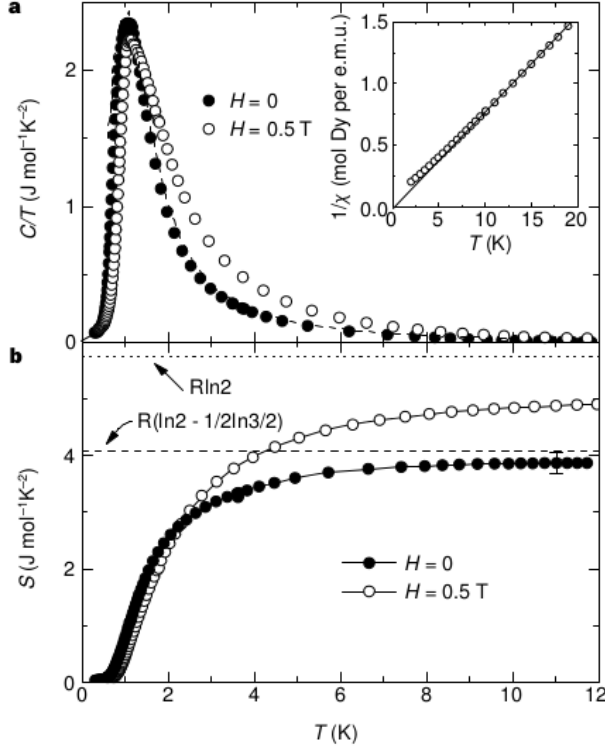


Figure 1.2: (a) is the specific heat ($C(T)$) divided by temperature of the classical spin ice $\text{Dy}_2\text{Ti}_2\text{O}_7$ in $H=0$ T and $H=0.5$ T. The inset of (a) shows inverse magnetic susceptibility to determine the Curie–Weiss temperature (Θ_{CW}). Temperature dependence of the entropy of $\text{Dy}_2\text{Ti}_2\text{O}_7$ found by integrating $C(T)/T$. The missing entropy, approximately $\frac{1}{3}\ln(2)$, comes from the degeneracy of the spin ice ground state [A.P. Ramirez 2011].

structure \mathbf{R}_i^t .

$$\mathbf{R}_i^p = \mathbf{R}_i^{\text{fcc}} + \mathbf{R}_i^t \quad (1.2)$$

The tetrahedra basis vectors \mathbf{R}_i^t are described below [Thompson 1999]. The nearest neighbors are separated by distance $\sqrt{2}r_c/4$ [Gardner 2004] where r_c is the cubic lattice constant, $10.029 \pm 0.1 \text{ \AA}$ for our $\text{Yb}_2\text{Ti}_2\text{O}_7$ samples. This tetrahedra basis has a high propensity towards producing frustrated magnetic systems, depending on the nature of the magnetic interactions.

$$\mathbf{r}_1 = \frac{r_c}{4}(0, 0, 0)$$

$$\mathbf{r}_2 = \frac{r_c}{4}(1, 1, 0)$$

$$\mathbf{r}_3 = \frac{r_c}{4}(1, 0, 1)$$

$$\mathbf{r}_4 = \frac{r_c}{4}(0, 1, 1)$$

$$\mathbf{R}_i^t = a\mathbf{r}_1 + b\mathbf{r}_2 + c\mathbf{r}_3 + d\mathbf{r}_4$$

Where a , b , c and d are real integers.

The atomic positions in the Wyckoff notation for pyrochlores in general are as follows:

Atom	Wyckoff Position	Point Symmetry	Minimal Coordinates
A	16d	$\bar{3}m (D_{3d})$	$\frac{1}{2}, \frac{1}{2}, \frac{1}{2}$
B	16c	$\bar{3}m (D_{3d})$	0, 0, 0
O	48f	mm (C_{2v})	x, $\frac{1}{8}, \frac{1}{8}$
O'	8b	$\bar{4}3m (T_d)$	$\frac{3}{8}, \frac{3}{8}, \frac{3}{8}$

For $\text{Yb}_2\text{Ti}_2\text{O}_7$, $x \approx 0.33$ [J.S. Gardner 2010].

1.3 Ytterbium Titanate - $\text{Yb}_2\text{Ti}_2\text{O}_7$

The rare earth pyrochlore $\text{Yb}_2\text{Ti}_2\text{O}_7$ does not have an Ising-like magnetic anisotropy, such that spins point towards or away from the center of the corner sharing tetrahedra in the pyrochlore structure as in classical "spin ice" frustrated pyrochlores $\text{Ho}_2\text{Ti}_2\text{O}_7$ and $\text{Dy}_2\text{Ti}_2\text{O}_7$ [K.A. Ross 2009, J.S. Gardner 2010]. The magnetic Yb^{3+} ions have an electronic configuration of $4f^{13}$, with a good quantum number of $J = 7/2$ due to a large contribution from orbital angular momentum [Thompson 1999]. The paramagnetic moment is therefore $\mu = g_j \sqrt{J(J+1)} \mu_B \approx 4.54 \mu_B$. This corresponds with experimental measurements of $\mu \approx 4 \mu_B$. It has a Curie–Weiss temperature of $\Theta_{CW} = 0.4 \pm 0.1$ K, indicating weak ferromagnetic interactions (see Chapter. 4).

Studies of the crystal field interactions through neutron time-of-flight scattering show that Yb^{3+} ions have planar XY-like magnetism, suggesting that

the continuous rotational degree of freedom possessed by the spins would prevent magnetic frustration [S. Rosenkranz 2000, Siddharthan 1999]. Because there is an odd number of valence electrons, the Yb^{3+} is a Kramers ion. Therefore, the crystal field must have an even number of levels. The valence shell of an isolated Yb^{3+} ion has a $^2F_{7/2}$ electronic configuration which is split into four Kramers doublets [Thompson 1999]. There is a large energy gap between the lowest excited state and the ground state Kramers doublet of $\sim 650 \pm 40$ K [Cao 2009, Hodges 2001].

Despite continuous rotational degrees of freedom given by the XY-like magnetic interactions, $\text{Yb}_2\text{Ti}_2\text{O}_7$ does not show low temperature freezing out of spins with a degenerate ground state. Instead, previous μSR measurements (Muon Spin Rotation/Relaxation/Resonance – see Chapter 5 for an introduction to μSR) only give evidence of a dynamic ground state with a non-zero spin fluctuation rate down to 30 mK, and no magnetic ordered ground state [J.A. Hodges 2002, J.A. Hodges 2004].

$\text{Yb}_2\text{Ti}_2\text{O}_7$ has a thermodynamic transition at approximately 265 mK (for stoichiometric polycrystalline samples), first viewed in Ref. [H.W.J. Blote 1969] via the temperature dependence of the specific heat. Surprisingly, there is controversy if this phase transition gives way to a long range magnetic ordered state at low temperature. There is evidence for both an ordered ferromagnetic ground state, and a dynamic ground state where spins are fluctuating quickly with only short range magnetic correlations (see Section 1.4 for further discussion). The phase transition corresponds approximately to the temperature of the drop in the Yb^{3+} fluctuation rate as measured by previous μSR and Mössbauer absorption spectra [J.A. Hodges 2002, J.A. Hodges 2004], which decreases by 4 orders

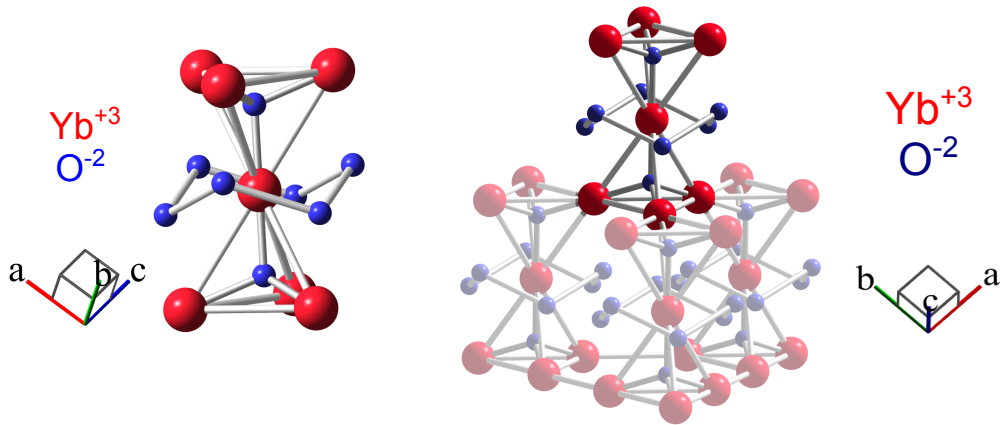


Figure 1.3: The corner sharing tetrahedra of $\text{Yb}_2\text{Ti}_2\text{O}_7$, with the nonmagnetic Ti^{4+} ions removed for clarity. There are two distinct oxygen sites (assuming no symmetry breaking external field is applied), six equivalent O^{2-} (represented in blue) ions surrounding the central Yb^{3+} ion (represented in red), and one in the center of each tetrahedra.

of magnitude in a first order manner, with the spins remaining dynamic. It has been suggested [Maestro 2004] that at low temperatures quantum fluctuations that cause the ground state of $\text{Yb}_2\text{Ti}_2\text{O}_7$ to remain dynamic. In combination with geometric magnetic frustration, the possibility of the realization of an exotic magnetic quantum spin liquid state makes $\text{Yb}_2\text{Ti}_2\text{O}_7$ an important system to study.

1.4 Previous work on $\text{Yb}_2\text{Ti}_2\text{O}_7$

$\text{Yb}_2\text{Ti}_2\text{O}_7$ and other frustrated pyrochlores have received much attention recently, so this overview will focus only on studies relevant to results presented in subsequent chapters. The first reported measurement of $\text{Yb}_2\text{Ti}_2\text{O}_7$ were of the magnetic susceptibility between $T=2$ and 1400 K, performed by Townsend *et al.* in 1968 [Townsend 1968]. Polycrystalline $\text{Yb}_2\text{Ti}_2\text{O}_7$ was then charac-

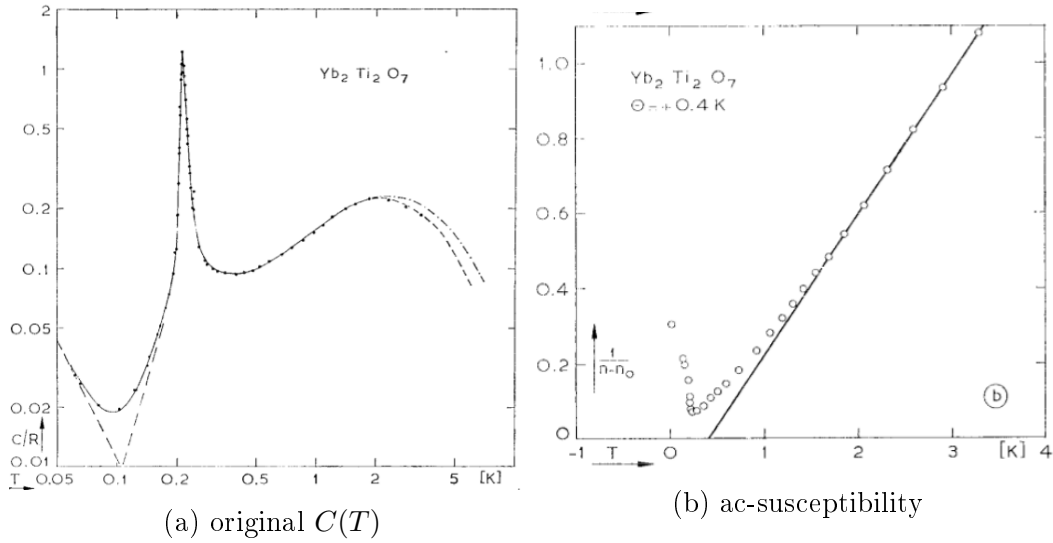


Figure 1.4: Original specific heat and ac-susceptibility measurements of polycrystalline $\text{Yb}_2\text{Ti}_2\text{O}_7$ by [H.W.J. Blote 1969]. The dash-dotted line in (a) represents a prediction based on entropy $S = R\ln(2)$. The solid line in (b) represents a fit to the inverse magnetic susceptibility above 2 K giving $\Theta_{CW} = 0.4 \pm 0.1$ K.

terized by Blote *et al.* [H.W.J. Blote 1969] shown in Fig. 1.4, using low temperature specific heat and ac-magnetic susceptibility measurements. Blote *et al.* measured a Curie-Weiss temperature of $\Theta_{CW} \approx 0.4$ K, suggesting weak ferromagnetic interactions. This value is consistent with those obtained for our samples, shown in Chapter. 4. Specific heat measurements revealed a sharp peak at ~ 200 mK, indicating a first order phase transition. In addition, a broad Schottky anomaly was observed between approximately 1 and 5 K. Blote *et al.* integrated the specific heat divided by the temperature $C(T)/T$ and note the result is less than the expected $R\ln(2)$, which was later recognized as a sign of magnetic frustration [A.P. Ramirez 2011].

Years later in 2004, low temperature Mössbauer and μSR measurements were conducted by Bonville *et al.* [P. Bonville 2004], confirming a first order like transition at ~ 240 mK. The Mössbauer measurements show a five line

magnetic hyperfine field up to ~ 220 mK, before the hyperfine field is suddenly washed out by a single broad line. The narrow range of temperatures across which this distinct change occurs is characteristic of a first order transition. However, the Mössbauer experiments could not reveal the nature of the magnetic ground state nor if long range magnetic order exists. Their ZF μ SR asymmetry spectra show the development of a fast relaxing component below the transition temperature. Above the transition temperature, the asymmetry spectra decay with a single weakly temperature dependent exponential timescale. Above the transition in the paramagnetic phase, Bonville *et al* assume that the Yb^{3+} ions are in the fast fluctuating "extreme-narrowing" limit and thus can extract the Yb^{3+} ion fluctuation rate from the decay timescale λ such that $\lambda = 2\Delta_p^2/\nu$ where ν is the Yb^{3+} ion fluctuation rate and Δ_p is the root mean square of the deviation of the distribution of dipolar couplings at the muon's stopping site inside the $\text{Yb}_2\text{Ti}_2\text{O}_7$. Below the transition, the authors extract the fluctuation frequency from the muon depolarization spectra by applying a Kubo-Toyabe decay function (see Chapter 5 for Kubo-Toyabe theory). From this, the authors report a drop in the spin fluctuation rate of approximately 4 orders of magnitude at the transition temperature, shown on the right side of Fig.1.5. Despite this drop, spins remain dynamic down to ~ 30 mK, with no evidence of long range magnetic order or static magnetic fields.

Neutron scattering experiments have introduced controversy over the nature of the magnetic ground state of $\text{Yb}_2\text{Ti}_2\text{O}_7$. Initial neutron studies by Yasui *et al.* [Y. Yasui 2003] observed a magnetic component develop on several different nuclear Bragg peaks below the transition temperature $T \sim 210$ mK, showing evidence of collinear ferromagnetic order. They also note the

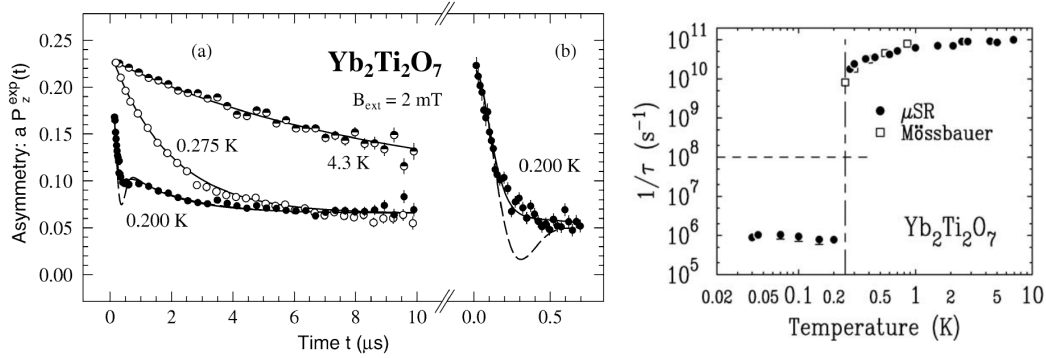


Figure 1.5: Left side figure: The first ZF μSR measurements performed on $\text{Yb}_2\text{Ti}_2\text{O}_7$ by Bonville *et al.* [P. Bonville 2004], showing the muon polarization time spectra. Below the thermodynamic transition at $T \sim 240 \text{ mK}$, a fast relaxing component develops. The right side figure shows the fluctuation frequency viewed by both Mössbauer and μSR which drops by approximately 4 orders of magnitude at $T \sim 240 \text{ mK}$.

long timescale (approximately 2 hours at low temperatures) for $\text{Yb}_2\text{Ti}_2\text{O}_7$ to reach thermal equilibrium. However, Gardner *et al.* [J.S. Gardner 2004] using polarized neutrons and neutron spin echo techniques confirmed that ferromagnetic interactions dominate, but observed no frozen ordered magnetic phase below the phase transition at approximately 240 mK. Instead, they observed a dynamic ground state where Yb^{3+} spins continue to fluctuate. Bonville *et al.* [P. Bonville 2004] were the first to view rods of scattering along the $[111]$ directions in momentum space below $T = 4 \text{ K}$, interpreted as short range $2D$ magnetic correlations.

Chang *et al.* [L.-J. Chang 2012] provide evidence of a first order transition to a ferromagnetic ground state. Chang *et al.*'s polarized neutron study shows the diffuse rods of scattering along the $[111]$ directions in momentum space form magnetic Bragg peaks below $T \sim 210 \text{ mK}$. In addition, temperature hysteresis of the amplitude of a $[111]$ magnetic Bragg peak was observed below the transition, an indication of a ferromagnetic state or a first order

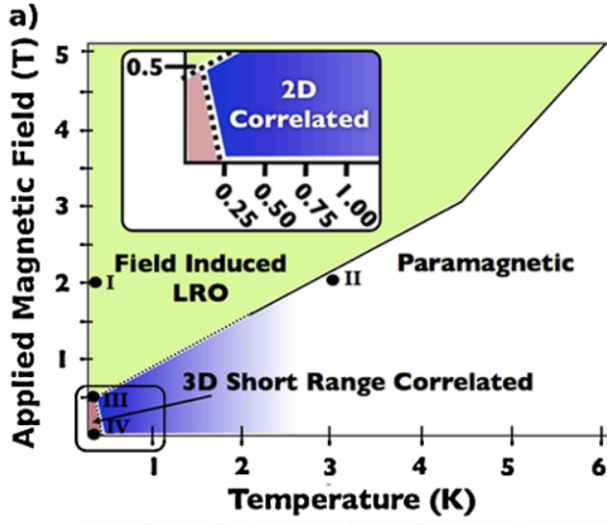


Figure 1.6: Magnetic phase diagram of $\text{Yb}_2\text{Ti}_2\text{O}_7$ deduced by Ross *et al.* [K.A. Ross 2009], showing 2D and 3D magnetic correlations, and the field induced long range magnetic order (LRO) regime.

transition. The authors observe pinch-point features in the magnetic scattering in momentum space, indicative of a large magnetic correlation length (in real space). However, Chang *et al.* [L.-J. Chang 2012] do not report observation of magnetic spin waves, which would give more conclusive evidence of ferromagnetic order.

Ross *et al.* [K.A. Ross 2009] deduced the phase diagram shown in Fig. 1.6 for $\text{Yb}_2\text{Ti}_2\text{O}_7$ using neutron scattering and dc-susceptibility measurements. The study observed a field induced ferromagnetic ordered state through spin waves for applied field $H > 0.5 \text{ T}$ parallel to the $[1\bar{1}0]$ crystallographic direction at low temperature. Cooling down past the transition temperature ($T \sim 240 \text{ mK}$ for Ross *et al.*'s sample), the rods of scattering along $[111]$ directions build up intensity at the nuclear Bragg peaks, interpreted as a crossover from 2D to 3D magnetic correlations. These correlations remain short range, and the low temperature magnetic state remains dynamic down to $\sim 30 \text{ mK}$.

A further study by Ross *et al.* [K.A. Ross 2011] impressively extract a full set of Hamiltonian parameters from the neutron data in the field induced long range ordered state data from [K.A. Ross 2009]. The theoretical Hamiltonian

assumes nearest neighbor exchange coupling, justified by the highly localized f -electrons of the Yb^{3+} ions. Exchange interactions result from the overlap of quantum mechanical electron wave functions, rather than the interaction of magnetic fields created by electronic dipole moments. The exchange interaction may be direct, or via "super-exchange" mediated by some intermediate ion, such as an O^{2-} ion.

The resulting components of the exchange interaction tensor demonstrates that $\text{Yb}_2\text{Ti}_2\text{O}_7$ does not have classical spin ice-like magnetism (as in $\text{Ho}_2\text{Ti}_2\text{O}_7$ or $\text{Dy}_2\text{Ti}_2\text{O}_7$) with large anisotropy only along the local $[111]$ directions, rather significant components of the exchange interactions are in the local XY plane. Although the magnetism is not completely XY-like as previously reported, [Siddharthan 1999] because the largest component of the exchange matrix is along the local $[111]$ direction. Ross *et al.* suggest that due to strong fluctuations, $\text{Yb}_2\text{Ti}_2\text{O}_7$ may be a "quantum spin liquid" such that quantum mechanical fluctuations dominate and prevent magnetic ordering down to absolute zero temperature. A quantum spin liquid could exhibit fractional $S = 1/2$ magnetic quantum excitations, distinct from classical spin waves.

Applegate *et al.* [Applegate 2012] and Hayre *et al.* [Hayre 2013] were able to use the exchange parameters determined in [K.A. Ross 2011] to compute thermodynamic properties: entropy $S(T)$, specific heat $C(T)$ and magnetization $M(T, H)$. The experimental magnetization data $M(T, H)$ presented in [Hayre 2013] was taken from the same $\text{Yb}_2\text{Ti}_2\text{O}_7$ crystal that dc-magnetization, specific heat and μSR measurements were performed on in this study. Applicable to the in-field specific heat measurements presented in Chapter 3, Applegate *et al.* focus on the Schottky anomaly that occurs

$1\text{ K} \leq T \leq 10\text{ K}$. They attribute the sharp peak viewed in the specific heat to a first order transition to an ordered ferrimagnetic ground state, and the Schottky anomaly as a crossover from the paramagnetic regime to a quantum spin ice phase as temperature is decreased. Thus, the authors propose a unique combination of quantum dynamics and an ordered magnetic ground state are represented as the two features in the low temperature specific heat. In this study, we will compare the theoretical data presented in [Applegate 2012] to specific heat measurements taken of single crystal $\text{Yb}_2\text{Ti}_2\text{O}_7$ above 2 K in an applied field up to $H = 9\text{ T}$. Moreover, we will address their claim of a ferrimagnetic ground state through ZF μSR measurements. It is important to note that this exchange Hamiltonian model uses the J parameters extracted from neutron studies [K.A. Ross 2011] in the induced order regime (as shown in Fig 1.6). Therefore, the authors note this model fails and does not reproduce neutron data at low applied fields, for $H < 0.5\text{ T}$, below the long range order regime. However, it qualitatively reproduces thermodynamic quantities $S(T)$ and $C(T)$ in zero applied field above $T = 1\text{ K}$.

The reader may notice the range of temperatures reported on the thermodynamic phase transition as viewed in the specific heat, from $T \sim 200\text{ mK}$ [H.W.J. Blote 1969] to $T \sim 265\text{ mK}$ for samples used in this study and by Ross *et al.* [K.A. Ross 2012]. The sharpness and temperature of this transition varies significantly between studies, and it has been proposed by Ross *et al.* [K.A. Ross 2012] that the low temperature magnetic state is sensitive to sample preparation conditions. The authors propose a "stuffed pyrochlore" model, where magnetic Yb^{3+} ions substitute on the nonmagnetic Ti^{4+} sublattice, affecting the low temperature magnetism through local lattice deformations and random exchange bonds. The stoichiometry of this stuffed

compound is described by Eq. 1.3 below.



In the above equation, x is the degree of stuffing. In Ross *et al.*'s sample, $x=0.046(4)$. This off-stoichiometry leads to variation in the cubic unit cell length a , which Ross *et al.* measured using Rietveld powder neutron diffraction measurements, comparing polycrystalline rods that are theoretically stoichiometric ($x=0$), and crushed up single crystal after growth using the optical floating zone method. Measuring the lattice constant a could give a measure of the level of stuffing in a specific sample. The authors suggest this off-stoichiometry could explain the range of reports on the low temperature magnetic state of $\text{Yb}_2\text{Ti}_2\text{O}_7$.

In some prepared single crystals grown in an optical floating zone furnace, there is a color gradient along the length of the crystal. There may be oxygen defects beyond those described by the stuffed model [K.A. Ross 2012] that change some oxidation states (possibly the d orbitals of the Ti ions) that result in a color change. An example of a single crystal of $\text{Yb}_2\text{Ti}_2\text{O}_7$ that shows a darkening along its length is shown in Fig. 1.7. Crystal growth is discussed in Chapter 3.



Figure 1.7: A single crystal of $\text{Yb}_2\text{Ti}_2\text{O}_7$ we grew in an optical floating zone furnace at McMaster University. This sample was grown in 6 Atm of O_2 . This crystal shows a color gradient possibly indicating O^{2-} defects.

Muon Spin Rotation, Resonance and Relaxation (μ SR)

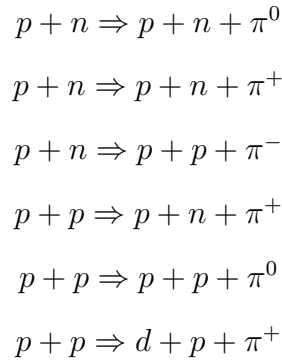
Contents

2.1	Zero Field (ZF) μSR	22
2.2	Transverse Field (TF) μSR	29
2.3	Longitudinal Field (LF) μSR	30
2.4	μSR in Magnetic Systems with Dynamic Fields . . .	32

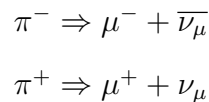
Muon Spin Rotation/Relaxation/Resonance (μ SR) is an extremely sensitive (~ 0.1 G) local probe of magnetic fields. μ SR is a tool used to probe the local magnetic environment surrounding the implanted muon. Fundamentally, the underlying principle of μ SR is to measure the time evolution of a muon's spin polarization inside of a material. From this polarization function, information about the magnetic, electronic and chemical properties of the material can be extracted. For example, information about the superconducting penetration depth, superconducting vortex lattice, magnetic ordering and local spin susceptibility are just a few of the many applications of μ SR in condensed matter physics [J.E. Sonier 2001].

Muons can be produced by colliding protons (approximately 500 MeV at TRI-

UMF) into a target usually made of a material with a low atomic Z number, such as carbon or beryllium. At TRIUMF, H^- ions are accelerated in a cyclotron, then stripped of electrons which extracts them producing a proton beamline. Upon leaving the cyclotron accelerator, protons then collide with a neutron or proton in the target and produce pions (π^+ , π^0 or π^-) which weak decay with lifetime $\tau \approx 26$ ns to muons. The possible pion production reactions are shown in below.

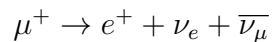


For most μ SR experiments, such as those we have performed at TRIUMF, only positive muons are used, as negative muons risk being captured by a positively charged nucleus due to the electrostatic attraction [S.L. Lee 1988]. Usually, only muons that are produced from pions near the surface of the proton target are used for most μ SR measurements. These pions are assumed to be effectively at rest. When they decay producing a positive muon and a neutrino ($\bar{\nu}_\mu$) as shown below, the muon is 100% spin polarized because of conservation of angular momentum.



This is a consequence of the pion having spin 0, and neutrinos only being left handed. The generated muon then has a momentum of 29.79 MeV/c

and an energy of 4.119 MeV. An illustration of this process is shown below in Fig. 2.1 [Rovers 2001, J.E. Sonier 2001]. Positive muons (μ^+) decay into positrons (e^+) and neutrinos, with a lifetime of $\tau_\mu = 2.19724(7)$ μs [S.L. Lee 1988].



Emitted positrons from the decay of positive muons have an angular probability distribution described by Eq. 2.1, where θ describes the angle between the muon’s polarization direction at the time of decay, and the emitted positron’s momentum vector. This parity violation is a consequence of there only being left handed neutrinos. The constant a depends on the emitted positron energy, and increases monotonically to a maximum value of $a = 1$ at an energy of 52.83 MeV [S.L. Lee 1988]. Notice that the probability $W(\theta)$ is at a maximum when $\theta = 0$.

$$W(\theta) = 1 + a \cos(\theta) \tag{2.1}$$

When the muon is implanted into an environment that has a static local magnetic field, the muon’s spin will precess at a frequency $\omega_\mu = \gamma_\mu |\mathbf{B}|$ where \mathbf{B} is the internal local magnetic field of the sample and $\gamma_\mu = 135.538817(12)$ Hz/T is the muon gyromagnetic ratio. An important key that makes μSR a powerful probe of magnetic environments is the precession frequency is independent of the angle between the magnetic field vector and the muon’s spin [S.L. Lee 1988]. Therefore, the magnitude of the local magnetic field is reflected by the precession frequency of the muon.

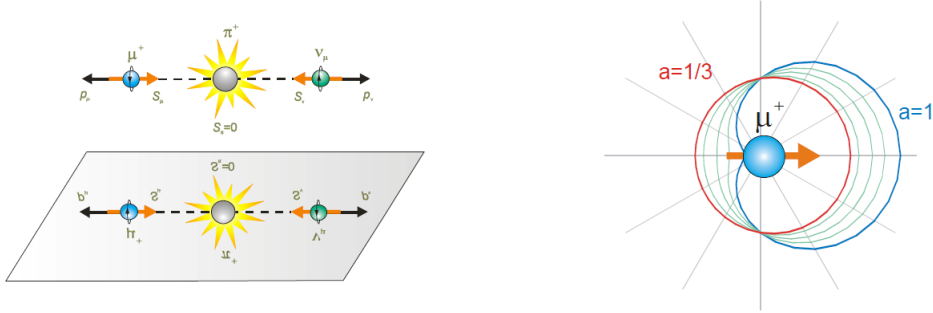


Figure 2.1: Left image: Parity violation of weak decay of a surface pion into a muon and a muonic neutrino, illustrating conservation of linear momentum. Right image: positron decay angular direction probability with a given muon polarization at the time of decay. There is a higher probability the positron to have it's momentum vector parallel to the muon' polarization. Taken from [J.E. Sonier 2001].

2.1 Zero Field (ZF) μ SR

There are several different experimental geometries in which μ SR measurements can be performed, each giving unique information about the internal magnetic environment of a sample in question. Possibly the simplest example, Zero Field (ZF) μ SR implants 100% spin polarized muons into the sample with no externally applied field. A diagram of the setup for a basic ZF μ SR experiment is shown in Fig. 2.2.

With no external applied magnetic field, muons implanted into the sample will only precess if they sit in an environment with a nonzero net magnetic field. For example, a ferromagnetic material below the Curie temperature, could have a net internal magnetic field at the muon implantation site, resulting in precession (Fig. A.1a). If this sample is then warmed up into the paramagnetic regime, the ferromagnetic order will be destroyed by thermal fluctuations (Fig. A.1b). At the location of muon implantation, the magnetic field will average to zero, and the muon will not precess.

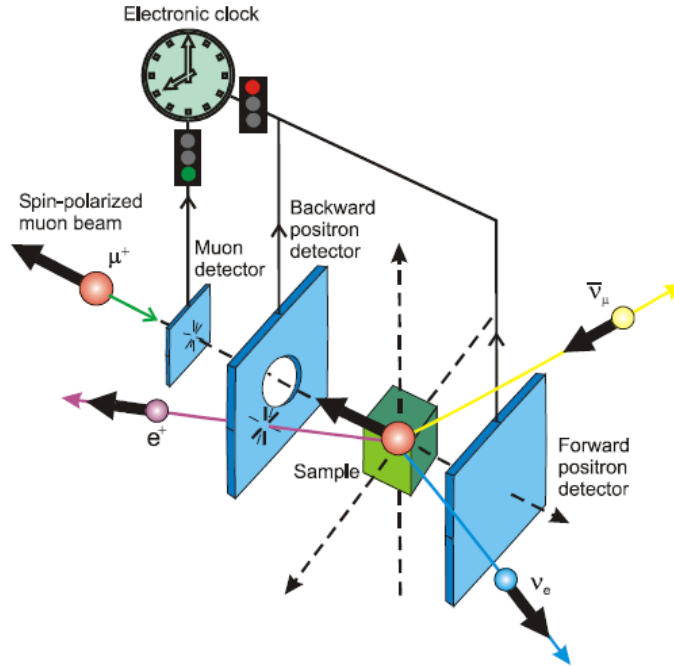


Figure 2.2: Schematic for a zero field (ZF) μ SR experiment. A single muon enters the sample area with its polarization antiparallel to the beam direction (or muon momentum vector), and passes through a muon counter that begins a timer. The muon then enters the sample and precesses at a frequency dependent on the local internal field, until it decays into a positron and a neutrino. Due to the weak interaction, the positron’s momentum vector has a higher probability to point parallel to the original muon’s polarization at the time of decay (Eq. 2.1). The emitted positron is then detected at either the forward (F) or backward (B) position detector. The positron detector turns the timer off, and a time spectra histogram is built for each detector, from which the time dependence of the muon polarization can be extracted.

ZF μ SR is a very sensitive probe of static magnetic fields. An advantage of μ SR over complementary techniques such as polarized neutron scattering measurements is that the sample does not need to be a single crystal to determine the magnetic state, as μ SR is not a momentum resolved technique. Often, when a new sample is produced, one of the first experiments employed to investigate its magnetism is μ SR, before techniques are developed to grow large single crystals for other experiments.

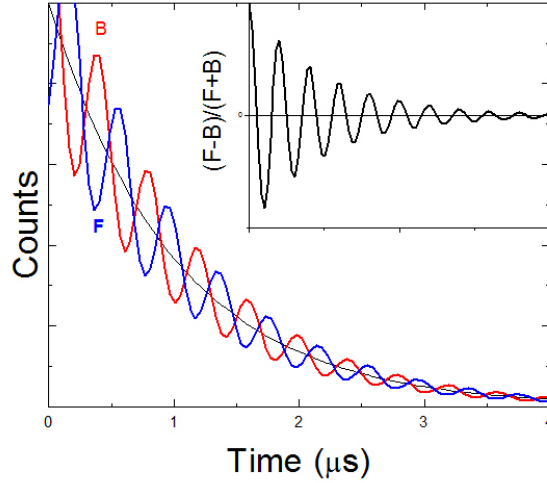


Figure 2.3: A qualitative representation of the muon’s polarization function, investigating a magnetically ordered sample. The solid black line represents the muon’s decay $\propto e^{-t/\lambda}$ with lifetime $\lambda \approx 2.197 \mu\text{s}$ [S.L. Lee 1988]. Superimposed on the exponential muon decay are the positron counts for the forward **F** and backward **B** detectors (explained further in Fig. 2.2), giving a sinusoidally oscillating signal which are out of phase by 180° . This oscillating signal can be used to extract information about the properties of the system at the muon’s site. To remove the contribution from the exponential muon decay, the asymmetry defined as $(F - B)/(F + B)$ in Eq. 2.4 is plotted in the graph’s inset. [S.L. Lee 1988]

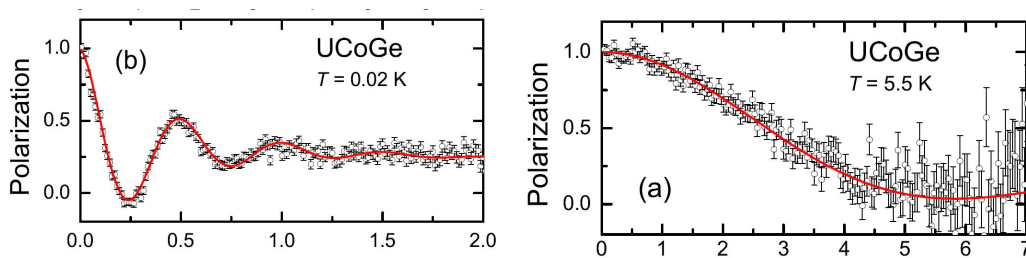


Figure 2.4: The left figure shows the muon polarization time evolution for the ferromagnetic material UCoGe below the Curie temperature ($T_{CW} \approx 3 \text{ K}$). A precession of the muon polarization is observed. The figure on the right shows UCoGe in the paramagnetic regime. There is no net internal magnetic field at the muon’s site, therefore no muon precession is observed, just a relaxation of the muon polarization. [A. de Visser 2009]

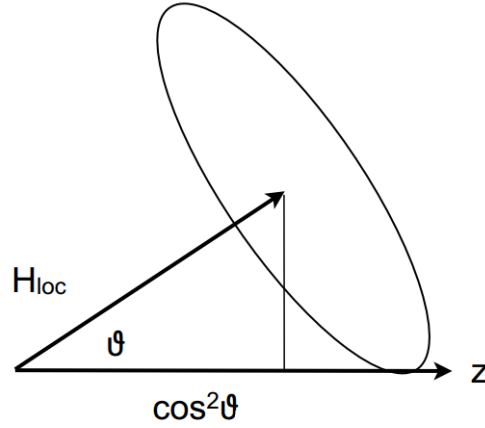


Figure 2.5: Schematic showing θ as defined in Eq 2.8 (different than Eq. 2.1), showing the vector relationship of the muon’s spin direction, shown to point in the \mathbf{z} direction, and the local magnetic field H_{loc} . [Luke 2013].

The time evolution of the total positron counts at the forward $F(t)$ and backward counter $B(t)$ can be described by Eq. 2.2 and 2.3 respectively.

$$F(t) = N_F e^{\frac{-t}{\tau_\mu}} (1 + A_F G_z(t)) + b_F \quad (2.2)$$

$$B(t) = N_B e^{\frac{-t}{\tau_\mu}} (1 - A_B G_z(t)) + b_B \quad (2.3)$$

Where in the equation above, the exponential factor $e^{\frac{-t}{\tau_\mu}}$ is the decay of the muon via the weak interaction, A is the intrinsic maximum asymmetry of the counter which is dependent on the properties of the detector, b_F and b_B are the time independent backgrounds that are subtracted by measuring counts before any muons arrive (before the clock starts in Fig. 2.3), and $G_z(t)$ is the muon polarization function which is defined in Eq. 2.9, containing all of the physical information we wish to extract.

To isolate the average muon polarization function $G_z(t)$ we can define the

asymmetry $A(t)$ as:

$$A(t) \equiv \frac{F(t) - B(t)}{F(t) + B(t)} = \frac{(1 - \alpha) + (1 + \alpha\beta)A_B G_z(t)}{(1 + \alpha) + (1 - \alpha\beta)A_B G_z(t)} \quad (2.4)$$

Where:

$$\alpha \equiv \frac{N_F}{N_B} \quad (2.5)$$

$$\beta \equiv \frac{A_F}{A_B} \quad (2.6)$$

If the detectors have identical geometries, then $N_F = N_B$ and $A_F = A_B$ and $\alpha = \beta = 1$, and Eq. 2.4 becomes Eq. 2.7, and we can extract the muon polarization function. In practice, $A_F \neq A_B$ and $N_F \neq N_B$. This small difference in positron detector properties can be corrected for during data analysis which includes α , β defined in Eq. 2.5 2.6, which take this difference into account. The correction factor α is dependent on experimental conditions such as applied magnetic field, and therefore must be included as a parameter when asymmetry spectra are fit. β is less sensitive to changes and can be approximated as $\beta = 1$ for many experiments [Luke 1988]. For all experiments that we conducted in this study, we assume $\beta = 1$. A representation of an ideal asymmetry spectra is shown in Fig. 2.3.

$$A(t) \equiv \frac{F(t) - B(t)}{F(t) + B(t)} \propto G_z(t) \quad (2.7)$$

The spin polarization $\sigma_z(B, t)$ of a muon with its initial polarization vector along the z direction, with a time independent magnetic field \mathbf{B} tilted by angle θ is given by Eq. 2.8, and shown schematically in Fig. 2.5.

$$\sigma_z(B, t) = \cos^2(\theta) + \sin^2(\theta) \cos(\gamma_\mu |B|t) = \frac{|B_z|^2}{|B|^2} + \frac{|B_x|^2 + |B_y|^2}{B^2} \cos(\gamma_\mu |B|t) \quad (2.8)$$

When a muon is implanted in a sample, it may experience a spatially dependent field distribution. This field distribution is described by the magnetic field density $P(\mathbf{B}(x, y, z))$. Taking this into account, we arrive at Eq. 2.9, where $G_z(t)$ is the average spin polarization such that $G_z(t) = \langle \sigma_z \rangle$ projected along one direction:

$$G_z(t) = \int P(\mathbf{B}(x, y, z)) \sigma_z d\mathbf{B}(x, y, z) \quad (2.9)$$

In calculating the polarization function, the assumption $P(\mathbf{B}) = P(\mathbf{B}_x)P(\mathbf{B}_y)P(\mathbf{B}_z)$ may be made, so that Eq. 2.9 becomes Eq. 2.10:

$$G_z(t) = \int \int \int P(B_x)P(B_y)P(B_z) \sigma_z dB_x dB_y dB_z \quad (2.10)$$

For a polycrystalline sample with a static internal magnetic field, it can be assumed that $\langle B_x \rangle = \langle B_y \rangle = \langle B_z \rangle$, and therefore $P(\mathbf{B})$ becomes scalar $P(B)$, and Eq. 2.9 can be integrated over spherical coordinates to become Eq. 2.11:

$$G_z(t) = \frac{1}{3} + \frac{2}{3} \int P(B) \cos(\gamma_\mu |B|t) dB \quad (2.11)$$

The time independent component, $\frac{1}{3}$ for an isotropic field distribution, is a good indication that static fields exist in a sample. The time dependent component with the $\frac{2}{3}$ prefactor will depend on the nature of the internal isotropic field distribution $P(B)$ and $|B|$. If static fields exist in a sample that has some non-isotropic field distribution, for example a frozen (static

moments) ferromagnet, the time independent prefactor in Eq. 2.11 will vary from 0 to 1 depending on the the internal field's orientation with respect to the initial muon polarization. If the muon's polarization happens to be parallel to the magnetic moment in a frozen ferromagnet, then there may be no time dependence of $G_z(t)$

If a system has randomly oriented local fields, such as in a frozen spin glass system with dense moments, or randomly oriented nuclear dipole fields [S.L. Lee 1988] the field distribution at the muon's location is often well described by the Gaussian function in Eq. 2.12 [S.L. Lee 1988]:

$$P(H_i) = \frac{\gamma_\mu}{2\pi\Delta} e^{-\frac{\gamma_\mu^2 H_i^2}{2\Delta^2}}, i = x, y, z \quad (2.12)$$

Where Δ is described by Eq. 2.13:

$$\Delta = \gamma_\mu^2 \langle H_i^2 \rangle, i = x, y, z \quad (2.13)$$

Substituting Eq. 2.12 into Eq. 2.9 and integrating, we arrive at the famous Kubo–Toyabe polarization function, first derived in 1966 [Kubo 1967]:

$$G_z(t) = \frac{1}{3} + \frac{2}{3}(1 - \Delta^2 t^2) e^{-\frac{\Delta^2 t^2}{2}} \quad (2.14)$$

A further example is a system with a sinusoidal field distribution, incommensurate with the crystal lattice such that the spacial field distribution is defined by $B(\vec{R}) = B_{max} \sin(\vec{k} \cdot \vec{R})$ where \vec{k} is a reciprocal lattice vector. The probability distribution as a function of field is then given by:

$$P(|B|) \propto \frac{B_{max}}{\sqrt{B_{max}^2 - |B|^2}} \quad (2.15)$$

Combining this with Eq. 2.10, we get the muon polarization function in zero external applied field:

$$G_z(t) = \frac{1}{3} + \frac{2}{3}J_o(\gamma_\mu B_{max}t) \quad (2.16)$$

Where J_o is the zero order Bessel function. If the field distribution is not sharply defined, (for example due to a contribution from nuclear dipole fields), the amplitude $G_z(t)$ will be further dampened [S.L. Lee 1988]. Working backwards from the experimentally observed muon polarization $G_z(t)$ the internal field distribution or magnetic phase can be determined.

2.2 Transverse Field (TF) μ SR

When a field is applied perpendicular to the initial muon’s polarization (transverse field), the muon will precess even if the local field in the sample is zero. The total local field experienced by the muon \mathbf{B}_{tot} is the vector sum of the internal field due to the sample’s magnetism \mathbf{B}_{loc} and the external applied field \mathbf{B}_{ext} such that $\mathbf{B}_{tot} = \mathbf{B}_{loc} + \mathbf{B}_{ext}$. The application of a dc external field \mathbf{B}_{ext} allows measurement of the magnetic spin susceptibility. This μ SR configuration is also commonly used to measure the penetration depth in superconductors. With this external field, the counts registered at a positron detector $F(t)$ or $B(t)$, as described in Eq. 2.2 and 2.3 will be modulated by an oscillating component at frequency $\omega_T = \gamma_\mu |\mathbf{B}_{tot}|$:

$$B(t) = N_B e^{-\frac{t}{\tau_\mu}} (1 + A G_x(t) \cos(\gamma_\mu |\mathbf{B}_{tot}| t + \phi)) \quad (2.17)$$

Where $B(t)$ is the counts at a generalized positron detector, shown in Fig. 2.6. In the high field limit, the local field \mathbf{B}_{loc} direction will almost be parallel to \mathbf{B}_{ext} . The asymmetry spectra is then given by:

$$A(t) \propto \cos(\omega_T t) G_x(t) \quad (2.18)$$

TF μ SR is used to characterize the local spin susceptibility in a magnetic system. If there are multiple muon stopping sites with unique magnetic environments within a sample, this will be reflected in the TF asymmetry spectra as several superimposed decaying sinusoidal functions with unique frequencies. A Fourier transform of the TF asymmetry spectra can help resolve these frequencies for data analysis. A more comprehensive survey of the theoretical background of TF measurements can be found in [Riseman 1993].

2.3 Longitudinal Field (LF) μ SR

Application of a magnetic field parallel to the initial muon polarization is known as a longitudinal field (LF). This corresponds to a field along the \mathbf{z} as described in Fig. 2.5. This field will help align a component of the internal local field along this direction. As the magnitude of the field is increased, a non-relaxing component of the asymmetry spectra will develop. This is known as "decoupling". For a static internal field of randomly oriented moments that can be described by the Gaussian Eq. 2.12 with a LF \mathbf{B}_{L} applied, Eq. 2.14 becomes:

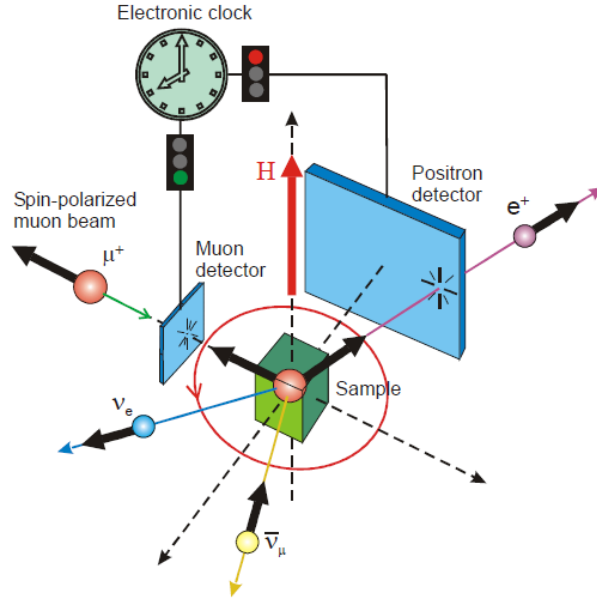


Figure 2.6: Schematic geometry for a transverse field (TF) μ SR experiment. As in other μ SR geometries, a single muon enters the sample area, and an electronic clock is started by its detection. The muon's polarization may be electrostatically tilted perpendicular to its momentum vector, referred to as "spin rotated mode", or may have its polarization antiparallel to its momentum vector, such as shown in this schematic (as in ZF). For both cases, the magnetic field is applied perpendicular to the muon polarization, giving muon precession. The muon hits a positron detector which stops a clock, and a time spectra histogram is built [J.E. Sonier 2001].

$$G_z(t, B_L) = 1 - \left(\frac{2\Delta^2}{\omega_L^2} \right) (1 - e^{\frac{\Delta^2 t^2}{2}} \cos(\omega_L t)) + \left(\frac{2\Delta^4}{\omega_L^3} \right) \int_0^t e^{\frac{\Delta^2 \tau^2}{2}} \sin(\omega_L \tau) d\tau \quad (2.19)$$

Using this, one can use LF measurements to estimate the value of Δ . A more detailed discussion of LF theory can be found in [S.L. Lee 1988].

2.4 μ SR in Magnetic Systems with Dynamic Fields

The previous sections in this chapter focus on systems that have static magnetic field distributions. In practice, this assumption may not be valid. Thermal energy at finite temperature, or quantum mechanical fluctuations can cause magnetic moments to fluctuate. In addition, the muon may diffuse through a magnetic system, "hopping" from site to site such that the local magnetic field it experiences becomes time dependent. Both of these situations can be treated as equivalent. With a time dependent internal field distribution, the muon polarization function can be described as:

$$G_z(t) = \Re \left\{ \overline{\exp \left[i \int_0^t \gamma_\mu B_{loc}(t') dt' \right]} \right\} \quad (2.20)$$

Where $\Re \{ \overline{A} \}$ represents the real component of the statistical average of A [Yaouanc 2011]. The assumption may be made that $B_{loc}(t) = B_{loc} + \delta B_{loc}(t)$. Also, if the external applied field is large enough ($B_{ext} \gg B_{loc}$) the muon Knight shift due to the internal field can be ignored to first order approximation. Applying these assumptions, Eq. 2.20 becomes:

$$G_z(t) = \Re \left\{ \overline{\exp \left[i \int_0^t \gamma_\mu \delta B_{loc}(t') dt' \right]} \right\} \cos(\gamma_\mu B_{ext} t) \quad (2.21)$$

If $B_{loc}(t)$ follows a Gaussian process, then the following simplification is valid:

$$\overline{\exp \left[i \int_0^t \gamma_\mu \delta B_{loc}(t') dt' \right]} = \exp \left[- \int_0^t dt' \int_0^{t'} \overline{\gamma_\mu^2 \delta B_{loc} \delta B_{loc}(t' - t'')} dt'' \right] \quad (2.22)$$

Considering only a special type stochastic processes known as Markovian processes where the "hopping probability" of muons within the system does not depend on time, the following property can be applied:

$$\overline{B_{loc}(t_0) B_{loc}(t_0 + t)} = \overline{B_{loc}^2} \exp(-\nu|t|) \quad (2.23)$$

In the above equation, ν refers to the correlation frequency of B_{loc} , and the overbar represents the weighted average of the corresponding term according to the spacial field distribution of B_{loc} . This relation is known as the Doob theorem [Yaouanc 2011]. Applying this to Eq. 2.22 and simplifying, we get the following relationship:

$$G_z(t) = \exp \left[- \frac{\gamma_\mu^2 \Delta^2}{\nu^2} \int_0^t (t - \tau) \exp(-\nu\tau) d\tau \right] \cos(\gamma_\mu B_{ext} t) \quad (2.24)$$

Where:

$$\Delta^2 \equiv \overline{B_{loc}^2} \quad (2.25)$$

The two asymptotic limits of Eq. 2.24 are relevant to the TF and ZF measurements on $\text{Yb}_2\text{Ti}_2\text{O}_7$ presented in this study in Chapter 5. In the high field limit where the fluctuation rate of spins is very low $\nu t \ll 1$, such that the field distribution is static, we arrive at the equation (Eq. 5.1) used to fit our TF field measurements in this study:

$$G_z(t) = \exp\left(-\frac{\gamma_\mu^2 \Delta^2 t^2}{2}\right) \cos(\gamma_\mu B_{ext} t) \quad (2.26)$$

In the opposite fast fluctuating limit ($\nu t \gg 1$), also known as the "motional narrowing" limit, Eq. 2.24 becomes:

$$G_z(t) = \exp(-\lambda t) \cos(\gamma_\mu B_{ext} t) \quad (2.27)$$

Where:

$$\lambda \equiv \frac{\gamma_\mu^2 \Delta^2}{\nu} \quad (2.28)$$

In zero external field $B_{ext} = 0$,

$$G_z(t) = \exp(-\lambda t) \quad (2.29)$$

Therefore in a system in which spins are completely dynamic and in the narrowing limit $\nu t \gg 1$ with no static domains, the muon asymmetry spectra can be described as a simple exponential decay. The relaxation rate λ is proportional to the timescale of the local magnetic field fluctuations $\tau = 1/\nu$. This is the form used to fit ZF asymmetry spectra in this study, detailed in Chapter 5.

Sample Preparation and Characterization Techniques

Contents

3.1 Optical Floating Zone Crystal Growth of $\text{Yb}_2\text{Ti}_2\text{O}_7$	35
3.1.1 Polycrystalline Rod Preparation	36
3.1.2 Crystal Growth	38
3.2 Specific Heat Measurements	39
3.2.1 Specific heat above 2 K	41
3.2.2 Specific heat below 2 K	42
3.3 Superconducting Quantum Interference Device (SQUID)	43
3.4 X-Ray Diffraction	47

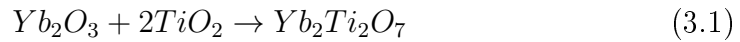
3.1 Optical Floating Zone Crystal Growth of $\text{Yb}_2\text{Ti}_2\text{O}_7$

We grew high quality single crystals of mass ≈ 10 g of $\text{Yb}_2\text{Ti}_2\text{O}_7$ using the NEC optical floating zone furnace at McMaster University. All crystals in this

report that were used for experiments were grown in 2 Atm of O₂, at a rate of approximately 5 mm/hour. In order to grow single crystals of Yb₂Ti₂O₇, sintered polycrystalline rods must first be prepared.

3.1.1 Polycrystalline Rod Preparation

To produce polycrystalline rods of Yb₂Ti₂O₇, high purity (>99.99%) powder of Yb₂O₃ and TiO₂ was preannealed at 400 °C in air for 12 hours to evaporate any aqueous solution. We then mixed Yb₂O₃ and TiO₂ in stoichiometric amounts, as described in Eq. 3.1 – 3.4. The materials were combined with mortar and pestle. The mixture was then placed in a ball mill with zirconium pellets at 400 rpm for 3 five minute intervals with 20 minute breaks in between (to allow heat dissipation) to ensure isotropic mixing. The equations below show the stoichiometry calculations to determine the ratio of Yb₂O₃ to TiO₂ needed to produce Yb₂Ti₂O₇.



$$\left(\frac{1 \text{ mol } Yb_2Ti_2O_7}{553.81 \frac{g}{mol}} \right) \left(\frac{394.08 \frac{g}{mol}}{Yb_2O_3} \right) = 0.712 \frac{g \text{ } Yb_2O_3}{g \text{ } Yb_2Ti_2O_7} \quad (3.2)$$

$$\left(\frac{1 \text{ mol } Yb_2Ti_2O_7}{553.81 \frac{g}{mol}} \right) \left(\frac{2 \text{ mol } TiO_2}{1 \text{ mol } Yb_2Ti_2O_7} \right) \left(\frac{79.867 \frac{g}{mol}}{Yb_2O_3} \right) = 0.288 \frac{g \text{ } TiO_2}{g \text{ } Yb_2Ti_2O_7} \quad (3.3)$$

Combining the above:

$$1 \text{ g } Yb_2O_3 \text{ per } 0.404 \text{ g } TiO_2 \quad (3.4)$$

Eq. 3.4 says for every 1 g of Yb₂O₃, ~ 0.404 g of TiO₂ is required for a stoichiometric mixture of Yb₂Ti₂O₇. The Yb₂O₃ – TiO₂ mixture was then

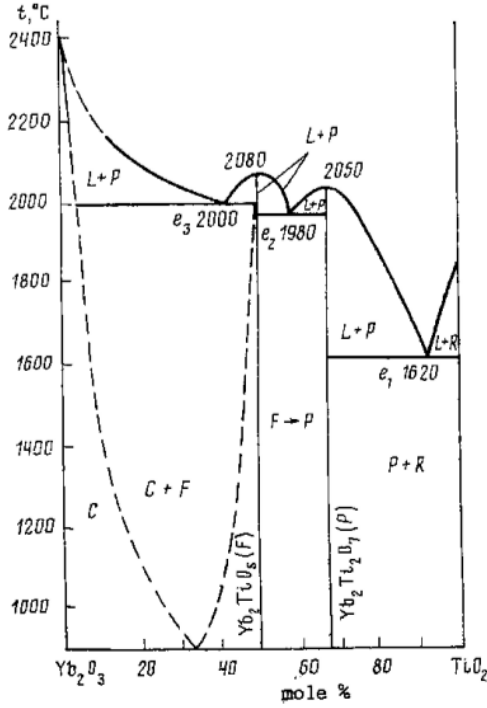


Figure 3.1: Phase diagram of the $\text{Yb}_2\text{O}_3 - \text{TiO}_2$ system. There are two congruently melting phases, $\text{Yb}_2\text{Ti}_2\text{O}_7$ and Yb_2TiO_5 at $2050\text{ }^\circ\text{C}$ and $2080\text{ }^\circ\text{C}$, respectively [Queyroux 1965].

hand packed into a cleaned long rubber tube of diameter $\sim 1\text{ cm}$, evacuated and hydrostatically pressed at 60 MPa for 15 minutes. For Eq. 3.1 to proceed to the right and form $\text{Yb}_2\text{Ti}_2\text{O}_7$, it must be reacted at high temperature. The pressed $\text{Yb}_2\text{O}_3 - \text{TiO}_2$ mixture was again sintered in air at $1200\text{ }^\circ\text{C}$ for 24 hours, with a heating and cooling rate of approximately $100\text{ }^\circ\text{C}/\text{hour}$. To confirm that the phase of the rod is indeed $\text{Yb}_2\text{Ti}_2\text{O}_7$ and not the possible competing phase Yb_2TiO_5 [Queyroux 1965], powder X-Ray diffraction was performed. For details of X-Ray Diffraction techniques, see Section 3.4. The rod was weighed before and after the anneal, to determine if any significant mass loss occurred. For $\text{Yb}_2\text{Ti}_2\text{O}_7$, prepared rods were $\sim 60\%$ of the theoretical density of the final grown single crystal.

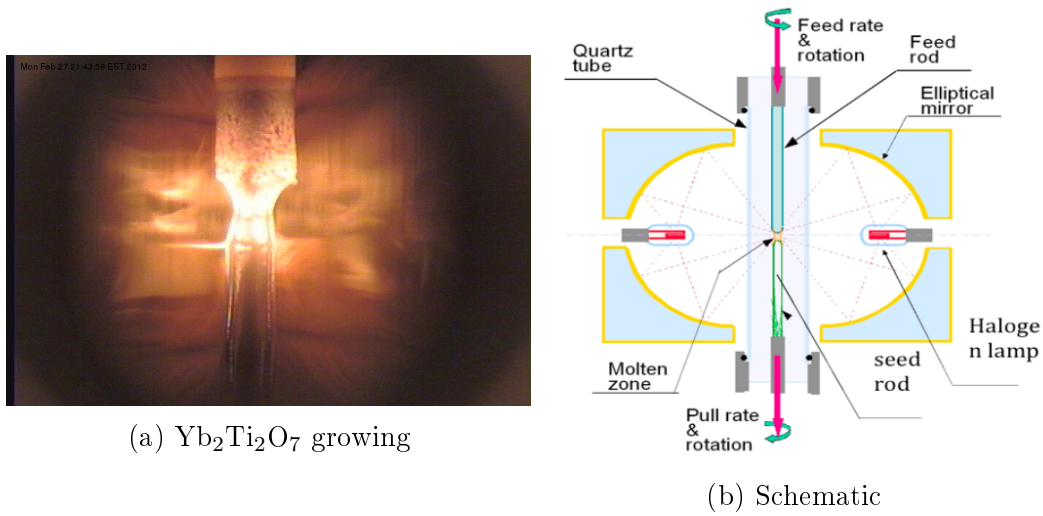


Figure 3.2: (a) shows $\text{Yb}_2\text{Ti}_2\text{O}_7$ in the process of being grown using the optical floating zone furnace at McMaster University. This sample was grown in a 6 Atm O_2 environment, at a rate of ≈ 5 mm/hour. (b) shows a schematic of an optical floating zone furnace. The elliptical mirrors focus light from the halogen bulbs, creating the molten zone. As the polycrystalline feed rod passes through the molten zone, a single crystal is formed.

3.1.2 Crystal Growth

Once the polycrystalline rod was prepared, we mounted it to the top rotating holder in an optical floating zone furnace. On the bottom rotating rod, a base or "seed" of a similar material was mounted, usually another polycrystalline rod of $\text{Yb}_2\text{Ti}_2\text{O}_7$. For the first crystal growth of $\text{Yb}_2\text{Ti}_2\text{O}_7$ in 2 Atm of O_2 , a $\text{Ho}_2\text{Ti}_2\text{O}_7$ ceramic was successfully used as a base. The base is where the grown single crystal sits. For our $\text{Yb}_2\text{Ti}_2\text{O}_7$, no premelt scan at a high speed was done. The premelt scan is usually done to increase the density of the polycrystalline rod, for experimental ease during the single crystal growth. The rods are sealed in a quartz tube chamber, purged and pressurized to 2 Atm of O_2 .

The halogen lamps which provide the heat to melt the $\text{Yb}_2\text{Ti}_2\text{O}_7$ ceramic are focused on the rod tip, and increased at approximately 1% of the max lamp

power (2000 W in the NEC at McMaster University) per minute until the rod melts at $\sim 70\%$ power, or 2050 °C for $\text{Yb}_2\text{Ti}_2\text{O}_7$ (Shown in Fig. 3.1). The rod and seed are then moved in conjunction downwards (not necessarily at the same rate, as the polycrystalline rod will have a smaller density than the forming single crystal) while rotating in opposite directions to ensure good mixing and a thermal equilibrium for heat dissipation. For $\text{Yb}_2\text{Ti}_2\text{O}_7$ the single crystal was formed at ~ 5 mm/hour, and the polycrystalline rod may move downwards at 7–8 mm/hour depending on its final density.

It is interesting to note that the $\text{Yb}_2\text{Ti}_2\text{O}_7$ molten zone has a lower viscosity compared to other pyrochlores, such as $\text{Dy}_2\text{Ti}_2\text{O}_7$. This means establishing a stable molten zone was more difficult, as more frequent adjustments needed to be made to the temperature during the duration of the growth to compensate for the changing thermodynamics of the cooling profile. The initial power requirement to melt the polycrystalline rod may be too hot to establish a stable zone during the crystal growth. In our experience in the NEC furnace at McMaster University, a stable zone required approximately 2% less total power than that required to initially melt the rod. Therefore, once a molten zone was established, the power was gradually decreased 2% over a 10 minute interval.

3.2 Specific Heat Measurements

In this study, we present two sets of specific heat data on $\text{Yb}_2\text{Ti}_2\text{O}_7$. The low temperature specific heat measurements were performed at the University of Waterloo in a dilution refrigerator, in zero applied magnetic field. These measurements compare the thermodynamic transition between polycrystalline

and single crystals grown using the optical floating zone method. The high temperature specific heat $T > 2$ K was performed at McMaster University in applied magnetic fields up to $H=9$ T to observe the field dependence of the Schottky anomaly.

The specific heat or heat capacity of a material is the amount of energy required to raise the temperature by a unit amount, defined as:

$$C = \frac{dQ}{dT} \quad (3.5)$$

Where dQ is the applied heat, and dT is the resultant change in temperature of the material. Specific heat may be used to determine the temperature dependence of the entropy of a system when integrated from $T = 0$ K:

$$S(T) - S(T_0) = \int_{T_0}^T \frac{C(T)}{T} dT \quad (3.6)$$

An important use of specific heat measurements is to observe phase transitions. In condensed matter physics, a wide range of phenomena are represented in the specific heat temperature dependence, such as structural and magnetic phase transitions. Generally, a system will assume the state that best minimizes its free energy F :

$$F = E - TS \quad (3.7)$$

Where E is the enthalpy of a system, and S is the entropy. At low temperature, the enthalpy term dominates. In a water system, the enthalpy is negative in the ice state due to binding forces between water molecules. At high temperatures, the entropy term dominates, so water enters a gas phase maximizing entropy in order to minimize F .

3.2.1 Specific heat above 2 K

For experiments we conducted at McMaster University ($T > 2$ K) in an applied magnetic field, measurements were done in an Oxford Instruments ExaLab. A flat surface of the sample is adhered to a sapphire chip using Apiezon N grease. The sapphire chip contains the heating element and the resistive thermometer. A smooth flat smooth surface is preferred as to ensure good thermal contact. The sample is weakly linked with low thermal resistance to the supporting copper reservoir using thin wires with low thermal conductivity. When the sample is in thermal equilibrium with the reservoir, a set unit of heat is applied via an external power source to the sample and sapphire chip, that causes an increase of temperature of a known amount. The time evolution of the sample’s temperature is then measured as it reaches thermal equilibrium. The specific heat contributions due to the sapphire chip and supporting equipment must be taken into account. The temperature of the copper reservoir is controlled by a gaseous helium bath. The temperature will exponentially decay according to Newton’s cooling law:

$$\frac{dT}{dt} \propto -(T_S - T_R) \quad (3.8)$$

Where T_S is the sample temperature and T_R is the reservoir temperature. The solution is described by a simple exponential decay:

$$\Delta T(t) = T_o + A(1 - e^{-\frac{t}{\tau}}) \quad (3.9)$$

Where T_o is the temperature before the heat pulse is applied, and the proportionality constant A depends on the input heat pulse power and the dimensions of the sample [Kittel 2005, Woods 2000]. This constant is usually

experimentally determined. The specific heat $C(T)$ can then be extracted from the decay constant $\tau(T) = R_{TH}C(T)$ where R_{TH} is the effective thermal resistance of the sample, experimentally determined by $R_{TH} = \Delta T/\Delta P$. ΔT is the net change in temperature of the sample, and ΔP is the power supplied in the heat pulse. The specific heat of the glue (Apiezon N at McMaster University) and addendum must also be experimentally measured and numerally subtracted. The magnetic field is applied parallel to the sample plane in contact with the thermal reservoir using a superconducting magnet that can reach $H = 9$ T [Woods 2000].

3.2.2 Specific heat below 2 K

To characterize the transition viewed at ~ 265 mK (for the polycrystal sample - Fig. 4.4) specific heat measurements were performed at University of Waterloo by David Pomaranski and Jan Kycia. In order to reach this low temperature regime, a dilution refrigerator must be used. To cool below the limit of approximately 1.8 K provided by pumping on a conventional Helium-4 cryostat, the extra cooling power to reach the mK scale is provided by the enthalpy of mixing Helium-4/Helium-3.

Besides the more sophisticated cryogenics, the principles of the specific heat measurement are similar to those used in measurements performed above 2 K, described in the previous section. The sample is allowed to reach thermal equilibrium, and a heat pulse is applied and the thermal relaxation observed according to Eq. 3.9. This relaxation method represents the specific heat quantitatively, but is limited by long timescales τ at very low temperatures. There may be several different time constants, viewed as superimposed exponential decays associated with the experimental apparatus that must be accounted

for. Generally, the time constant increases as temperature is lowered. For $\text{Yb}_2\text{Ti}_2\text{O}_7$, it can reach hours [Y. Yasui 2003] at very low temperatures, such that a single measurement of the specific heat at one temperature via the relaxation method will be on the order of days. Measurements were performed in a similar fashion to those presented in [Quilliam 2007], however a slightly different technique was used, known as the "sweep" technique. The basic principle of the sweep method is the sample is heated to a higher temperature using a thermal link with known thermal conductivity. The sample is then allowed to cool to base temperature, and the specific heat is proportional to the rate of cooling. This method represents the data qualitatively, such that the magnitude can then be calibrated using conventional relaxation method data points.

3.3 Superconducting Quantum Interference Device (SQUID)

Superconducting Quantum Interference Devices (SQUID) allow extremely sensitive measurements of magnetic fields, with sensitivity as low as 5×10^{-18} T [Kittel 2005]. There are two common variants, the direct current (DC), and radio frequency (RF) SQUID. Experiments in this report were conducted using an RF SQUID measuring the DC magnetization.

An RF SQUID magnetometer consists of a superconducting ring with one Josephson Junction, coupled with an Inductor Capacitor (LC) circuit. A Josephson Junction is a non-superconducting material (usually an insulator) sandwiched between two superconductors, forming a weak link.

The superconducting ring with the Josephson Junction exploits the prin-

ciple of magnetic flux quantization. From quantum mechanics, flux through a superconducting loop must be quantized into integer units of: $\Phi = h/2e$. The superconducting ring broken by the Josephson Junction is the SQUID component of the magnetometer. The phenomena that allows sensitive measurements of the dc-magnetic susceptibility is called the Josephson effect, where the quantum mechanical tunneling of electron pairs across the non-superconductor (or insulator) weak occurs. The RF SQUID magnetometer is based on the AC Josephson effect [Kittel 2005]. The AC Josephson effect produces an AC current when a fixed DC voltage is incident across the Josephson Junction.

If we consider an insulator sandwiched between two superconductors, it will have some probability P for an electron pair to tunnel across the barrier.

$$P \sim e^{-2\gamma}, \gamma = \frac{1}{\hbar} \int_x \sqrt{2m(V(x) - E)} dx \quad (3.10)$$

This equation tells us the tunneling probability decreases exponentially with the energy barrier height $V(x)$, and the thickness of the barrier x . The wave function of electrons inside each superconducting section to the left and right of the insulator is denoted ψ_1 and ψ_2 respectively. For the AC Josephson effect, a DC voltage is applied across the gap. Applying Schroedinger Equation gives:

$$i\hbar \frac{d\psi_1}{dt} = \hbar t \psi_2 - eV \psi_1 \quad (3.11)$$

$$i\hbar \frac{d\psi_2}{dt} = \hbar t \psi_1 - eV \psi_2 \quad (3.12)$$

Assuming that the tunneling probability is the same in both directions across the barrier. The exact form of ψ_1 and ψ_2 is not known, all that is important is that the wave functions are proportional to the probability amplitude for electron pairs. For this purpose, the following form for the wave function can be used:

$$\psi_w = \sqrt{n_w} e^{i\phi_w} \Rightarrow w = 1, 2 \quad (3.13)$$

Where n_1 and n_2 are the density of electron pairs in each superconducting section, and ϕ is the phase of each respective wave function. Substituting this in this waveform into the differential Schroedinger form above yields:

$$\frac{dn_1}{dt} = 2T \sqrt{n_1 n_2} \sin \delta \Rightarrow \delta \equiv \phi_1 - \phi_2 \quad (3.14)$$

Making the assumption that $n_1 \approx n_2$, such that the number of pairs that tunnel is small compared to the overall pair density in the superconductor, we get the following relationship for δ , the phase difference between the wave functions in the two superconducting regions:

$$\delta(t) = \delta(0) - \frac{2eV}{\hbar} t \quad (3.15)$$

The Josephson current $J(t)$ is proportional to the rate that electron pairs cross the insulating barrier. Combining the two above equations yields the form of the AC Josephson current.

$$J(t) \propto \frac{dn_1}{dt} = 2T \sqrt{n_1 n_2} \sin \left[\delta(o) - \frac{2eV}{\hbar} t \right] \quad (3.16)$$

Therefore, with a fixed DC voltage V applied across the Josephson Junc-

tion, an AC current will arise with frequency $2eV/\hbar$ [Kittel 2005]. This time dependent current arises from the change in phase δ between the wave function in each superconducting section.

The magnetic flux through the SQUID ring is related to the phase of the wave function by:

$$\delta = \frac{2e}{\hbar c} \Phi \quad (3.17)$$

Therefore, a change in the magnetic flux Φ through the ring will result in a measurable change in the current through the junction. The changes in current due to magnetic flux is then amplified and measured. A SQUID ring alone can detect changes in magnetic fields without any extra electronics, but in practice, some type of flux transformer circuit is used. The most basic flux transformer circuit contains two inducting coils, both cooled to a superconducting state. The coil that measures the second component of the RF SQUID magnetometer is the LC circuit, sometimes referred to as the "tank" circuit. The LC circuit has a specific frequency at which maximum power is used, known as the resonant frequency. The resonant frequency depends on the inductance and capacitance of the circuit, and is chosen to be around 20-30 MHz for an RF SQUID. This means a shift in the AC current frequency through the Josephson junction can be detected through a change in power dissipation of the tank circuit.

At McMaster University, the Quantum Design squid uses a Reciprocating Sample Oscillator (RSO). The sample oscillates through four pick up coils oriented such that the outer coils are wound in the opposite direction as the inner coils. This arrangement acts as a second order gradiometer and takes into account of stray magnetic fields and external applied fields. To center the

sample in the coils, an induced voltage vs position graph is measured. When a magnetic sample is moved through the coils, an AC current is induced with the frequency of the sample's oscillation. A lock in amplifier and SQUID loop are then used to accurately determine the magnetic moment of the sample. The SQUID magnetometer was used to perform magnetic susceptibility measurements χ of $\text{Yb}_2\text{Ti}_2\text{O}_7$.

3.4 X-Ray Diffraction

X-Ray diffraction (XRD) techniques provide a powerful tool to characterize the quality, crystal structure, number of grains (for a crystal sample), stoichiometry and phase of a sample. XRD may also be used to probe the physics of materials, such as inelastic techniques to determine electronic band structures. To determine the crystal axis orientation, Laue X-Ray diffraction is used. For diffraction to occur, the difference between the incident x-ray wave vector \mathbf{k}_i and reflected wave vector \mathbf{k}_f in momentum space must be equal to a reciprocal lattice vector \mathbf{G} of the sample, satisfying Eq. 3.18.

$$\mathbf{k}_f - \mathbf{k}_i = \mathbf{G} \quad (3.18)$$

If $\mathbf{a}_1, \mathbf{a}_2, \mathbf{a}_3$ are components of the lattice vectors of a crystal, and $\mathbf{g}_1, \mathbf{g}_2, \mathbf{g}_3$ are components of the reciprocal lattice vector \mathbf{G} , taking the scalar product of $\mathbf{a}_1, \mathbf{a}_2, \mathbf{a}_3$ and the above equations, along with $\mathbf{a}_i \cdot \mathbf{g}_j = 2\pi\delta_{i,j}$ we get the Laue equations ??.

$$\mathbf{a}_i(\mathbf{k}_f - \mathbf{k}_i) = 2\pi\mathbf{g}_w, w = 1, 2, 3 \quad (3.19)$$

A reflection of x-rays $\mathbf{k}_f - \mathbf{k}_i$ must satisfy all 3 equations above, which requires a single incident wavelength. A monochromatic x-ray source will only produce diffraction peaks at a detector when Eq. 3.18 is satisfied. When a "white" x-ray source that produces a continuous range of wavelengths is used, the above equation will be satisfied. This is the basic principle of Laue x-ray diffraction. An illustration of this is shown in Fig. 3.3.

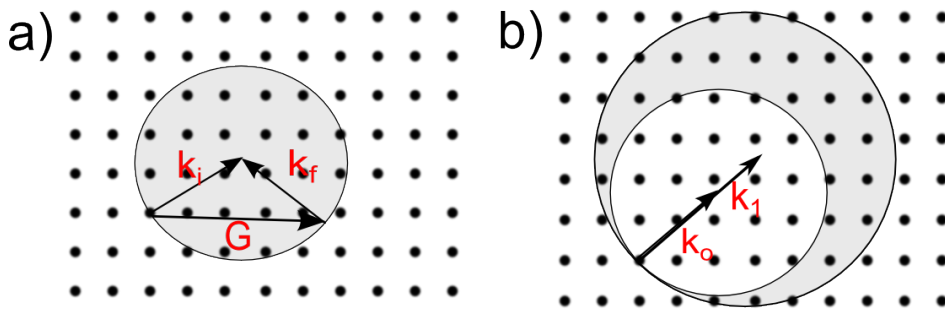


Figure 3.3: Visualization of Laue diffraction works using the Ewald Construction. The black points represent the reciprocal lattice in k space. In figure a) a monochromatic source is used, so $\mathbf{k}_f - \mathbf{k}_i$ is satisfied only if a reciprocal lattice point lies directly on the surface of the gray Ewald sphere. In figure b) the incident wave vector ranges from \mathbf{k}_0 to \mathbf{k}_1 so that all reciprocal lattice points that lie in the volume contained by these two spheres will meet the Bragg condition. These points are represented by all of the points lying within the gray section.

If the incoming x-ray is parallel to a high symmetry direction in the crystal, the Laue diffraction pattern will have a corresponding symmetry. For example, if \mathbf{k}_i is along a $[100]$ direction in a simple cubic crystal, the resulting Laue pattern recorded on the detector will have a four fold symmetry [Kittel 2005].

Another form of XRD used in this study to determine the phase and quality of samples is powder X-Ray diffraction. The sample is crushed into a polycrystalline powder. A single wavelength of incident X-Rays is used, and the 2Θ angle is varied. As the sample was ground into a powder, the

diffraction pattern is averaged over all crystallographic directions. This is equivalent to projecting the 3D reciprocal space into one dimension. Point like Bragg peaks are averaged over all angles, such that they are smeared into rings of diffraction. Details and results of XRD experiments are presented in Chapter 4.

Characterization Results

Contents

4.1	Verification of Phase through Powder XRD	51
4.2	dc-magnetization Results	53
4.2.1	Determining the Curie-Weiss Temperature	54
4.3	Specific Heat Results	56
4.3.1	Zero Field Specific Heat $30 \text{ mK} < T < 400 \text{ mK}$	57
4.3.2	In Field Specific Heat $2 \text{ K} < T < 20 \text{ K}$	58

4.1 Verification of Phase through Powder XRD

To verify the grown single crystal via the optical floating zone method is indeed $\text{Yb}_2\text{Ti}_2\text{O}_7$ and not a competing phase such as Yb_2TiO_5 , as shown in [Queyroux 1965], we performed powder X-Ray diffraction (XRD) using the Debye-Scherrer method on the PANalytical XPert Powder Diffractometer at McMaster University. Powder samples or crushed single crystals were adhered to the rotating sample disk using a mixture of an organic solvent and petroleum jelly. A small amount of ground Si provided a reference diffraction peak. Unlike Laue X-Ray diffraction described in Chapter 3, powder XRD

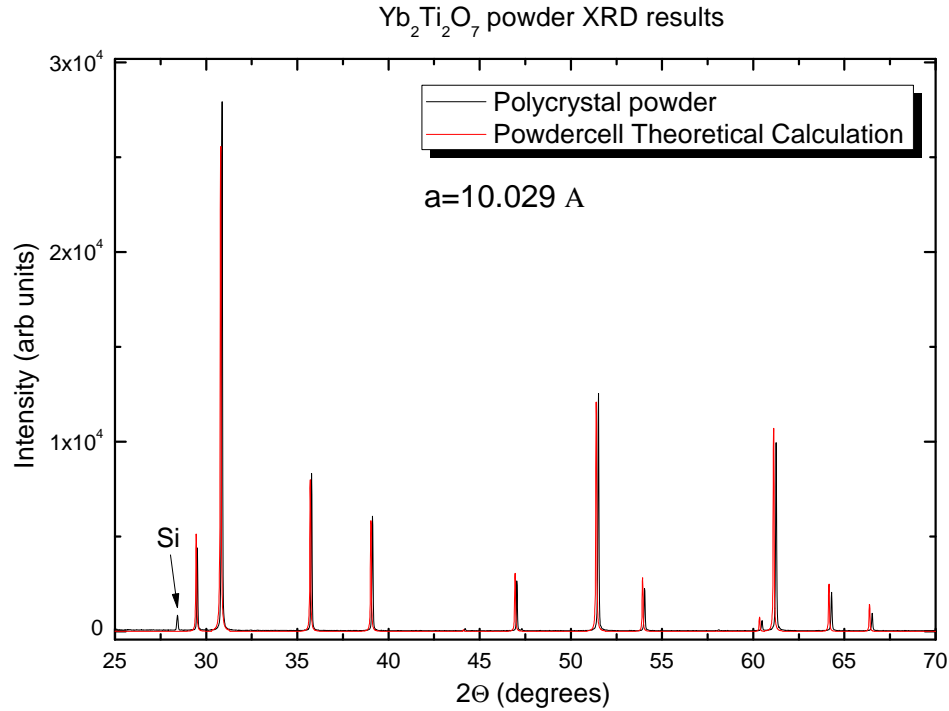


Figure 4.1: XRD spectra of polycrystalline $\text{Yb}_2\text{Ti}_2\text{O}_7$ (before crystal growth), confirming the phase to be $\text{Yb}_2\text{Ti}_2\text{O}_7$. Rietveld refinement of the data gives a lattice constant of $10.029 \pm 0.001 \text{ \AA}$.

uses a single incident wavelength, and varies the 2Θ angle. Since the sample was ground into a powder, the diffraction pattern is averaged over all crystallographic directions. This is equivalent to projecting the 3D reciprocal space into one dimension. The distinct points of a Laue diffraction pattern will be averaged into "rings" of diffraction.

The experimentally obtained XRD pattern shown in Fig. 4.1 was compared to a theoretically obtained spectra using the Wyckoff numbers and an initial estimate of the lattice constant a given in Chapter 1 [J.S. Gardner 2010]. The lattice constant and an estimate of the stoichiometry can be determined by a Rietveld refinement of the amplitude and spacing of the Bragg diffraction pattern. The sample grown using the optical floating zone was verified to be

$\text{Yb}_2\text{Ti}_2\text{O}_7$, with a lattice constant of $a = 10.029 \pm 0.001 \text{ \AA}$.

4.2 dc-magnetization Results

We performed measurements of the dc magnetic susceptibility of both polycrystalline and several orientations of $\text{Yb}_2\text{Ti}_2\text{O}_7$ in a SQUID magnetometer (introduced in Chapter. 3). The Quantum Design SQUID at McMaster University contains a conventional Helium-4 cryostat with a base temperature of $\sim 1.8 \text{ K}$, therefore $\text{Yb}_2\text{Ti}_2\text{O}_7$ was in the paramagnetic regime for all measurements. A magnetic field up to $H = 5 \text{ T}$ was applied to the [100], [110] and [111] crystallographic directions, several of which are shown in Fig. 4.2. As expected from the cubic structure of $\text{Yb}_2\text{Ti}_2\text{O}_7$ and the magnetic degrees of freedom in the exchange tensor [K.A. Ross 2009], there is little magnetic anisotropy between the different measured directions. The small anisotropy observed is more pronounced at lower applied fields (displayed in the inset of Fig. 4.2), but may be due to a misalignment of the magnetic field (the orientation of the crystal has uncertainty $\pm 2^\circ$), or possibly uncertainty in the applied field due to trapped flux in the superconducting magnet. Also it is important to note that no demagnetization correction was applied to the data to take into account the shape of the sample. For our results shown in Fig. 4.2, we cut the sample such that all three crystallographic directions measured were in the sample plane, such that the sample just had to be rotated in between measurements. This also ensures the demagnetization correction would be similar.

The data exhibits typical Curie behavior for a paramagnetic material, monotonically decreasing as $\propto (T - \Theta_{CW})^{-1}$ (where Θ_{CW} is the Curie-Weiss

temperature) over the measured temperature range $1.8K \leq T \leq 20K$.

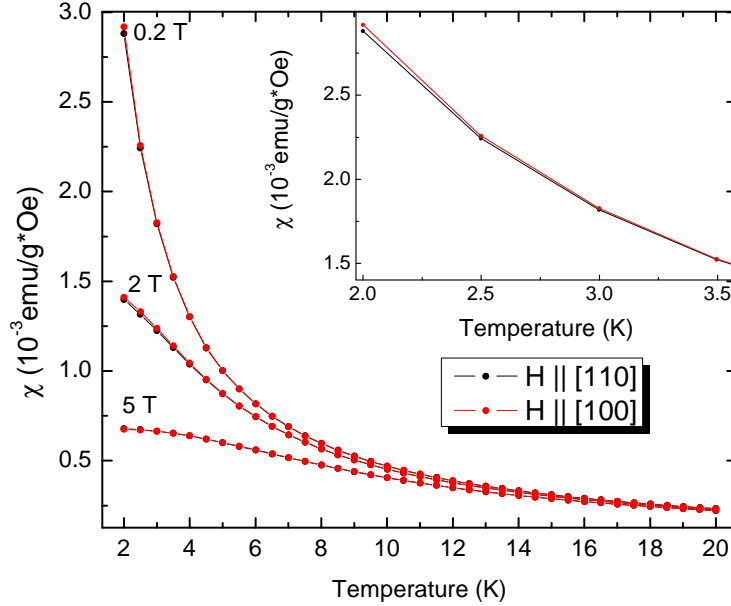


Figure 4.2: Magnetic susceptibility of single crystal $\text{Yb}_2\text{Ti}_2\text{O}_7$ along $[100]$ and $[110]$ directions in applied field up to $H=5$ T. As expected due to the cubic nature of the pyrochlore lattice, there is very small anisotropy between the crystallographic directions, which may be an artifact of the data. Inset: a zoom in of the magnetic susceptibility at $H = 0.2$ T to emphasize the small magnetic anisotropy.

4.2.1 Determining the Curie-Weiss Temperature

The Curie-Weiss law describes the temperature dependence of a ferromagnetic or antiferromagnetic material's magnetic susceptibility in the paramagnetic regime using a mean field approximation. The Curie-Weiss law is described as:

$$\chi(T) = \frac{A}{T - \Theta_{CW}} \quad (4.1)$$

Where A is known as the Curie Constant given by $A = \frac{\mu_B^2}{3k_B} N g^2 J(J + 1)$ where N is the number of magnetic moments, k_B is the Boltzmann's constant (1.3806×10^{-23} J/K), g is the Landé g-factor and J is the angular momentum quantum number.

For a ferromagnetic material in the mean field approximation, $\Theta_{CW} = T_C$ is known as the Curie temperature and $T_C > 0$. For an antiferromagnetic material, the critical temperature is referred to as the Néel temperature, where $\Theta_{CW} = T_N$ and $T_C < 0$ in the mean field approximation. The magnitude of the temperature is proportional to the strength of the the magnetic interactions [Kittel 2005].

From Eq. 4.1, a plot of $\chi(T)^{-1}$ will yield a linear relationship, of which the horizontal intercept gives Θ_{CW} . A plot of $\chi(T)^{-1}$ vs T of single crystal $\text{Yb}_2\text{Ti}_2\text{O}_7$ with a magnetic field of $H = 50$ mT applied parallel to a [111] direction is shown in Fig: 4.3. $H = 50$ mT was chosen to compare to TF μSR measurements, presented later in Chapter. 5.

Fig. 4.3 shows the mostly linear behavior of $\chi(T)^{-1}$ down to approximately 2 K. Three separate linear fits were performed over the data using different temperature ranges to illustrate the variation in the resulting Θ_{CW} . This temperature dependence suggests there are competing interactions as the transition observed in the specific heat $T \sim 185$ mK for this single crystal (Fig. 4.4). The temperature dependence of T_C will be revisited in Chapter. 5 with a comparison to μSR results. Overall, the magnetic susceptibility agrees with previous measurements first performed in [H.W.J. Blote 1969] with $T_C = 0.4 \pm 0.1\text{K}$ when fit using the low temperature data.

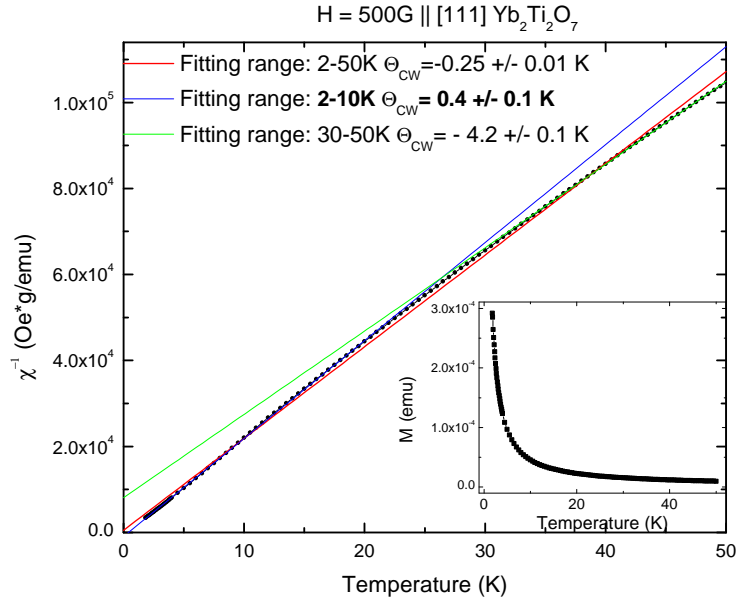


Figure 4.3: Temperature dependence of the inverse magnetic susceptibility of single crystal $\text{Yb}_2\text{Ti}_2\text{O}_7$ aligned such that the applied field $H=500$ G is parallel to a $[111]$ crystallographic direction, as measured in the SQUID at McMaster University. This is the same sample that was used for all μSR experiments. Linear fits are done on different temperature ranges to show that the Curie–Weiss temperature is not constant. The inset displays the magnetic moment temperature dependence.

4.3 Specific Heat Results

Here the specific heat measurements are presented in two sets, the low temperature measurements of both polycrystalline and single crystal $\text{Yb}_2\text{Ti}_2\text{O}_7$ in zero applied magnetic field, measured at the University of Waterloo from $30 \text{ mK} < T < 400 \text{ mK}$. The second sets presents the evolution of the Schottky anomaly in an applied magnetic field up to $H = 9$ T performed at McMaster University at temperatures $2\text{K} < T < 20\text{K}$. The specific heat above 30 K is largely dominated by a phonon contribution, and was not measured.

4.3.1 Zero Field Specific Heat $30 \text{ mK} < T < 400 \text{ mK}$

Fig. 4.4 presents the low temperature specific heat data of two $\text{Yb}_2\text{Ti}_2\text{O}_7$ samples, the single crystal shown in blue, and the polycrystalline sample in red, plotted on a semilogarithmic scale. The thermodynamic transition has very different behavior before and after growth using the optical floating zone method. The polycrystalline sample has a sharp transition at $T \sim 265 \text{ mK}$, where the single crystal’s transition is broadened and pushed down to peak at $T \sim 185 \text{ mK}$, with an overall amplitude approximately 25 times less.

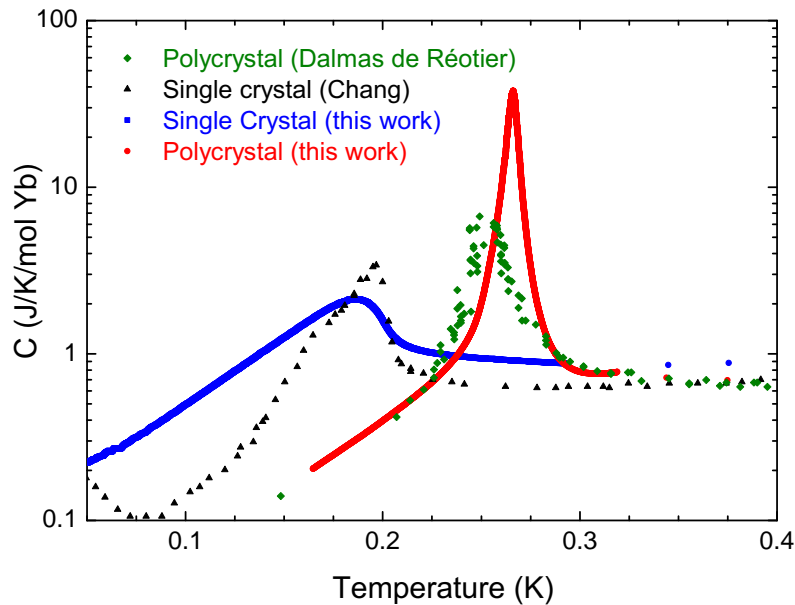


Figure 4.4: The low temperature specific heat measurements of polycrystalline (red) and single crystal (blue) $\text{Yb}_2\text{Ti}_2\text{O}_7$, performed at the University of Waterloo using a combination of the relaxation method (described above) and the sweep method. For comparison, digitized versions of specific heat results of samples used in studies by Chang *et al.* [L.-J. Chang 2012] (black triangles) and Dalmas de Réotier *et al.* (green diamonds) are included. Taken from [R.M. D’Ortenzio 2013].

Included in Fig. 4.4 are digitized data taken from measurements

by Dalmas de Réotier *et al.* [P. Dalmas de Réotier 2006] and Chang *et al.* [L.-J. Chang 2012] for comparison. Is it evident from the range of transition temperatures, that samples prepared in this study are extreme cases of sample variation in $\text{Yb}_2\text{Ti}_2\text{O}_7$. With respect to the stuffed pyrochlore model put forward by Ross *et al.* [K.A. Ross 2012] we would expect the polycrystalline ceramic which exhibits a sharp transition at $T \sim 265$ mK, similar to Ross's sample, to be close to ideal stoichiometry ($x \approx 0$ in Eq. 1.3). On the other hand, our single crystal would exhibit a large degree of stuffing, probably $\sim 0.046(4)$, as the single crystal samples used in [K.A. Ross 2012] show a similar transition temperature ($T \sim 185$ mK) in the specific heat. Ross *et al.* predicts that different degrees of lattice defects in samples will strongly effect the magnetic ground state. Therefore by comparing these two extreme cases of sample dependence in $\text{Yb}_2\text{Ti}_2\text{O}_7$, a direct connection can be made between the low temperature magnetism and specific heat measurements. The reader will see that our ZF μSR results presented in Chapter 5 indicate both samples have strikingly similar dynamic low temperature behavior with no long range magnetic order.

4.3.2 In Field Specific Heat $2 K < T < 20 K$

To observe the evolution of the Schottky anomaly in an applied field, specific heat measurements were taken up to $H = 9$ T parallel to a $[110]$ crystallographic direction at temperatures $2 K < T < 40 K$. The results are presented in Fig. 4.5. As the applied field was increased, the peak temperature of the Schottky anomaly monotonically increased, and the amplitude decreased with respect to the background phonon T^3 contribution. In addition, the anomaly width increases with applied field. Independent of applied field, we would

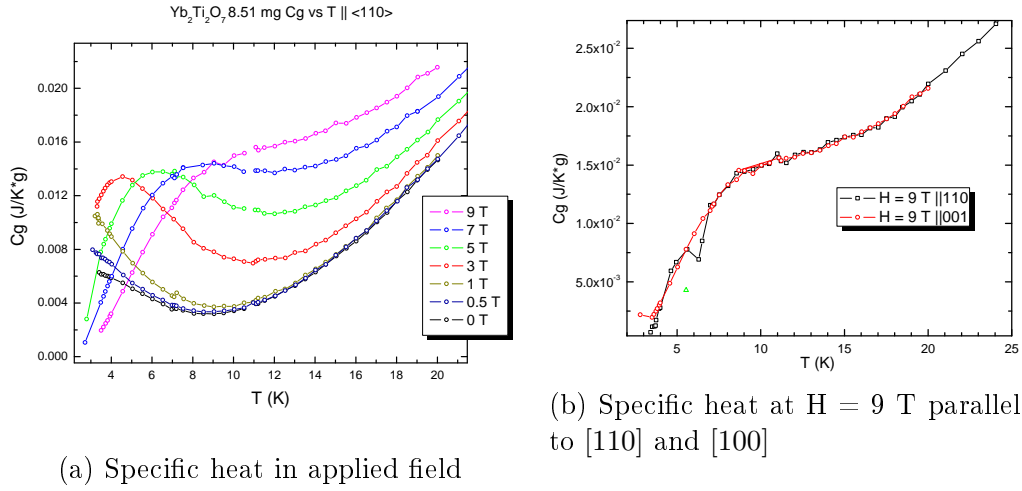


Figure 4.5: (a) shows the specific heat measurements of single crystal Yb₂Ti₂O₇ up to H=9 T, with the field parallel to a [110] crystallographic direction. (b) shows a comparison of specific heat data taken with the field H = 9 T applied parallel to the [110] and [100] directions.

extrapolate that the specific heat converges to a common temperature dependence at approximately 30 - 40 K for all measurements. Fig. 4.6 shows our measurements taken to at least 30 K, showing this is the approximate temperature range when the data becomes independent of applied field. Like the dc magnetic susceptibility measurements, the in-field specific heat has little directional anisotropy. Fig. 4.5 (b) compares specific heat data taken with the field H = 9 T applied parallel to the [110] and [100] directions. Within the noise of the data, there is no significant difference. This is true in all applied fields employed.

To clearly illustrate the field dependence of the Schottky anomaly, we show a contour plot of the data in Fig. 4.5 in Fig. 4.7. The "warmer" colors represent higher specific heat. Generally, the peak of the Schottky anomaly increases in temperature as applied field was increased.

In order to compare this data to the theoretically calculated specific heat

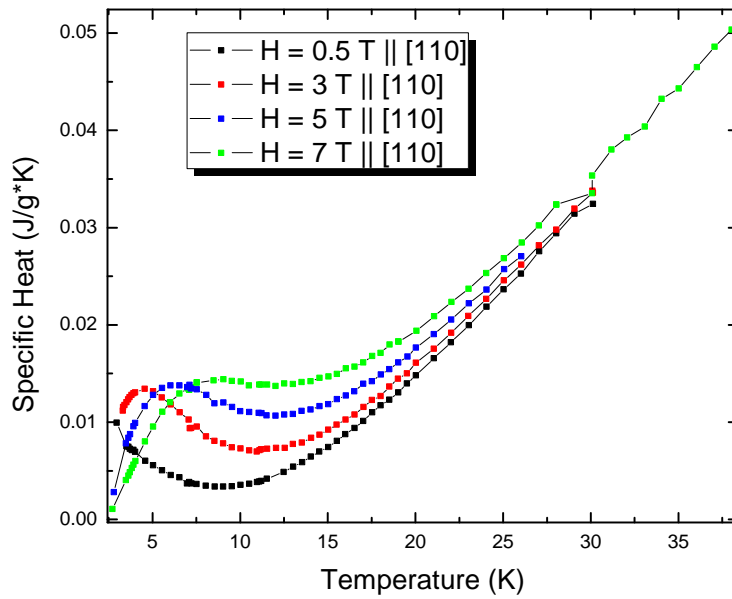


Figure 4.6: Specific heat measurements conducted at least up to 30 K, to give an approximation of where data becomes field independent.

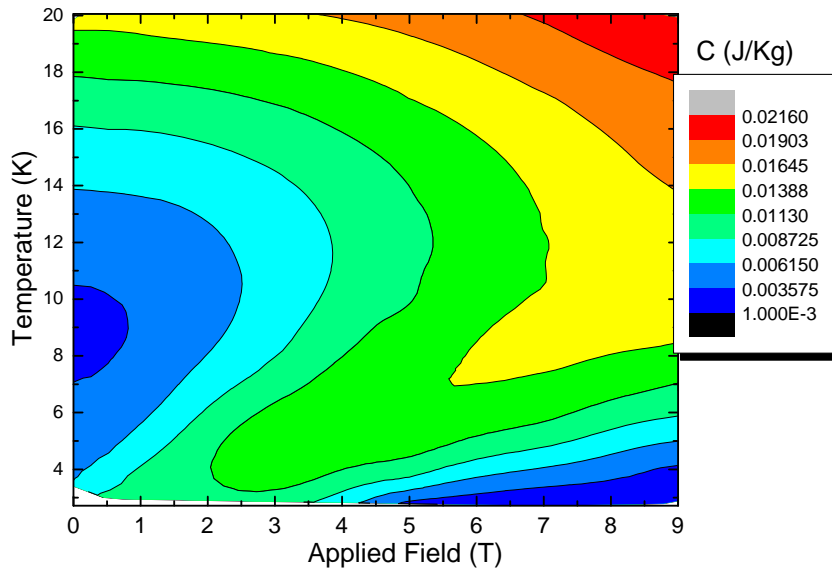


Figure 4.7: A contour plot of specific heat in an applied field.

by Applegate *et al.* [Applegate 2012], the phonon contribution must be removed, as Applegate *et al.* only consider the magnetic field dependent contribution to the specific heat. Generally, at temperatures much lower than the Debye temperature, the free electronic Fermi contribution to the specific heat is linearly proportional to temperature, and the phonon contribution depends on the temperature cubed:

$$C(T) = \gamma T + \beta T^3, \frac{C(T)}{T} = \gamma + \beta T^2 \quad (4.2)$$

Where γ and β are sample dependent constants. For an insulating material, the free electron contribution should $\gamma = 0$. Therefore a plot of $C(T)/T$ vs T^2 can be fit with a linear function, where the slope gives the magnitude of the phonon contribution β . No Debye temperature for $\text{Yb}_2\text{Ti}_2\text{O}_7$ could be found in published literature, however we would expect it to be similar to the nonmagnetic pyrochlore $\text{Y}_2\text{Ti}_2\text{O}_7$, which has a Debye temperature of $\Theta_D = 970$ K [M.B. Johnson 2009]. These plots with a linear fit of the high temperature data is given in Fig. 4.8. The extracted β and γ parameters are plotted as a function of applied field in Fig. 4.9. The phonon contribution should be independent of the applied field, which is not true for our specific heat measurements. Measurements taken at $H = 0.5$ T, 3 T and 5 T have a β value of $\beta \approx 1.3 \pm 0.2$ J/gK⁴, and are only slightly field dependent when uncertainties are considered (plotted in Fig. 4.9). However, the $H = 1$ T run has a very different measured β value of $\beta \approx 2.97 \pm 0.04$ J/gK⁴. We believe that this is because this measurement was not taken to high enough temperature, such that it is not in the T^3 regime. The linear fit for $H = 1$

T was performed between $12K \leq T \leq 20K$ where the other measurements were fit $20K \leq T \leq 30K$. In addition, the γ value for $H = 1$ T is notably different than the other applied fields. In Figure 4.9 the field dependence of the β and γ parameters are plotted, showing the large change for the $H = 1$ T measurement.

Theoretically, because $\text{Yb}_2\text{Ti}_2\text{O}_7$ is an insulator, the free electron Fermi contribution to the specific heat should be zero. The nonzero intercepts of linear fits shown in Fig. 4.8 suggest that there is an unknown contribution to the specific heat that has linear temperature dependence. This contribution is due to some unknown magnetic excitation.

Figure 4.10 directly compares the theoretical specific heat presented in [Applegate 2012] with our experimental data. For $H = 5$ T and $H = 1$ T, the data is in general qualitative agreement down to the lowest temperatures measured. Although in Fig. 4.8 shows good agreement to the linear fits, (shown as red lines) for some measurements (particularly $H = 3$ T and $H = 0.5$ T between $10K \leq T \leq 20K$) the specific heat dips below this red line. This means that this contribution to the specific heat is not only due to phonons, but also contains an additional part from some type of field dependent magnetic excitations. This is why when both components γ and β are subtracted from our measurements and compared to Applegate *et al.*'s [Applegate 2012] calculations as shown in Figure 4.10, our resulting data becomes negative for $H = 3$ T and $H = 0.5$ T.

An alternative method to compare our specific heat measurements with calculations by Applegate *et al.* [Applegate 2012] is to subtract the entire $H = 0$ T measurement. Applegate *et al.* only consider the field dependent component of the Schottky anomaly, so this method promises a good compari-

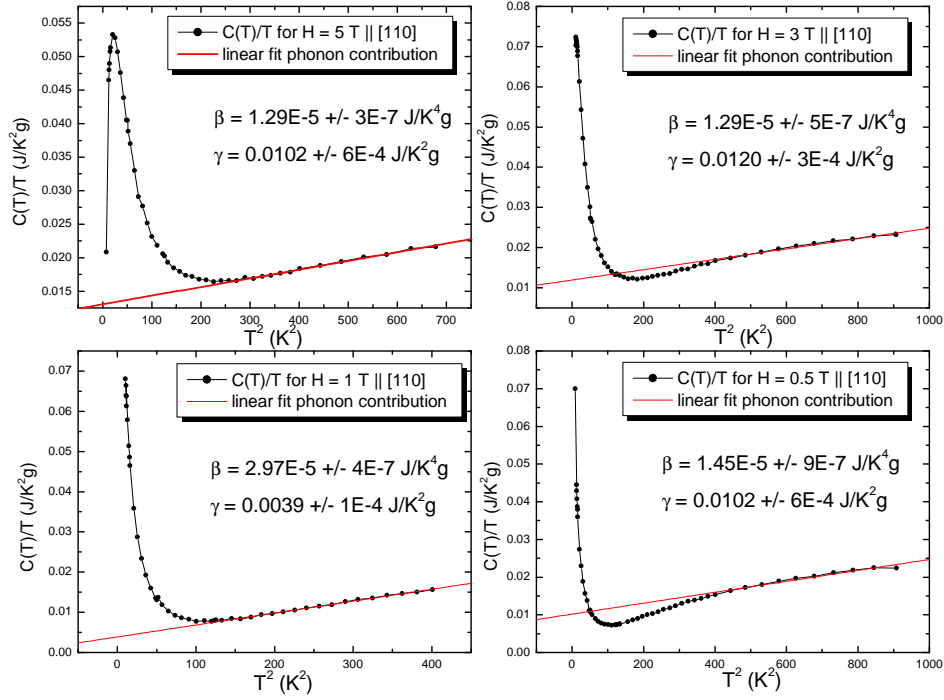


Figure 4.8: Plots of $C(T)/T$ vs T^2 of single crystal $\text{Yb}_2\text{Ti}_2\text{O}_7$ in a field of $H = 0.5 \text{ T}$, 1 T , 3 T and 5 T applied parallel to a $[110]$ crystallographic direction. This plot is included to show the linear fit as to subtract the phonon contribution of the specific heat. The extracted parameters γ and β from Eq. 4.2 for each fit are included. Notice for the two images on the right side where $H = 0.5 \text{ T}$ and $H = 3 \text{ T}$, there is a temperature range where the specific heat dips below the red linear fits.

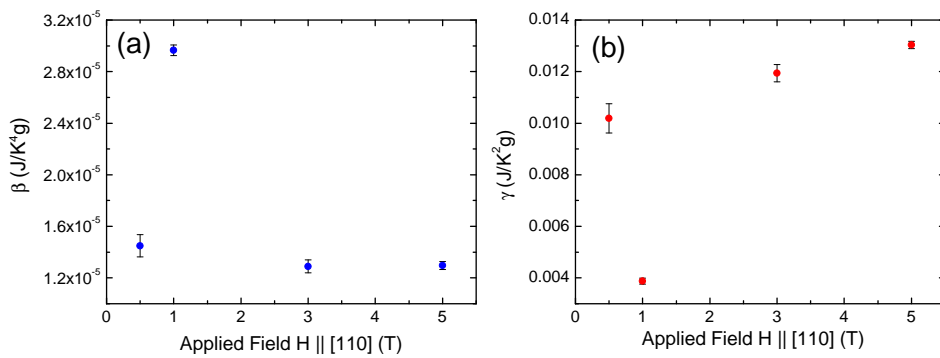


Figure 4.9: Field dependence of parameters β (a) and γ (b) from Eq. 4.2 extracted from specific heat data. The magnetic field is applied along a $[110]$ direction. The $H = 1 \text{ T}$ measurement shows significantly different parameters, as it was fit using a different temperature range.

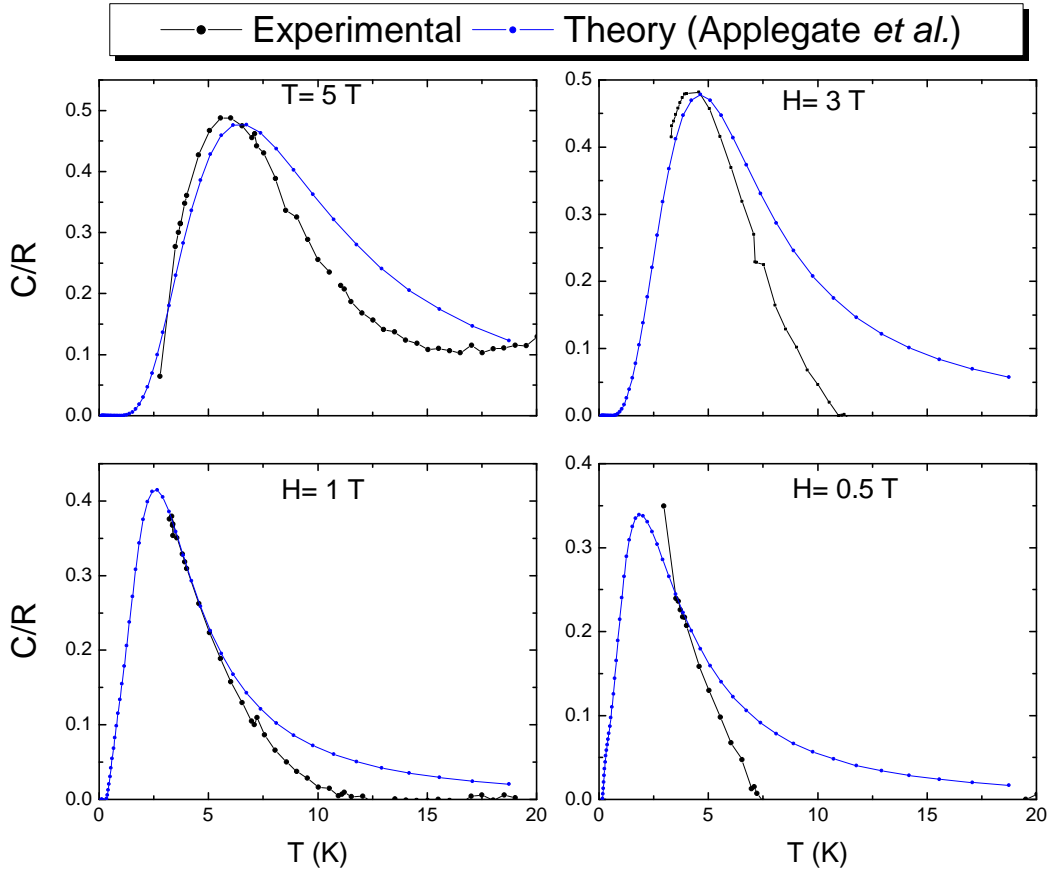


Figure 4.10: Comparison of theoretical data taken from Applegate *et al.* [Applegate 2012] and experimental data taken at McMaster University, with the T^3 phonon contribution subtracted.

son by guaranteeing removal all other components. The results of this analysis are shown in Figure 4.11. This technique shows good qualitative agreement for all applied fields across the temperature range of the Schottky anomaly.

It is difficult to draw conclusions from the temperature evolution of the Schottky anomaly and its implications to the theory proposed by Applegate *et al.* [Applegate 2012]. Their calculations using the numerical linked-cluster method (NLC) attribute the Schottky anomaly to a crossover from the paramagnetic phase to a temperature region dominated by quantum mechanical fluctuations. The authors note they were only focusing on calculating the high

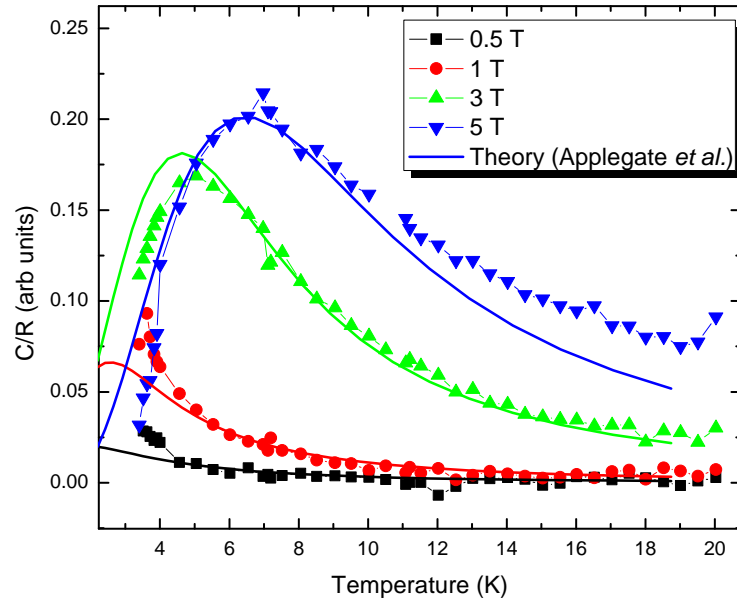


Figure 4.11: Comparison of theoretical data (represented by solid lines) from [Applegate 2012] with our measurements with the $H = 0$ T data numerically subtracted.

temperature (away from the sharp transition at $T \sim 265$ mK) thermodynamic properties, and draw the conclusion that the ground state of $\text{Yb}_2\text{Ti}_2\text{O}_7$ should show full ferrimagnetic order. Their calculations represent the field dependent part of our specific heat measurements qualitatively well. The authors admit their model fails (their calculated data becomes negative and unphysical) below the Schottky anomaly, however they still propose their model implies an ordered magnetic ground state. This brings the claim of the Schottky anomaly is a consequence of the crossover from the paramagnetic regime to a phase dominated by quantum mechanical fluctuations, or even a quantum spin ice, into question. In this study, there are some uncertainties related to the T^3 phonon contribution subtraction, as well as the unknown linear contribution ($\gamma \neq 0$) to the specific heat. However this is not enough to account for the large differences shown in Fig. 4.10. In Chapter 5, we will follow up on

Applegate *et al.*'s [Applegate 2012] model and investigate the low temperature magnetism with ZF and TF μ SR and determine if there is any type of magnetic long range order.

μ SR Results

Contents

5.1 Zero Field μSR	68
5.2 Transverse Field μSR	71
5.3 Comparison to $\text{Tb}_2\text{Sn}_2\text{O}_7$	78

The following chapter discusses the ZF and TF μ SR measurements on both single crystal and polycrystalline $\text{Yb}_2\text{Ti}_2\text{O}_7$. Much of these results form the basis of a paper titled "Unconventional Magnetic Ground State in $\text{Yb}_2\text{Ti}_2\text{O}_7$ " submitted to Physical Review Letters [R.M. D'Ortenzio 2013]. Our results give conclusive proof that the ground state of $\text{Yb}_2\text{Ti}_2\text{O}_7$ is dynamic with no long range magnetic order, contrasting the ordered ground state observed in several other studies [Y. Yasui 2003, L.-J. Chang 2012]. This dynamic ground state makes $\text{Yb}_2\text{Ti}_2\text{O}_7$ a possible experimental realization of a quantum spin liquid. In addition, the temperature independence of ZF asymmetry spectra as the thermodynamic phase transitions viewed in the specific heat are transversed (Fig. 4.4) suggests these phase transitions are not described by magnetic order parameters, rather some unknown "hidden order" mechanism.

5.1 Zero Field μ SR

A summary of ZF μ SR measurements performed on polycrystalline and single crystal $\text{Yb}_2\text{Ti}_2\text{O}_7$ is shown in Fig. 5.1. Each sample was left to sit at base temperature ($T \sim 16$ mK) for several hours before experiments were conducted, in order to ensure thermal equilibrium with the Ag sample holder has been reached. This was done to take into account the long thermal relaxation time as viewed by neutron scattering [Y. Yasui 2003] at low temperatures. Muons entered the samples 100% spin polarized, and the time evolution of the average muon depolarization was measured. We found that the asymmetry spectra were unaffected by an applied longitudinal field (LF) up to at least $H = 20$ G. Calibration using the asymmetry spectra taken at the transverse positron counters verified that the max applied LF is $H < 5$ G, therefore no precise zeroing procedure was necessary. This small longitudinal field serves to decouple any relaxation contribution to the asymmetry due to static nuclear moments in the Ag sample holder or cryostat equipment [Dunsiger 2011].

It is clear from the spectra in Fig. 5.1 (b) and (c) that neither sample has an oscillating or non-relaxing component down to $T \sim 16$ mK. The muon polarization function completely depolarize to zero asymmetry such that they can be fit with a simple exponential decay with no constant offset. This indicates that the fields are completely dynamic, with no static component. There is no evidence of any magnetic long range order in either samples measured down to $T = 16$ mK.

This result is in contrast to the evidence presented through neutron scattering measurements by Chang *et al.* [L.-J. Chang 2012] and Yasui *et al.* [Y. Yasui 2003], who observe a full first order transition to a ferromag-

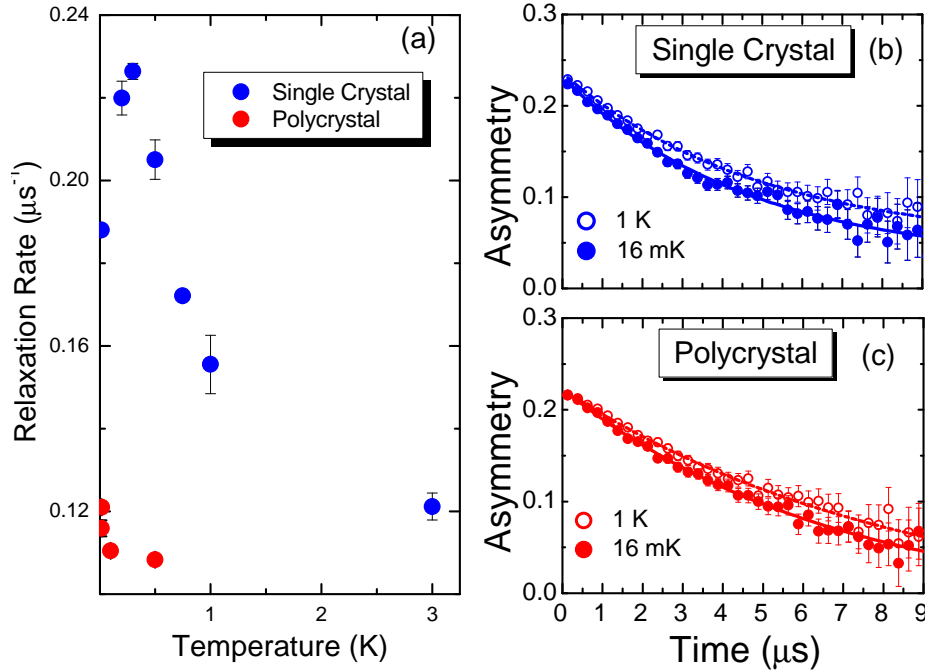


Figure 5.1: Left image: the temperature dependence of the relaxation of the muon polarization in ZF. Both polycrystalline and single crystal $\text{Yb}_2\text{Ti}_2\text{O}_7$ show little change. The right images show the asymmetry spectra at 16 mK and 1 K, below and above the magnetic transition at ~ 265 mK for both polycrystalline and single crystal, to emphasize the similarities. Taken from [R.M. D'Ortenzio 2013].

netic long range ordered ground state. Chang *et al* suggest that other experiments do not see long range magnetic order because they are using non-stoichiometric samples of $\text{Yb}_2\text{Ti}_2\text{O}_7$, which also results in variations in specific heat data. However, our polycrystalline sample exhibits a very sharp first order like transition at high temperature ($T \sim 265$ mK), and no sign of ferromagnetism down to 16 mK. Our measurement is consistent with several other experimental studies of the low temperature magnetism of $\text{Yb}_2\text{Ti}_2\text{O}_7$ [K.A. Ross 2009, Gardner 2004]. In addition, these results do not support the ordered ferrimagnetic ground state proposed by Ap-

plegate *et al.* [Applegate 2012] used to calculate the thermodynamic properties of $\text{Yb}_2\text{Ti}_2\text{O}_7$. Surprisingly, our ZF μSR results are very different from those presented by Hodges *et al.* [J.A. Hodges 2002, J.A. Hodges 2004]. We do not see the development of a second shorter timescale below the thermodynamic transition. This indicates that the fluctuation rate of Yb^{3+} ions does not significantly drop in a discontinuous manner for either of our measured samples. It is difficult to reconcile these differences, however it is possible that the differences viewed in specific heat between our sample and those used in [J.A. Hodges 2002, J.A. Hodges 2004] (shown as the green data points in Fig. 4.4) are connected with the low temperature magnetic state of $\text{Yb}_2\text{Ti}_2\text{O}_7$. [K.A. Ross 2012]. In addition, there are other sample dependencies beyond those described by the stuffed pyrochlore model [K.A. Ross 2012], such as oxygen deficiencies that cause color gradients along the length of grown single crystals (Fig. 1.7).

Fig 5.1 shows asymmetry spectra both above and below the first order transition at $T = 16$ mK and $T = 1$ K, and both are well described by a simple exponential decay, with similar decay rates. The striking lack of difference between the two asymmetry spectra suggests this thermodynamic transition is not magnetic at all, as the ZF measurements would be sensitive to any changes in the magnetic state. The possibility that the muon's initial polarization is parallel to the internal magnetic field of the sample, resulting in no oscillations in the asymmetry spectra can be eliminated due to the cubic nature of the crystal structure. If there was a magnetic anisotropy such that the internal magnetic field at the muon location pointed along a [111] crystallographic direction, the symmetry of the crystal lattice with four equivalent [111] directions would break the internal magnetic fields into a domain structure, giving

a muon precession signal in all but one domain. In the polycrystal sample, the local magnetic fields will be averaged over all crystallographic directions, also eliminating the possibility that the entire magnetic field is parallel to the initial muon polarization.

Another possible explanation is that the samples are not in thermal equilibrium with the Ag cryostat finger, and the samples are still above the temperature of the thermodynamic transition. Our TF μ SR measurements preclude this possibility, as we observe a change in the muon Knight shift at the thermodynamic transition temperature, showing that muons are sensitive to the magnetic environment in $\text{Yb}_2\text{Ti}_2\text{O}_7$. This is discussed further in the subsequent section on TF μ SR.

5.2 Transverse Field μ SR

TF μ SR measurements were performed with an applied field of $H = 50$ mT applied perpendicular to the initial muon polarization, and parallel to the muon beam direction. For the single crystal sample, the field was applied parallel to a [111] crystallographic direction. The geometry of this measurement is shown in Fig. 2.18. The measurements were not taken in any way to take into account the magnetic history. We chose a small applied magnetic field of $H = 50$ mT to not enter the magnetic induced LRO state shown in Fig. 1.6 which occurs above $H \sim 0.5$ T at 30 mK when the field is applied parallel to [110] [K.A. Ross 2009]. We completed this experiment under the assumption that this critical field is similar for the [111] direction, justified by the lack of magnetic anisotropy viewed in our dc magnetic susceptibility measurements.

The results of the TF measurements are presented on the left side of

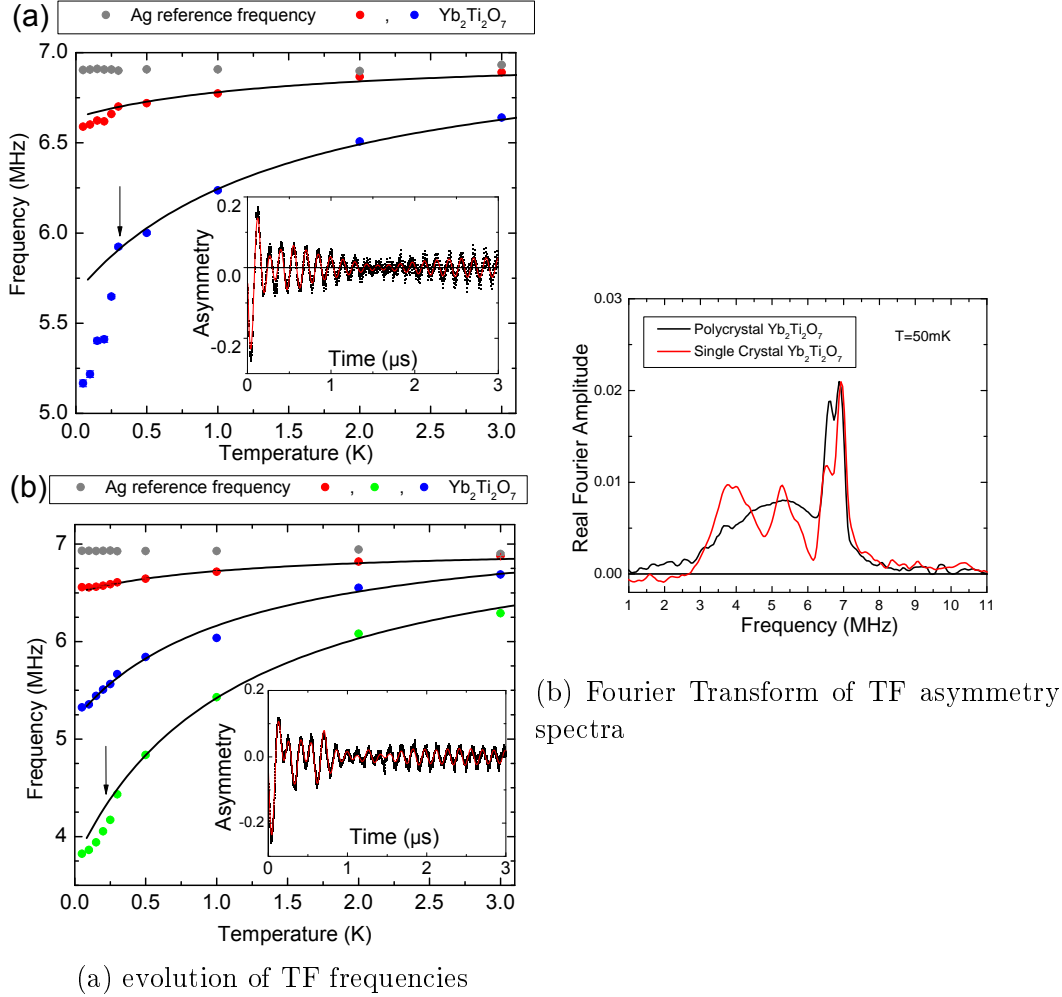


Figure 5.2: The image on the left: TF=50 mT μSR measurements of (a) polycrystalline and (b) single crystal $\text{Yb}_2\text{Ti}_2\text{O}_7$. The single crystal is aligned such that a $\langle 111 \rangle$ direction is parallel to the muon momentum (beam direction), but perpendicular to the incident muon's polarization. The temperature independent signal represented by grey points comes from the Ag sample holder. The black lines added are Curie-Weiss fits with a common $\Theta_{\text{CW}}^\mu = -1.3 \pm 0.5$ K. The inset of both (a) and (b) show the asymmetry time spectra in black, with the fit functions in red. The image on the right: The Fourier transform of the TF asymmetry spectra at $T = 50$ mK for both samples. There are three distinct lines (frequencies) for the polycrystal sample, and four distinct lines for the single crystal sample, justifying the fit presented in Eq. 5.1. Taken from [R.M. D'Ortenzio 2013].

Fig. 5.2 for both single crystal and polycrystalline samples. The insets of the left image in Fig. 5.2 (a) and (b) show an example of an asymmetry spectra at $T = 50$ mK in black, with the corresponding fit superimposed in red, showing good agreement. The asymmetry spectra were fit with Eq. 5.1:

$$A(t) = \sum_{i=1}^n A_i e^{-\sigma_i^2 t^2} \cos(\omega_i t + \varphi) \quad (5.1)$$

The entire data set was fit globally for each sample, with the total asymmetry and amplitude of each precession frequency’s contribution held constant for all temperatures. In our fitting, the asymmetry spectra was best described by a sum of sinusoidal precession with a Gaussian relaxation envelope with timescale σ_i which was allowed to vary with temperature. In addition, the overall phase (approximately $90 \pm 5^\circ$ for all runs) could vary in between temperatures.

To determine the number of frequencies in each sample, a Fourier transform of each asymmetry spectra at $T = 50$ mK was performed, shown in the right hand side of Fig. 5.2, where the precession frequencies were most resolved. From this, the single crystal sample shows four distinct muon precession frequencies $n = 4$, and the polycrystalline sample shows three $n = 3$ that could be resolved. It is possible there be more precession frequencies that could not be resolved at $H = 50$ mT, however the number of frequencies chosen in Eq. 5.1 gave very good agreement with raw asymmetry spectra. Applying a larger magnetic field, and collecting more muons to improve statistics could show any unresolved precession frequencies, but risks inducing a LRO state. There is a sharp peak in the real Fourier power at approximately 7 MHz for both samples. This peak’s amplitude and position is largely independent of

temperature, and therefore attributed to muons landing in the Ag cryostat sample holder. This frequency signal provides a useful reference to measure the muon Knight shifts of the actual $\text{Yb}_2\text{Ti}_2\text{O}_7$ signals. On the left hand side of Fig. 5.2, this temperature independent muon precession is shown by the grey points.

The remaining muon precession frequencies are interpreted as unique magnetic environments for the implanted muons. The single crystal sample has an additional precession frequency when compared to the polycrystal sample. Our proposed explanation is that when all crystallographic directions are averaged, two of the the unique magnetic environments become equivalent. This is consistent with the data in Fig. 5.2, as an average of the two lines shown in the blue and green data for the single crystal (b) will approximately reproduce the positions of the line shown by the blue data in the polycrystalline data (a). The positively charged muons have a high probability to sit near the O^{2-} ions, due to electrostatic interaction. There are two unique oxygen sites in $\text{Yb}_2\text{Ti}_2\text{O}_7$, as shown in Fig. 1.3. There are six oxygens staggered up and down surrounding the central Yb^{3+} ion connecting the two tetrahedral, and an additional oxygen site sitting in the middle of each tetrahedra. One possibility is when a magnetic field is applied parallel to the $[111]$ direction, the six surrounding oxygens are split into two unique magnetic environments for the muons. As the oxygens are staggered three above and three below a plane through the central Yb^{3+} ion normal to the global $[111]$ direction, this explanation seems plausible. This leaves the remaining muon site to sit near the oxygen in the center of the corner sharing tetrahedra. When the crystal is in powder form, the direction of the applied field does not matter as all crystallographic directions are equally represented. The signals viewed

in the Fourier transform (Fig. 5.2) for the polycrystalline sample span the full range of possible signals if the magnetic field was applied along a specific crystallographic direction.

It is a common trend for frustrated magnetic pyrochlores to exhibit largely temperature independent ZF/LF muon polarization functions [Uemura 1994, P.A. McClarty 2011, Dunsiger 2011, Quemerais 2012]. A recent proposal explaining the temperature independence of the relaxation at low temperature in the closely related rare earth pyrochlore classical spin ice $\text{Dy}_2\text{Ti}_2\text{O}_7$ [Quemerais 2012], originating from the quantum diffusion of muons is eliminated by our TF μSR results shown in Fig. 5.2. This mechanism involves the quantum mechanical tunneling of muons to different magnetic environments in the low temperature spin ice state. This results in a temperature independent relaxation, and an averaging of the local magnetic field seen by implanted muons such that they would be only one precession frequency. This model is based upon the assumption that electronic spins are static on the timescale of the muons, which does not apply to $\text{Yb}_2\text{Ti}_2\text{O}_7$ as our ZF μSR measurements show a completely dynamic low temperature state. The possibility of quantum diffusion of muons [Quemerais 2012] is unlikely here, as the lines as viewed in the Fourier transform (Fig. 5.2 right side) of the asymmetry spectra would be broadened by muons tunneling to different locations such that they could not be resolved. The only possibility is muons selectively tunneling to equivalent magnetic environments, which would leave the muon precession frequencies intact.

The arrows in Fig. 5.2 represent the onset temperature of the thermodynamic transition measured in our specific heat measurements (Fig. 4.4). There is a distinct change in the temperature dependence of the frequencies

corresponding approximately to these temperatures. This change is more pronounced in the polycrystalline sample, which also has the sharper transition in the specific heat. As TF measurements characterize the magnetic spin susceptibility, the frequency shifts (described in Eq. 5.2) above the thermodynamic transition temperature in the paramagnetic regime (above $T = 300$ mK for both samples) were fit to a Curie-Weiss function as it represents the data well and provides a physical interpretation. Superimposed on the muon frequency temperature dependence are Curie-Weiss like fits, described by Eq. 4.1 in black. These fits were taken with respect to the reference Ag sample holder frequency, where Θ_{CW}^μ is the empirical Curie-Weiss temperature:

$$\left| \frac{f_{Ag} - f_y}{f_{Ag}} \right| \propto (T - \Theta_{CW}^\mu)^{-1} \quad (5.2)$$

Where f_{Ag} is the muon precession frequency in the sample holder, assumed to be temperature independent, and f_y is the muon precession frequencies in $\text{Yb}_2\text{Ti}_2\text{O}_7$. The fits were done such that each muon Knight shift had a common Θ_{CW}^μ temperature (allowed to vary for the two samples) where we obtained common value of $\Theta_{CW}^\mu = -1.3 \pm 0.5$ independently. This is considerably below the value calculated from dc magnetic susceptibility measured in a SQUID above 2K, $\Theta_{CW} = 0.4 \pm 0.1$ K. We have established a temperature dependence of the Curie-Weiss temperature in Chapter. 4. The negative Curie-Weiss temperature suggests that there may be some competing antiferromagnetic interactions is interesting to note. We do not expect that the magnetic susceptibility would have the same behavior below $\Theta_{CW} = 0.4 \pm 0.1$ K measured in a SQUID. These fits show there is a distinct deviation from

Curie-Weiss behavior at the temperature of the onset of the transition seen in the specific heat. Plotted in Fig. 5.3 are the residuals of the fits, highlighting these deviations. The transition is larger and more first order-like for the polycrystalline sample, consistent with the more prominent transition seen in $C(T)$ (Fig. 4.4).

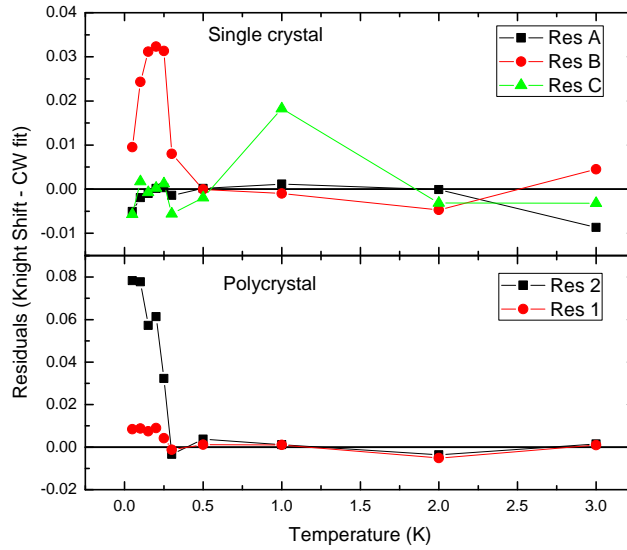


Figure 5.3: Temperature dependence of the difference between parameterized Curie-Weiss fits on the muon Knight shifts (shown in Fig. 5.2) for both single crystal and polycrystalline $\text{Yb}_2\text{Ti}_2\text{O}_7$ samples. There is a distinct deviation from Curie-Weiss behavior, more pronounced in the polycrystalline sample, at the approximate temperature of the phase transitions that are observed in the specific heat ($T_C \approx 265$ mK for the polycrystal, and $T_C \approx 185$ mK for the single crystal). Error bars are included, but smaller than the data points. Error is on the order of 1%.

Our TF μSR measurements are important for several reasons. These results eliminate the possibility that the ZF μSR measurements were taken out of thermal equilibrium, as the TF measurements which were largely taken in quick succession (less than an hour between runs) are clearly sensitive to the thermodynamic transition viewed by the specific heat. This supports the conclusion of a dynamic magnetic ground state as observed from our ZF μSR

results. In addition, these results show the thermodynamic transition in the specific heat corresponds to a change in the Yb^{3+} ion spin susceptibility or hyperfine coupling of the electronic moments to the muon.

The temperature dependence of the muon relaxation TF (σ in Eq. 5.1) is presented in the Appendix A of this report.

5.3 Comparison to $\text{Tb}_2\text{Sn}_2\text{O}_7$

It is interesting to compare our μSR results to those presented in [Dalmas de Réotier 2006] on $\text{Tb}_2\text{Sn}_2\text{O}_7$, which is another geometrically frustrated material on a pyrochlore lattice. Powder neutron diffraction measurements of $\text{Tb}_2\text{Sn}_2\text{O}_7$ show a magnetic ordered state below $T=0.87$ K, also associated with a peak in the temperature dependence of the specific heat. Magnetic susceptibility measurements of $\text{Tb}_2\text{Sn}_2\text{O}_7$ reveal strong antiferromagnetic interactions $\Theta_{CW} = -12\text{K}$ rather than the weak ferromagnetic interactions in $\text{Yb}_2\text{Ti}_2\text{O}_7$. The transition at lower than expected temperature $T=0.87$ K with respect to the strength of the magnetic interactions is a good indication that $\text{Tb}_2\text{Sn}_2\text{O}_7$ exhibits magnetic frustration. The ordered magnetism as viewed by neutron scattering would lead one to expect to see an oscillatory component in the ZF μSR measurements below 0.87 K, but no such signal is observed. They report similar ZF μSR spectra to those presented in this study, fit with a stretched exponential function where the asymmetry spectra $A(t)$ is described by $A(T) \propto e^{-(\lambda t)^\alpha}$ where α is the stretching parameter. At low temperatures, the reported relaxation rate becomes almost temperature independent. However, the nature of the ground state of $\text{Tb}_2\text{Sn}_2\text{O}_7$ and whether it truly displays long range magnetic order is not fully

established [Dalmas de Réotier 2006, Bert 2006, Giblin 2008]. It seems that $\text{Tb}_2\text{Sn}_2\text{O}_7$ suffers from similar sample dependence issues that could affect the low temperature magnetism issues as many other frustrated pyrochlores. It seems it is a common problem for frustrated magnetic pyrochlores to exhibit sample dependence that affects the magnetic ground state.

Conclusions

Contents

6.1 Prospective Future Work	85
--	-----------

In this study, I performed detailed measurements on the low temperature behavior of $\text{Yb}_2\text{Ti}_2\text{O}_7$ using specific heat, ZF and TF μSR measurements. In order to investigate the important issue of sample dependence and its effects on the magnetic ground state of $\text{Yb}_2\text{Ti}_2\text{O}_7$, measurements were conducted on both a polycrystalline sample with assumed perfect stoichiometry, and a single crystal grown via the optical floating zone method that has a high degree of off stoichiometry stuffing as described in [K.A. Ross 2012].

The initial component of this study involves the growth and characterization of $\text{Yb}_2\text{Ti}_2\text{O}_7$. Polycrystalline rods were prepared and grown using the optical floating zone method, and the single grain component of the grown crystals were aligned by Laue X-Ray diffraction and cut along appropriate crystallographic direction with a diamond saw. We verified the phase and determined the lattice constant a to be $a = 10.029 \pm 0.001 \text{ \AA}$ for all samples by powder X-Ray diffraction.

To characterize the bulk magnetism of both single and polycrystalline samples, I measured the dc magnetic susceptibility in a Superconducting Quantum Interference Device (SQUID). The Curie-Weiss temperature was seen to be

temperature dependent, but generally confirmed to agree with previous studies [H.W.J. Blote 1969] $\Theta_{cw} = 0.4 \pm 0.1$ K when fit in the temperature range $2 \text{ K} \leq T \leq 10 \text{ K}$, giving overall weak ferromagnetic interactions of approximate strength $T_C \times k_B \sim 34 \mu\text{eV}$. Magnetic susceptibility was measured along the [100] and [110] crystallographic directions, and no significant magnetic anisotropy was observed up to an applied field of $H = 5 \text{ T}$.

A phase transition was observed for both samples through specific heat measurements below 2 K done at the University of Waterloo by D. Pomaranski and J. Kycia. For the polycrystalline sample, the transition is sharp and first order like, peaking at approximately $T \sim 265 \text{ mK}$. This lead the experimenters to approximate the polycrystalline sample as stoichiometric balanced, such that $x \approx 0$ in the stuffed pyrochlore model described by Eq. 1.3. The single crystal sample has a much broader transition approximately 25 times weaker, peaking at $T \sim 185 \text{ mK}$. This sample is expected to have a high degree of stuffing ($x \neq 0$) [K.A. Ross 2012]. These two samples illustrate extreme cases of sample dependence in $\text{Yb}_2\text{Ti}_2\text{O}_7$ as reflected in the specific heat.

Specific heat measurements above 2K in an applied field up to $H = 9 \text{ T}$ performed at McMaster University in an Oxford ExaLab reveal the evolution of the Schottky anomaly, which occurs between $2 \text{ K} < T < 10 \text{ K}$. As the applied magnetic field increases, the peak temperature and FWHM increase, and the amplitude with respect to the T^3 phonon contribution decreases. To compare to the theoretical data presented by Applegate *et al.* [Applegate 2012], experimental data was plotted as $C(T)/T$ vs T^2 to remove the phonon contribution. There is a linear contribution to the specific heat, reflected through non-zero γ values for $C(T) = \gamma T + \beta T^3$ fits. This contribution cannot be a free electron fermi contribution, as $\text{Yb}_2\text{Ti}_2\text{O}_7$ is an insulator. There is good

agreement below ~ 10 K in all applied fields, however there is an unaccounted for component in the specific heat viewed by our experimental data after the phonon contribution is removed, beyond the uncertainties of the numerical subtraction process. The theoretical data represents the observed evolution of the the specific heat in the vicinity of the Schottky anomaly in an applied field well, but fails at lower and higher temperatures. This brings Applegate *et al.*'s model of a ferrimagnetic ground state where the Schottky anomaly is due to a crossover from paramagnetism to a quantum mechanical dominated regime into question.

To investigate the magnetic ground state of $\text{Yb}_2\text{Ti}_2\text{O}_7$ and investigate the link of sample dependence with the low temperature magnetism, TF and ZF μSR measurements were performed. The ZF asymmetry spectra for all samples could be described by a simple exponential decay to zero. This indicates that the magnetic moments of Yb^{3+} ions are completely dynamic, with no static frozen fields and no long range magnetic order down to 16 mK. Surprisingly, there is little temperature dependence of the relaxation timescale as the thermodynamic transition is crossed for both measured samples, suggesting there is no significant change in the magnetism. Therefore, the change in entropy that causes the phase transition viewed in the specific heat must be described by some other nonmagnetic unknown "hidden order" parameter. In addition, it is important to note how similar the ZF asymmetry spectra are for the samples measured. Despite the extreme variations in the transition viewed in the specific heat, the magnetic state we observed is almost the same. Therefore our ZF results suggest that although there is variation in the specific heat in $\text{Yb}_2\text{Ti}_2\text{O}_7$, the low temperature magnetism may not be affected.

Our TF μ SR measurements demonstrate that our measurements are indeed sensitive to the thermodynamic phase transition, as characterized by a distinct change in the local spin susceptibility. This change is seen as a deviation from $\propto (\Theta_{CW} - T)^{-1}$ Curie-Weiss behavior at temperatures corresponding approximately to the onset of the phase transition. There are three unique precession frequencies in the single crystal sample, and two distinct signals in the polycrystalline sample that can be resolved at an applied field of $H = 50$ mT.

Our μ SR do not reproduce the first order like drop in fluctuation rate observed by Hodges *et al.* [J.A. Hodges 2002, J.A. Hodges 2004], which could be due to sample variation in $\text{Yb}_2\text{Ti}_2\text{O}_7$. We observe no ordered magnetic ground state reported by some neutron scattering measurements [L.-J. Chang 2012, Y. Yasui 2003] and theoretically proposed in several studies, such as: [Applegate 2012, Hayre 2013].

Our ZF μ SR data gives evidence that the magnetic state shows little temperature dependence when the thermodynamic transition viewed in the specific heat is crossed. The change in entropy that causes this transition in the specific heat must be provided by some other order parameter, likely non-magnetic. As in the heavy fermion compound URu_2Si_2 , which undergoes a thermodynamic transition at ~ 17.5 K as viewed by the specific heat of which the order parameter is unknown [Mydosh 2011], we propose that $\text{Yb}_2\text{Ti}_2\text{O}_7$ undergoes a "hidden order" phase transition to a dynamic magnetic ground state. Despite the extreme variation of the specific heat between our two samples measured, their magnetic low temperature behavior is surprisingly similar. This also supports the hypothesis that this transition is not magnetic in nature.

6.1 Prospective Future Work

With regards to further μ SR measurements, to fully determine the nature of the magnetic ground state in $\text{Yb}_2\text{Ti}_2\text{O}_7$ and what types of magnetic environments exist within the crystal lattice more μ SR measurements need to be conducted. TF μ SR measurements with the magnetic field applied along different crystallographic directions would elucidate the muon's stopping locations and give deeper insight into the magnetic properties of $\text{Yb}_2\text{Ti}_2\text{O}_7$. Applying a field larger than the $H = 50$ mT used in this study, and collecting more muons to improve the asymmetry spectra's statistics could help resolve any hidden precession frequencies. It would also be an interesting experiment to apply a large TF > 0.5 T field to investigate the induced LRO state, as shown in Fig. 1.6. An experiment that would give more insight into the role of sample dependence on the magnetic state would be to investigate the transition to LRO with both stuffed and stoichiometric samples, and compare the magnetic properties. μ SR could provide an excellent tool that could be used to verify and provide detail to Fig. 1.6.

To solve the stuffing problem for crystals grown via the optical floating zone technique and to compensate for the presumably evaporating TiO_2 , it would be interesting to attempt a growth where the polycrystalline rod has been formed with extra TiO_2 . Some attempts at this have already been performed at McMaster University. In addition, the effects of using different pressures or different atmospheres (such as Ar) on the magnetic ground state and specific heat are relatively poorly understood.

Bibliography

- [A. de Visser 2009] A. Gasparini D.E. de Nijs D. Andreica C. Baines A. de Visser N.T. Huy and A. Amato. *Muon spin rotation and relaxation in the superconducting ferromagnet UCoGe*. Physical Review Letters, vol. 102, no. 167003, 2009. (Cited on pages [viii](#) and [24](#).)
- [A.P. Ramirez 2011] R.J. Cava R. Siddharthan A.P. Ramirez A. Hayashi and B.S. Shastry. *Searching for the Magnetic Interactions in the Rare Earth Pyrochlore Oxide Yb₂Ti₂O₇*. Letters to Nature, no. 2, pages 1–157, 2011. (Cited on pages [5](#), [6](#) and [10](#).)
- [Applegate 2012] R. Applegate, N. R. Hayre, R. R. P. Singh, T. Lin, A. G. R. Day and M. J. P. Gingras. *Vindication of Yb₂Ti₂O₇ as a Model Exchange Quantum Spin Ice*. Phys. Rev. Lett., vol. 109, page 097205, Aug 2012. (Cited on pages [ii](#), [xi](#), [14](#), [15](#), [61](#), [62](#), [64](#), [65](#), [66](#), [70](#), [82](#), [84](#) and [98](#).)
- [Bert 2006] F. Bert, P. Mendels, A. Olariu, N. Blanchard, G. Collin, A. Amato, C. Baines and A. D. Hillier. *Direct Evidence for a Dynamical Ground State in the Highly Frustrated Tb₂Sn₂O₇ Pyrochlore*. Phys. Rev. Lett., vol. 97, page 117203, Sep 2006. (Cited on page [79](#).)
- [C. Castelnovo 2008] S.L. Sondhi C. Castelnovo R. Moessner. *Magnetic monopoles in spin ice*. Nature Physics, vol. 451, no. 42-45, 2008. (Cited on page [5](#).)
-

- [C. Lacroix 2011] F. Mila C. Lacroix P. Mendels. *Introduction to Frustrated Magnetism. Materials, Experiments and Theory*. 2011. (Cited on page 3.)
- [Cao 2009] H. Cao, A. Gukasov, I. Mirebeau, P. Bonville, C. Decorse and G. Dhahlenne. *Ising versus XY Anisotropy in Frustrated $R_2Ti_2O_7$ Compounds as "Seen" by Polarized Neutrons*. Phys. Rev. Lett., vol. 103, page 056402, Jul 2009. (Cited on page 8.)
- [D. Pomaranski 2013] S. Meng K.A. Ross H.M.L. Noad H.A. Dabkowska B.D. Gaulin D. Pomaranski L.R. Yaraskavitch and J.B. Kycia. *Absence of Pauling's residual entropy in thermally equilibrate $Dy_2Ti_2O_7$* . Nature Physics, vol. 9, no. 353-356, 2013. (Cited on page 5.)
- [Dalmas de Réotier 2006] P. Dalmas de Réotier, A. Yaouanc, L. Keller, A. Cervellino, B. Roessli, C. Baines, A. Forget, C. Vaju, P. C. M. Gubbens, A. Amato and P. J. C. King. *Spin Dynamics and Magnetic Order in Magnetically Frustrated $Tb_2Sn_2O_7$* . Phys. Rev. Lett., vol. 96, page 127202, Mar 2006. (Cited on pages 78, 79 and 98.)
- [Dunsiger 2011] S. R. Dunsiger, A. A. Aczel, C. Arguello, H. Dabkowska, A. Dabkowski, M.-H. Du, T. Goko, B. Javanparast, T. Lin, F. L. Ning, H. M. L. Noad, D. J. Singh, T. J. Williams, Y. J. Uemura, M. J. P. Gingras and G. M. Luke. *Spin Ice: Magnetic Excitations without Monopole Signatures Using Muon Spin Rotation*. Phys. Rev. Lett., vol. 107, page 207207, Nov 2011. (Cited on pages 68 and 75.)
- [Gardner 2004] G. Rosov N. Erwin R.W. Petrovic C. Gardner J.S. Ehlers. *Spin-spin correlations in $Yb_2Ti_2O_7$: A polarized neutron scattering*

study. Phys. Rev. B, vol. 70, page 180404, Nov 2004. (Cited on pages i, 6 and 69.)

[Giblin 2008] S. R. Giblin, J. D. M. Champion, H. D. Zhou, C. R. Wiebe, J. S. Gardner, I. Terry, S. Calder, T. Fennell and S. T. Bramwell. *Static Magnetic Order in $Tb_2Sn_2O_7$ Revealed by Muon Spin Relaxation with Exterior Muon Implantation*. Phys. Rev. Lett., vol. 101, page 237201, Dec 2008. (Cited on page 79.)

[G.M. Luke 1997] K.M. Kojima M. Larkin J. Merrin B. Nachumi S. Sinawiy. J. Uemura M.J.P. Gingras M. Sato-S. Taniguchi M. Isobe Y. Ueda G.M. Luke Y. Fudamoto. *Observation of Spin Freezing in CaV_4O_9 and CaV_2O_5 by μSR* . Condensed Matter Arxiv, no. arXiv:cond-mat/9709123, 1997. (Cited on page 97.)

[Hayre 2013] N. R. Hayre, K. A. Ross, R. Applegate, T. Lin, R. R. P. Singh, B. D. Gaulin and M. J. P. Gingras. *Thermodynamic properties of $Yb_2Ti_2O_7$ pyrochlore as a function of temperature and magnetic field: Validation of a quantum spin ice exchange Hamiltonian*. Phys. Rev. B, vol. 87, page 184423, May 2013. (Cited on pages ii, 14 and 84.)

[Hodges 2001] JA Hodges, P Bonville, A Forget, M Rams, K Królas and G Dhalenne. *The crystal field and exchange interactions in $Yb_2Ti_2O_7$* . Journal of Physics: Condensed Matter, vol. 13, no. 41, page 9301, 2001. (Cited on page 8.)

[H.W.J. Blote 1969] W.J. Huiskamp H.W.J. Blote R.F. Weilinga. *Heat Capacity Measurements on Rare Earth Double Oxides $R_2M_2O_7$* . Physica, no. 43, pages 549–568, 1969. (Cited on pages vii, 8, 10, 15, 55 and 82.)

[J.A. Hodges 2002] A. Forget A. Yaouanc P. Dalmas de Réotier G. André-M. Rams K. Królas C. Ritter-P.C.M. Grubbens C.T. Kaiser P.J.C. King J.A. Hodges P. Bonville and C. Baines. *First-Order Transition in the Spin Dynamics of Geometrically Frustrated $Yb_2Ti_2O_7$* . Physical Review Letters, vol. 88, no. 077204, 2002. (Cited on pages i, 8, 70 and 84.)

[J.A. Hodges 2004] E. Bertin J.Ph. Bouchaud P. Dalmas de Réotier L.-P. Regnault H.M. Ronnow J.-P. Sanchez-S. Sosin J.A. Hodges P. Bonville and A. Yaouanc. *Transitions and Spin Dynamics at Very Low Temperature in the Pyrochlores $Yb_2Ti_2O_7$ and $Gd_2Sn_2O_7$* . Hyperfine Interactions, no. 156/157, pages 103–111, 2004. (Cited on pages i, 8, 70 and 84.)

[J.E. Sonier 2001] S.J. Blundell K.H. Chow S.R. Dunsiger D.G. Fleming R.H. Heffner S.R. Kreitzman R.F. Kieff-M.I. Larkin-G.M. Luke W.A. MacFarlane D.E. MacLaughlin P. Percival F.L. Pratt S.L. Stubbs J.E. Sonier J.H. Brewer and Y.J. Uemura. *Muon Spin Rotation/Relaxation/Resonance (μ SR)*. 2001. (Cited on pages viii, ix, 19, 21, 22 and 31.)

[J.S. Gardner 2004] N. Rosov R.W. Erwin J.S. Gardner G. Ehlers and C. Petrovic. *Spin-spin correlations in $Yb_2Ti_2O_7$: A polarized neutron scattering study*. Physical Review B, vol. 70, no. 180404, 2004. (Cited on page 12.)

[J.S. Gardner 2010] M.J.P. Gingras J.S. Gardner and J.E. Greedan. *Magnetic pyrochlore oxides*. Reviews of Modern Physics, vol. 82, no. 53-107, 2010. (Cited on pages 4, 7 and 52.)

- [K.A. Ross 2009] C.P. Adams J.S. Gardner H.A. Dabkowska Y. Qiu J.R.D. Copley K.A. Ross J.P.C. Ruff and B.D. Gaulin. *Two-Dimensional Kagome Correlations and Field Induced Order in the Ferromagnetic XY Pyrochlore $Yb_2Ti_2O_7$* . Physical Review Letters, vol. 103, no. 227202, 2009. (Cited on pages vii, 7, 13, 53, 69 and 71.)
- [K.A. Ross 2011] B. Gaulin L. Balents K.A. Ross L. Savery. *Quantum Excitations in Quantum Spin Ice*. Physical Review X, vol. 1, no. 021002, 2011. (Cited on pages ii, 13, 14 and 15.)
- [K.A. Ross 2012] H.A. Dabkowska J.A. Quilliam L.R. Yaraskavitch J.B. Kycia K.A. Ross Th. Proffen and B.D. Gaulin. *Lightly stuffed pyrochlore structure of single-crystalline $Yb_2Ti_2O_7$ grown by the optical floating zone technique*. Physical Review B, vol. 86, no. 174424, 2012. (Cited on pages 15, 16, 58, 70, 81 and 82.)
- [Kittel 2005] C. Kittel. Introduction to solid state physics. John Wiley & Sons, Inc, 2005. (Cited on pages vii, 3, 41, 43, 44, 46, 48 and 55.)
- [Kubo 1967] R Kubo, T Toyabe and R Blinc. *Magnetic resonance and relaxation*. North-Holland, Amsterdam, 1967) p, vol. 810, 1967. (Cited on page 28.)
- [L.-J. Chang 2012] Y. Su Y.-J. Kao K.-D. Tsuei Y. Yasui K. Kakurai L.-J. Chang S. Onoda and M.R. Lees. *Higgs transition from a magnetic Coulomb liquid to a ferromagnet in $Yb_2Ti_2O_7$* . Nature Communications, vol. 3, no. 992, 2012. (Cited on pages i, x, 12, 13, 57, 58, 67, 68 and 84.)

- [Luke 1988] G.M. Luke. *Quantum Diffusion and Spin Dynamics of Muons in Copper*. Ph.D Thesis, 1988. (Cited on page 26.)
- [Luke 2013] G. Luke. Physics 734: Experimental methods in condensed matter μ sr. McMaster University, 2013. (Cited on pages ix and 25.)
- [Maestro 2004] A.G. Del Maestro and M.J.P. Gingras. *Quantum spin fluctuations in the dipolar Heisenberg-like rare earth pyrochlores*. J. Physics: Condensed Matter, vol. 16, no. 3339, 2004. (Cited on page 9.)
- [M.B. Johnson 2009] A. Bourque H.A. Dabkowska-B.D. Gaulin M.A. White M.B. Johnson D.D. James. *Thermal Properties of the pyrochlore, $Y_2Ti_2O_7$* . J. of Solid State Chemistry, vol. 182, pages 725–729, 2009. (Cited on page 61.)
- [Melko 2001] Roger G. Melko, Byron C. den Hertog and Michel J. P. Gingras. *Long-Range Order at Low Temperatures in Dipolar Spin Ice*. Phys. Rev. Lett., vol. 87, page 067203, Jul 2001. (Cited on page 5.)
- [Mydosh 2011] J. A. Mydosh and P. M. Oppeneer. *Colloquium : Hidden order, superconductivity, and magnetism: The unsolved case of URu₂Si₂*. Rev. Mod. Phys., vol. 83, pages 1301–1322, Nov 2011. (Cited on page 84.)
- [P. Bonville 2004] E. Bertin J.-Ph. Bouchaud P. Dalmas de Réotier L.-P. Regnault H. M. Ronnow J.-P. Sanchez S. Sosin P. Bonville J.A. Hodges and A. Yaouanc. *Transitions and Spin Dynamics at Very Low Temperature in the Phrochlores $Yb_2Ti_2O_7$ and $Gd_2Sn_2O_7$* . Hyperfine Interactions, no. 156/157, pages 103–111, 2004. (Cited on pages vii, 10 and 12.)

- [P. Dalmas de Réotier 2006] C. Martin A. Yaouanc P.C.M. Gubbens S. Sakarya-P. Bonville A. Amato C. Baines P. Dalmas de Réotier V. Glazkov and P.J.C. King. *Studies of $R_2Ti_2O_7$ ($R = Gd$ and Yb); new results*. Physica B, vol. 374-375, no. 145-147, 2006. (Cited on page 58.)
- [P.A. McClarty 2011] A.G. Del Maestro P.A. McClarty N.J. Cosman and M.J.P. Gingras. *Calculation of the expected zero-field muon relaxation rate in the geometrically frustrated rare earth pyrochlore $Gd_2Sn_2O_7$ antiferromagnet*. J. of Physics: Condensed Matter, vol. 23, no. 164216, 2011. (Cited on page 75.)
- [Quemerais 2012] P. Quemerais, P. McClarty and R. Moessner. *Possible Quantum Diffusion of Polaronic Muons in $Dy_2Ti_2O_7$ Spin Ice*. Phys. Rev. Lett., vol. 109, page 127601, Sep 2012. (Cited on page 75.)
- [Queyroux 1965] F. Queyroux. *Existence of a new compound Yb_6TiO_{11} and the phase diagram for $Yb_2O_3-TiO_2$* . Bull. Soc. Franc. Miner. et Cristallogr., vol. 88, no. 519, 1965. (Cited on pages ix, 37 and 51.)
- [Quilliam 2007] J. A. Quilliam, C. G. A. Mugford, A. Gomez, S. W. Kycia and J. B. Kycia. *Specific Heat of the Dilute Ising Magnet $LiHo_xY_{1-x}F_4$* . Phys. Rev. Lett., vol. 98, page 037203, Jan 2007. (Cited on page 43.)
- [Riseman 1993] T.M. Riseman. Ph.d thesis. University of British Columbia, 1993. (Cited on page 30.)
- [R.M. D'Ortenzio 2013] S. R. Dunsiger B. D. Gaulin M. J. P. Gingras T. Goko J. B. Kycia-L. Liu T. Medina T. J. Munsie D. Pomaranski K. A. Ross Y. J. Uemura T. J. Williams G. M. Luke R.M. D'Ortenzio H.

A. Dabkowska. *Unconventional Magnetic Ground State in $\text{Yb}_2\text{Ti}_2\text{O}_7$* . arxiv.org arXiv:1303.3850, 2013. (Cited on pages i, x, xi, 57, 67, 69, 72 and 99.)

[Ross 2012] K.A. Ross. *Neutron Scattering Studies of the Quantum Spin Ice Material $\text{Yb}_2\text{Ti}_2\text{O}_7$* . Ph. D Thesis, McMaster University, 2012. (Cited on page 2.)

[Rovers 2001] Martin Tyssen Rovers. Spin liquid behavior in geometrically frustrated chromium oxides. McMaster University, 2001. (Cited on page 21.)

[S. Rosenkranz 2000] A. Hayashi R.J. Cava R. Siddharthan S. Rosenkranz A.P. Ramirez and B.S. Shastry. *Crystal-field interaction in the pyrochlore magnet $\text{Ho}_2\text{Ti}_2\text{O}_7$* . Journal of Applied Physics, vol. 87, no. 5914, 2000. (Cited on pages 5 and 8.)

[Siddharthan 1999] R. Siddharthan, B. S. Shastry, A. P. Ramirez, A. Hayashi, R. J. Cava and S. Rosenkranz. *Ising Pyrochlore Magnets: Low-Temperature Properties, "Ice Rules," and Beyond*. Phys. Rev. Lett., vol. 83, pages 1854–1857, Aug 1999. (Cited on pages 8 and 14.)

[S.L. Lee 1988] S.H. Kilcoyne R. Cywinski S.L. Lee. Muon science, muons in physics, chemistry and materials. 1988. (Cited on pages viii, 20, 21, 24, 28, 29 and 31.)

[T-H Han 2012] S. Chu D.G. Nocera J.A. Rodriguez-Rivera C. Broholm T-H Han J.S. Helton and Y.S. Lee. *Fractionalized excitations in the spin-liquid state of a kagome-lattice antiferromagnet*. Nature, vol. 492, no. 406-410, 2012. (Cited on page 3.)

- [Thompson 1999] J. Thompson. Zero-point entropy in "spin ice". University of Waterloo, 1999. (Cited on pages vii, 2, 3, 6, 7 and 8.)
- [Townsend 1968] M.G. Townsend and W.A. Crossley. *Magnetic susceptibility of rare-earth compounds with the pyrochlore structure*. Journal of Physics and Chemistry of Solids, no. 29(4), pages 593–598, 1968. (Cited on page 9.)
- [Uemura 1994] Y. J. Uemura, A. Keren, K. Kojima, L. P. Le, G. M. Luke, W. D. Wu, Y. Ajiro, T. Asano, Y. Kuriyama, M. Mekata, H. Kikuchi and K. Kakurai. *Spin Fluctuations in Frustrated Kagome Lattice System SrCr₈Ga₄O₁₉ Studied by Muon Spin Relaxation*. Phys. Rev. Lett., vol. 73, pages 3306–3309, Dec 1994. (Cited on page 75.)
- [Woods 2000] T. Woods. *Heat Capacity (Relaxation) Probe*. Oxford Instruments Technical Reference, 2000. (Cited on pages 41 and 42.)
- [Y. Yasui 2003] S. Iikubo M. Ito M. Sato N. Hamaguchi T. Matsushita N. Wada T. Takeuchi N. Aso Y. Yasui M. Soda and K. Kakurai. *Ferromagnetic transition of pyrochlore compound Yb₂Ti₂O₇*. J. Phys. Soc. Jpn, vol. 72, no. 11, 2003. (Cited on pages i, 11, 43, 67, 68 and 84.)
- [Yaouanc 2011] A. Yaouanc and P. Dalmas de Réotier. *Muon spin rotation, relaxation and resonance: Applications to condensed matter*. Oxford Science Publications, 2011. (Cited on pages 32 and 33.)

TF relaxation Temperature Dependence and LF measurements

A.1 TF = 500 G μ SR relaxation

Fig. A.1 shows the temperature dependence of σ from Eq. A.1 for single crystal and polycrystalline $\text{Yb}_2\text{Ti}_2\text{O}_7$. Each independent magnetic environment (corresponding to a unique muon precession frequency) was fit such to allow a unique relaxation timescale. The flat, mostly temperature independent relaxations are due to muons landing in the Ag sample holder.

$$A(t) = \sum_{i=1}^n A_i e^{-\sigma_i^2 t^2} \cos(\omega_i t + \varphi) \quad (\text{A.1})$$

The relaxation rate for muons landing in $\text{Yb}_2\text{Ti}_2\text{O}_7$ show temperature dependence, but no distinct change at the temperature corresponding to the transition observed in the specific heat.

A.2 LF μ SR measurements

In the paramagnetic phase of a material, such that the magnetic moments are fluctuating, the muon relaxation rate T_1 with an applied LF B_L is given by the following equation [G.M. Luke 1997]:

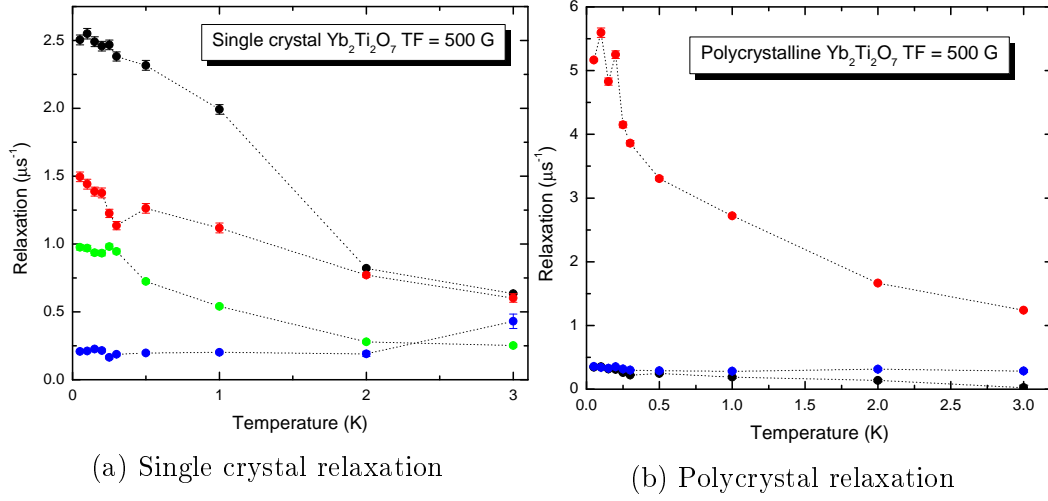


Figure A.1: The temperature dependence of the Gaussian envelope σ described in Eq. A.1 for single crystal (a) and polycrystalline samples (b).

$$\frac{1}{T_1} = \frac{\gamma_\mu^2 B_{inst}^2 \nu}{\nu^2 + \omega_L^2} \Rightarrow \nu \gg \gamma_\mu B_{inst} \quad (\text{A.2})$$

Where $B_L = \frac{\omega_L}{\gamma_\mu}$, ν is the fluctuation rate of the electronic magnetic moments, and B_{inst} is the magnitude of the instantaneous magnetic field experienced by the muon. When this model was applied to the field dependence of the relaxation rate in our LF measurements, the extracted B_{inst} was too small, on the order of ~ 1 Gauss, where a much bigger internal field on the order of 0.2 T (for other similar frustrated pyrochlores [Dalmas de Réotier 2006]) was expected. One possibility of why this fit does not give realistic results is that the system is not fully paramagnetic at $T = 1$ K, but in some regime dominated by quantum fluctuations as proposed by [Applegate 2012], displayed in the specific heat as a Schottky anomaly.

APPENDIX B

"Unconventional Magnetic
Ground State in $\text{Yb}_2\text{Ti}_2\text{O}_7$ " -
Submitted to Physical Review
Letters

The following paper is the result of work completed in this thesis. It has been submitted to Physical Review Letters [[R.M. D'Ortenzio 2013](#)].

Unconventional Magnetic Ground State in $\text{Yb}_2\text{Ti}_2\text{O}_7$

R. M. D’Ortenzio,^{1,*} H. A. Dabkowska,² S. R. Dunsiger,³ B. D. Gaulin,^{1,2,4}
M. J. P. Gingras,^{4,5,6} T. Goko,⁷ J. B. Kycia,⁵ L. Liu,⁷ T. Medina,¹ T. J. Munsie,¹
D. Pomaranski,⁵ K. A. Ross,^{8,9} Y. J. Uemura,⁷ T. J. Williams,¹ and G. M. Luke^{1,4}

¹*Department of Physics and Astronomy, McMaster University,
1280 Main St. W., Hamilton, ON, Canada, L8S 4M1*

²*Brockhouse Institute for Materials Research, McMaster University, Hamilton, Ontario L8S 4M1, Canada*

³*Physik-Department E21, Technische Universitat Munchen, D-85748 Garching, Germany*

⁴*Canadian Institute for Advanced Research, Toronto, Ontario, Canada, M5G 1Z8*

⁵*Department of Physics and Astronomy, University of Waterloo, Waterloo, ON N2L 3G1, Canada*

⁶*Perimeter Institute for Theoretical Physics, 31 Caroline North, Waterloo, Ontario, N2L-2Y5, Canada*

⁷*Department of Physics, Columbia University, New York, New York 10027, USA*

⁸*Institute for Quantum Matter and Department of Physics and Astronomy,
Johns Hopkins University, Baltimore, Maryland 21218, USA*

⁹*NIST Center for Neutron Research, National Institute of Standards and Technology, Gaithersburg, Maryland 20899, USA*

(Dated: March 18, 2013)

We report low temperature specific heat and muon spin relaxation/rotation (μSR) measurements on both polycrystalline and single crystal samples of the pyrochlore magnet $\text{Yb}_2\text{Ti}_2\text{O}_7$. This system is believed to possess a spin Hamiltonian supporting a Quantum Spin Ice (QSI) ground state and to display sample variation in its low temperature heat capacity. Our two samples exhibit extremes of this sample variation, yet our μSR measurements indicate a similar disordered low temperature state down to 16 mK in both. We report little temperature dependence to the spin relaxation and no evidence for ferromagnetic order, in contrast to recent reports by Chang *et al.* (Nat. Comm. **3**, 992 (2012)). Transverse field (TF) μSR measurements show changes in the temperature dependence of the muon Knight shift which coincide with heat capacity anomalies. We are therefore led to propose that $\text{Yb}_2\text{Ti}_2\text{O}_7$ enters a hidden order ground state below $T_c \sim 265$ mK where the nature of the ordered state is unknown but distinct from simple long range order.

Rare earth titanates of the form $\text{R}_2\text{Ti}_2\text{O}_7$ (R is a trivalent magnetic rare earth ion and the Ti is non-magnetic) provide an excellent vehicle for the study of geometric magnetic frustration. The R sites within the cubic pyrochlore structure, with space group $Fd\bar{3}m$, reside on a network of corner sharing tetrahedra, with a high propensity towards frustrated magnetic interactions leading to a wide range of exotic low temperature magnetic states [1]. For example, classical spin ice materials have been theoretically proposed to exhibit monopole-like quasiparticle excitations [2].

Spin ices such as $\text{Dy}_2\text{Ti}_2\text{O}_7$ have been extensively studied and are relatively well understood [1]. Recently, a new direction that has received much interest is that of “quantum spin ice”, where quantum fluctuations may elevate the classical spin liquid state of spin ice to a full blown quantum spin liquid. A possible candidate for a quantum spin ice is $\text{Yb}_2\text{Ti}_2\text{O}_7$, which does not exhibit the gradual spin freezing and residual low-temperature entropy of a classical spin ice [3]. However, the nature of its ground state is currently under much debate, with some recent experiments reporting a ferromagnetic low temperature state [4, 5], while others show a dynamic ground state with no long range order [6–9]. Despite this, the microscopic Hamiltonian for $\text{Yb}_2\text{Ti}_2\text{O}_7$ appears well described by a pseudospin-1/2 quantum spin ice model [3, 10, 11].

Previous zero field (ZF) μSR [6, 12] performed on polycrystalline $\text{Yb}_2\text{Ti}_2\text{O}_7$ showed no evidence of long range

magnetic order below the sharp specific heat transition at ~ 240 mK, rather they reported a Yb^{3+} spin fluctuation rate drop of approximately 4 orders of magnitude [13]. Mössbauer absorption spectra by the same group also indicated a first order magnetic transition, but could not give information about the microscopic nature of the ground state. Neutron scattering experiments show evidence for both an ordered ferromagnetic ground state [4, 5], and a dynamic magnetic ground state, with only short range (3D) spin correlations [7, 9]. Ross *et al.* [7, 9] report rods of magnetic scattering along the $\langle 111 \rangle$ directions, characteristic of short range two-dimensional (2D) correlations above 400 mK. Below 400 mK, the rods begin to coalesce and build up intensity near the $\mathbf{Q} = (1, 1, 1)$ Bragg peak, interpreted [10] as a cross-over to short range three-dimensional (3D) magnetic correlations, but clearly lacking long range order. Inelastic neutron scattering at 30 mK in these same studies shows only diffuse quasielastic scattering, and no evidence of sharp spin waves, again consistent with a dynamic disordered ground state. In contrast with Ref. [7], Chang’s polarized neutron scattering results [4] show suppression of the $\langle 111 \rangle$ scattering rods into full magnetic Bragg peaks in a first order manner below $T \sim 210$ mK.

Recent evidence suggests that, like other geometrically frustrated magnets such as $\text{Tb}_2\text{Ti}_2\text{O}_7$ [14], $\text{Yb}_2\text{Ti}_2\text{O}_7$ ’s ground state may be sensitive to small amounts of quenched disorder and non-stoichiometry at the $\sim 1\%$

level, with several reports of sample variation of the strong heat capacity anomaly near ~ 260 mK and below [7, 15, 16]. Variation of the heat capacity is observed between samples, both poly- and single-crystalline, and the largest heat capacity anomaly appearing at the highest temperature could be taken as a figure of merit for the sample quality. To date, this anomaly is seen to be sharpest in polycrystalline samples that were prepared by the method outlined in Ref. [15].

Neutron diffraction studies [15] have shown that a single crystal of $\text{Yb}_2\text{Ti}_2\text{O}_7$ grown using the optical floating zone technique is weakly “stuffed”, with stoichiometry $\text{Yb}_2(\text{Ti}_{2-x}\text{Yb}_x)\text{O}_{7-x/2}$ where $x \sim 0.046$, or 2.3% extra Yb^{3+} ions reside on the nonmagnetic Ti^{4+} sublattice. Meanwhile, polycrystalline samples prepared by the method in Ref. [15] are not stuffed ($x=0$). These defects are proposed [15] to contribute to the variation in magnetic ground state properties, and therefore the variation in the heat capacity observed in different samples.

In this letter, we study two samples of $\text{Yb}_2\text{Ti}_2\text{O}_7$ with very different low temperature heat capacities, shown in Fig. 1. One is a polycrystalline sample with a sharp, large heat capacity anomaly at relatively high $T_c \sim 265$ mK, while the other is a single crystal sample which displays a broad anomaly at $T_c \sim 185$ mK, with a peak amplitude 20 times smaller than that of the polycrystalline sample. For comparison, we also show the specific heat measurements reported by Chang *et al.* for the single crystal used in their neutron study [4], Dalmas de Réotier *et al.*'s polycrystalline sample used in a previous μSR study [6] and Ross *et al.*'s polycrystal used in Ref. [7]. Based on our specific heat data, we would expect our single crystal to have a relatively high degree of stuffing as the specific heat peak is pushed down to ~ 185 mK. Our polycrystalline sample shows a sharp temperature peak, from which we infer that it should be closer to balanced stoichiometry ($x \approx 0$). Remarkably, the μSR measurements we report show little difference between the two samples at low temperatures, and both the single crystal and our high quality polycrystalline sample are shown to remain disordered and dynamic to the lowest temperatures measured.

We prepared polycrystalline pellets of $\text{Yb}_2\text{Ti}_2\text{O}_7$ by mixing stoichiometric quantities of Yb_2O_3 and TiO_2 , isotropically pressing at 60 MPa then sintering at 1200 °C for 24 hours. We then grew single crystal $\text{Yb}_2\text{Ti}_2\text{O}_7$ from some of the polycrystalline material using the optical floating zone crystal growth method in 2 ATM of O_2 as described in [17]. SQUID measurements of the demagnetization above 2 K confirm Curie-Weiss behavior with overall weak ferromagnetic interactions, $\Theta_{\text{CW}}=0.4$ K, similar to values reported by previous studies [18, 19].

Weak longitudinal field (LF) μSR spectra are shown for $T=1$ K and 16 mK in Fig. 2 for both single crystal and polycrystalline samples. Calibration spectra using transverse counters show that the applied field is $H \leq 0.5$ mT.

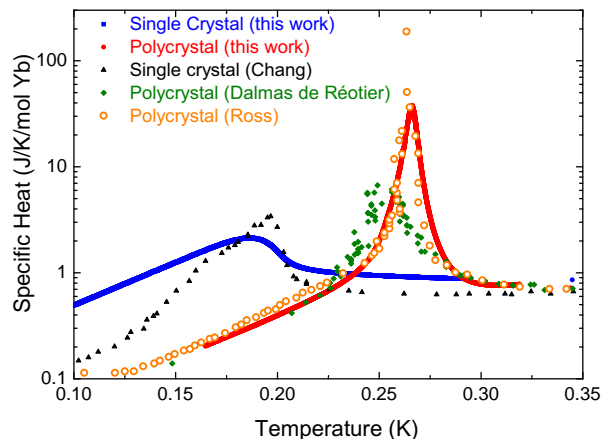


FIG. 1. Low T specific heat measurements of $\text{Yb}_2\text{Ti}_2\text{O}_7$ on a semi-logarithmic scale. The red and blue curves represent samples used for this work. Our polycrystalline sample exhibits a sharp transition at ~ 265 mK, and our single crystal shows a broad peak at ~ 185 mK. The black data is taken from Chang *et al.*'s [4] single crystal, and the green is the sample [13] used for Hodges *et al.*'s μSR measurements. The orange points are taken from Ross *et al* [7].

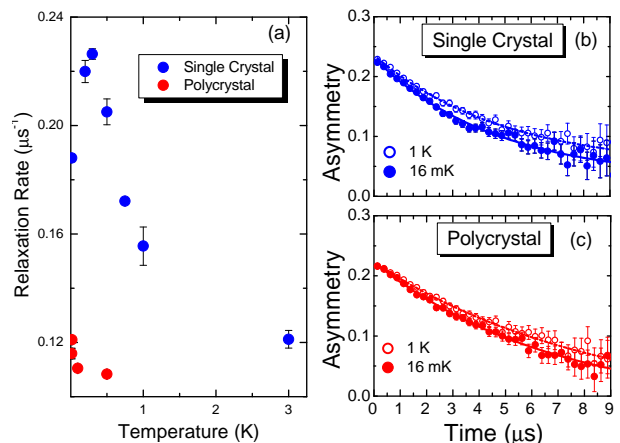


FIG. 2. A comparison of the weak LF (less than 0.5 mT) data for polycrystalline and single crystal $\text{Yb}_2\text{Ti}_2\text{O}_7$. Asymmetry spectra (shown in (b) and (c)) were fit with a single exponential decay with a globally fixed asymmetry for all T . Plot (a) shows the temperature dependence of the relaxation rate.

We confirmed that the longitudinal relaxation rate did not vary with the size of the weak applied field (up to at least ~ 2 mT) indicating that the small field does not affect the dynamics of the Yb^{3+} moments, although it does serve to decouple any static nuclear dipole relaxation from any stray muons landing in the cryostat tails or sample holder [20].

We find that the entire muon polarization signal re-

laxes with a simple exponential decay and a weak relaxation rate that is only slightly temperature dependent, as shown in Fig. 2. No oscillatory component or rapid relaxation that would be observed from an ordered state is present down to 16 mK for either sample. The random orientations of crystallites in the polycrystal and the cubic symmetry giving three equivalent $\langle 111 \rangle$ directions in the single crystal preclude the possibility of a static local field solely along the initial muon polarization direction (where muon precession would not be observed) [21]. In marked contrast to the results presented in [6], we observe no fast relaxing component for either of our samples at any temperature, including below the transitions observed in the specific heat. This behavior allows us to conclude that the Yb^{3+} spins are in the fast fluctuating (narrowing) regime, with an absence of long range magnetic order or even static internal magnetic fields such as would be present in a spin glass system at low temperature. The relaxation rate does increase somewhat with decreasing temperature, indicating a gradual slowing down of Yb^{3+} spin fluctuations; however they remain rapidly fluctuating down to 16 mK.

To further characterize the Yb^{3+} spin system, we performed transverse field (TF) μSR measurements to probe the local spin susceptibility, applying $H=50$ mT perpendicular to the initial muon spin polarization, which was rotated 90° relative to the LF measurements. For the single crystal $\text{Yb}_2\text{Ti}_2\text{O}_7$, the field was applied parallel to $[111]$. $H=50$ mT is small enough not to induce a magnetically ordered state along $[110]$, and likely also $[111]$ [7, 9]. Fig. 3 shows Fourier transforms of time spectra measured at $T=50$ mK, which exhibit a number of resolved lines for each sample. The positively charged muon's site in materials is determined by electrostatic interactions, with muons in $\text{Yb}_2\text{Ti}_2\text{O}_7$ most likely to reside near O^{2-} ions [20]. There are two crystallographically inequivalent O^{2-} ions in the pyrochlore structure, both of which could provide muon sites. The application of an external magnetic field along a specific (in this case a $[111]$) axis makes several crystallographically equivalent sites magnetically inequivalent and can therefore increase the multiplicity of muon precession frequencies. The splitting of each line from the frequency corresponding to the applied field reflects the local (anisotropic) susceptibility of that particular muon site. The polycrystalline sample exhibits fewer lines, though they are broader in frequency as a result of the powder averaging of the anisotropic shifts of different crystallographic sites. After examining the Fourier transforms we chose to fit the time spectra to Eq. 1 with $n=3$ (polycrystal) and $n=4$ (single crystal), fixing the amplitudes of the individual components at all temperatures for each sample to values obtained from simultaneous global fits over a range of temperatures. Typical fits are shown in the insets of Fig. 4 (a) and (b) for the polycrystal and single crystal samples respectively.

$$A(t) = \sum_{i=1}^n A_i e^{-\sigma_i^2 t^2} \cos(\omega_i t + \varphi) \quad (1)$$

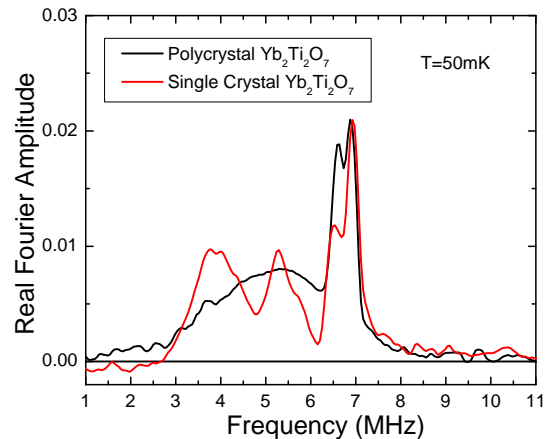


FIG. 3. Fourier Transform of μSR asymmetry spectra in a transverse field of 50 mT at $T=50$ mK. The single crystal $\text{Yb}_2\text{Ti}_2\text{O}_7$ shows 4 resolvable frequencies (red) and the polycrystalline $\text{Yb}_2\text{Ti}_2\text{O}_7$ shows three (black). This motivates $n=4$ for the single crystal and $n=3$ in the polycrystalline $\text{Yb}_2\text{Ti}_2\text{O}_7$ for Eq. (1). The sharp signal at approximately 7 MHz for both samples reflects the precession of the muons in the Ag cryostat tails.

We show the results of this analysis for the frequencies of each component in Fig. 4. The highest frequency component (labeled in grey) for each sample exhibits no temperature dependence. We ascribe this signal to muons landing in the silver sample holder which provides a useful reference signal for determining the muon Knight shift. The frequencies originating in the samples all show a strong temperature dependence as shown in Fig. 4. We parametrized the Knight shifts of these signals referenced to the silver signal by fitting them to a Curie-Weiss temperature dependence in the temperature range $400 \text{ mK} < T < 3.5 \text{ K}$. We used a common “Curie-Weiss temperature” (T_{CW}^μ) for each signal which was allowed to vary between samples. The resulting frequencies obtained from these fits of the Knight shifts are indicated by the black solid lines in Fig. 4; for both samples $T_{\text{CW}}^\mu = -1.3 \pm 0.5 \text{ K}$, which is considerably below the value ($\Theta_{\text{CW}}=+0.4 \text{ K}$) we obtain at higher temperatures (above 2 K) in dc-magnetization. For both samples we see a strong deviation from this parametrized Curie-Weiss behavior below the temperature corresponding to the onset of the specific heat phase transition, indicated by arrows in Fig. 4. This deviation indicates that there is a marked change in the muon Knight shift (which reflects the local spin susceptibility

and Yb^{3+} -muon hyperfine coupling) onseting at about the thermodynamic phase transition and that this occurs in both samples.

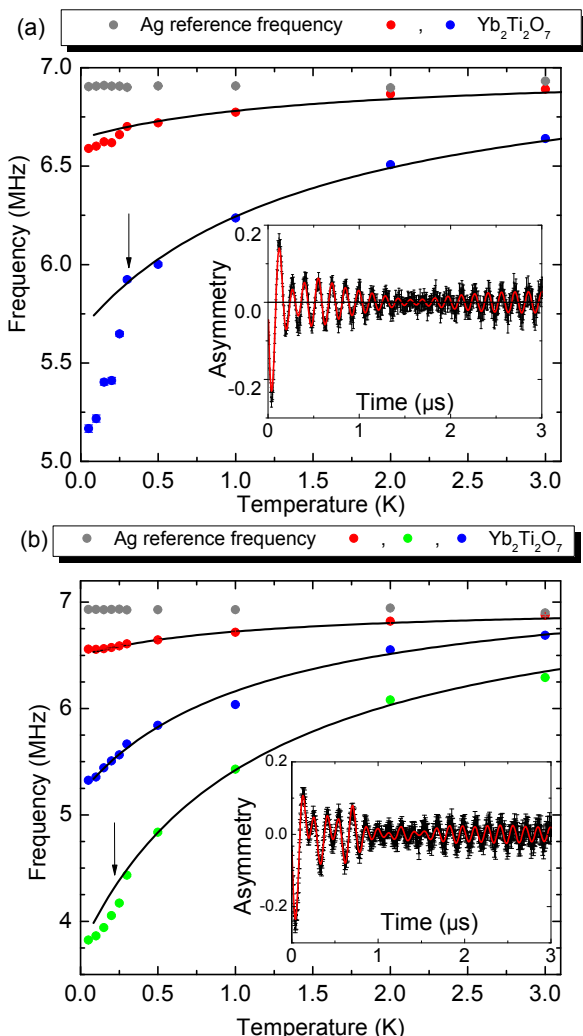


FIG. 4. The Yb^{3+} spin susceptibility characterized by $\text{TF}=50$ mT μSR measurements of (a) polycrystalline and (b) single crystal $\text{Yb}_2\text{Ti}_2\text{O}_7$. For the single crystal $\text{Yb}_2\text{Ti}_2\text{O}_7$ the initial muon polarization points perpendicular to the TF field which was applied parallel to [111]. There are two distinct muon signals from the polycrystalline sample, and three from the single crystal sample. The arrows show the approximate temperature of the onset of the transition observed in the specific heat. The solid black lines represent Curie–Weiss fits, as described in the text. The insets show asymmetry spectra (black) and fit to Eq.1 (red).

The similarities of our data between the polycrystalline and single crystal samples is surprising considering their very different specific heat signatures indicating a wide range of stuffing [15]. It is also surprising that we see no evidence for the dramatic first-order-like change in the spin fluctuation rate that was previously reported [6]. This difference is apparent in the raw data and is evi-

dence of a sample dependence between those studied by Hodges *et al.* and this work which must go beyond the differences in stuffing between our polycrystal and single crystal samples. Our results suggest that from a local microscopic point of view, the magnetic ground state is to a large extent insensitive to some aspects of sample variation, and that a sharp specific heat transition does not signify magnetic order.

Our weak LF measurements, shown in Fig. 2 exhibit a weakly temperature dependent spin fluctuation rate to the lowest temperatures studied. Many frustrated pyrochlore systems exhibit a substantial, largely temperature independent LF/ZF relaxation [20, 22, 23] which although often seen in frustrated or low-dimensional magnetic systems have not yet been explained [20]. A recent proposed explanation for these apparent persistent spin dynamics in terms of quantum diffusion of muons suggested for $\text{Dy}_2\text{Ti}_2\text{O}_7$ [24] is untenable here (and likely in that case as well as we would expect similar muon diffusion behaviour in the two systems). If muons were mobile in $\text{Yb}_2\text{Ti}_2\text{O}_7$, then they would move between different possible magnetically inequivalent sites which would broaden all of the individual TF lines in Fig. 3 into one, which clearly does not occur. Furthermore, we can exclude a “muon impurity” effect in which the presence of the muon would locally destroy the magnetic behaviour, since our TF- μSR measurements are clearly sensitive to the transition which strongly affects the muon Knight shift.

$\text{Yb}_2\text{Ti}_2\text{O}_7$ exhibits a clear phase transition evidenced by specific heat measurements, however the ground state is not magnetically ordered. This leaves the nature of the low temperature state unresolved, although we do know that it involves a change of the local spin susceptibility and/or hyperfine coupling. This behavior recalls that of the moderate heavy fermion system URu_2Si_2 which has thermodynamic phase transition at 17.5 K to a so-called “hidden-order” state [25] without magnetic order, whose order parameter remained unknown for more than 20 years of detailed study. In the case of URu_2Si_2 , recent studies [26–28] indicate the phase transition originates from a change in the hybridization between the localized electronic states associated with the uranium atoms and the conduction band, as it enters the heavy fermion state. While such a mechanism could not occur in insulating $\text{Yb}_2\text{Ti}_2\text{O}_7$, we are still left with a thermodynamic phase transition with an unidentified order parameter. Numerous exotic ground states have been proposed [29] for spin-1/2 pyrochlore systems including quantum spin liquid (QSL) and Coulomb ferromagnet in addition to antiferromagnetic and ferromagnetic order. Another possibility which could be considered is a valence bond solid (VBS). Of these states, the QSL and VBS would have no static magnetic moments consistent with our results. However, it is unclear whether or how the known Hamiltonian for $\text{Yb}_2\text{Ti}_2\text{O}_7$ could give rise to

either of these states. Which of these phases or perhaps other more exotic states is realized in $\text{Yb}_2\text{Ti}_2\text{O}_7$ remains to be seen.

Research at McMaster University and University of Waterloo is supported by NSERC while research at Columbia is supported by the US NSF PIRE (OISE-0968226) and DMR-1105961 projects. We appreciate the technical support of Dr. B. Hitti and Dr. A. Dabkowski and the TRIUMF Centre for Molecular and Materials Science. This work is supported in part by the Canada Research Chair program (M.J.P.G., Tier 1) and by the Perimeter Institute for Theoretical Physics through Industry Canada and by the Province of Ontario through the Ministry of Economic Development & Innovation.

* dortenrm@mcmaster.ca

- [1] J.S. Gardner, M.J.P. Gingras and J.E. Greedan. *Rev. Mod. Phys.* **82**, 53107 (2010).
- [2] C. Castelnovo, R. Moessner and S.L. Sondhi. *Nat. Lett.* **451**, 4245 (2008).
- [3] R. Applegate, N. R. Hayre, R. R. P. Singh, T. Lin, A. G. R. Day and M. J. P. Gingras, *Phys. Rev. Lett.* **109**, 097205 (2012).
- [4] L.-J. Chang, S. Onoda, Y. Su, Y.-J. Kao, K.-D. Tsuei, Y. Yasui, K. Kakurai, and M.R. Lees. *Nat. Comm.* **3**, 992 (2012).
- [5] Y. Yasui, M. Soda, S. Iikubo, M. Ito, M. Sato, N. Hamaguchi, T. Matsushita, N. Wada, T. Takeuchi, N. Aso and K. Kakurai. *J. Phys. Soc. Japan.* **72**, 11 (2003).
- [6] J.A. Hodges, P. Bonville, A. Forget, A. Yaouanc, P. Dalmas de Réotier, G. André, M. Rams, K. Królas, C. Ritter, P.C.M. Grubbens, C.T. Kaiser, P.J.C. King and C. Baines. *Phys. Rev. Lett.* **88**, 077204 (2008).
- [7] K.A. Ross, L.R. Yaraskavitch, M. Laver, J.S. Gardner, J.A. Quilliam, S. Meng, J.B. Kycia, D.K. Singh, Th. Proffen, H.A. Dabkowska and B.D. Gaulin. *Phys. Rev. B* **84**, 174442 (2011).
- [8] J.S. Gardner, G. Ehlers, N. Rosov, R.W. Erwin and C. Petrovic. *Phys. Rev. B* **70**, 180404 (2004).
- [9] K.A. Ross, J.P.C. Ruff, C.P. Adams, J.S. Gardner, H.A. Dabkowska, Y. Qiu, J.R.D. Copley and B.D. Gaulin. *Phys. Rev. Lett.* **103**, 227202 (2009).
- [10] K.A. Ross, L. Savary, B.D. Gaulin and L. Balents. *Phys. Rev. X* **1**, 021002 (2011).
- [11] N. R. Hayre, K. A. Ross, R. Applegate, T. Lin, R. R. P. Singh, B. D. Gaulin and M. J. P. Gingras, arXiv:1211.5934, (2012).
- [12] P. Bonville, J.A. Hodges, E. Bertin, J.Ph. Bouchaud, P. Dalmas de Réotier, L.-P. Regnault, H.M. Ronnow, J.-P. Sanchez, S. Sosin and A. Yaouanc. *Hyper. Inter.* **156/157**, 103–111 (2004).
- [13] P. Dalmas de Réotier, V. Glazkov, C. Martin, A. Yaouanc, P.C.M. Gubbens, S. Sakarya, P. Bonville, A. Amato, C. Baines and P.J.C. King. *Physica B.* **374375**, 145-147 (2006).
- [14] H. Takatsu, H. Kadowaki, T.J. Sato, J.W. Lynn, Y. Tabata, T. Yamazaki, and K. Matsuhira, *Journal of Physics: Condensed Matter* **24**, 052201 (2012).
- [15] K.A. Ross, Th. Proffen, H.A. Dabkowska, J.A. Quilliam, L.R. Yaraskavitch, J.B. Kycia and B.D. Gaulin. *Phys. Rev. B.* **86** 174424 (2012).
- [16] A. Yaouanc, P. Dalmas de Réotier, C. Martin and V. Glazkov. *Phys. Rev. B.* **84**, 172408 (2011).
- [17] *Springer Handbook of Crystal Growth*, Chap. 12. H. Dabkowska, A. Dabkowski (Springer, Verlag Berlin Heidelberg) (2010).
- [18] S.T. Bramwell, M.N. Field, M.J. Harris and I.P. Parkin. *J. Phys. Condens. Matter* **12** 483 (2000).
- [19] J.A. Hodges, P. Bonville, A. Forget, M. Rams, K. Królas and G. Dhalenne. *J. Phys. Condens. Matter* **13** 9301 (2001).
- [20] S.R. Dunsiger, A.A. Aczel, C. Arguello, H. Dabkowska, M.-H. Du, T. Goko, B. Javanparast, T. Lin, F.L. Ning, H.M.L. Noad, D.J. Singh, T.J. Williams, Y.J. Uemura, M.J.P. Gingras and G.M. Luke. *Phys. Rev. Lett.* **107**, 207207 (2011).
- [21] P. Dalmas de Réotier, A. Yaouanc, L. Keller, A. Cervellino, B. Roessli, C. Baines, A. Forget, C. Vaju, P.C.M. Grubbens, A. Amato and P.J.C. King. *Phys. Rev. Lett.* **96**, 127202 (2006).
- [22] Y.J. Uemura A. Keren, K. Kojima, L.P. Le, G.M. Luke, W.D. Wu, Y. Ajiro, T. Asano, Y. Kuriyama, M. Mekata, H. Kikuchi and K. Kakurai. *Phys. Rev. Lett.* **73**, 3306 (1994).
- [23] P.A. McClarty, J.N. Cosman, A.G. Del Maestro and M.J.P. Gingras. *J. Phys. Condens. Matter.* **23**, 164216 (2011).
- [24] P. Quemerais, P. McClarty and R. Moessner. *Phys. Rev. Lett.* **109**, 127601 (2012).
- [25] J.A. Mydosh, P.M. Oppeneer. *Mod. Phys. Rev.* **83**, (2011).
- [26] C. R. Wiebe, J. A. Janik, G. J. MacDougall, G. M. Luke, J. D. Garrett, H. D. Zhou, Y.-J. Jo, L. Balicas, Y. Qiu, J. R. D. Copley, Z. Yamani, and W. J. L. Buyers, *Nature Physics* **3**, 91–95 (2007).
- [27] U. Nagel, T. Room, T. Uleksin, R. P. S. M. Lobo, P. Lejay, C. C. Homes, J. Hall, A. W. Kinross, S. Purdy, T. J. Williams, G. M. Luke and T. Timusk, *Proc. Nat. Acad. Sci.* **109**, 19161 (2012).
- [28] A. R. Schmidt, M. H. Hamidian, P. Wahl, F. Meier, A. V. Balatsky, T. J. Williams, G. M. Luke and J. C. Davis, *Nature* **465**, 570 (2010).
- [29] L. Savary and L. Balents, *Phys. Rev. Lett.* **108**, 037202 (2012).

